


<b>Title</b>	Fabrication of sub-10 nm lamellar structures by solvent vapour annealing of block copolymers
<b>Author(s)</b>	Chaudhari, Atul
<b>Publication date</b>	2015
<b>Original citation</b>	Chaudhari, A. 2015. Fabrication of sub-10 nm lamellar structures by solvent vapour annealing of block copolymers. PhD Thesis, University College Cork.
<b>Type of publication</b>	Doctoral thesis
<b>Rights</b>	© 2015, Atul Chaudhari. <a href="http://creativecommons.org/licenses/by-nc-nd/3.0/">http://creativecommons.org/licenses/by-nc-nd/3.0/</a> 
<b>Embargo information</b>	No embargo required
<b>Item downloaded from</b>	<a href="http://hdl.handle.net/10468/2488">http://hdl.handle.net/10468/2488</a>

Downloaded on 2017-02-12T06:41:26Z



**UCC**

University College Cork, Ireland  
Coláiste na hOllscoile Corcaigh

# **Fabrication of sub-10 nm lamellar structures by Solvent Vapour Annealing of Block Copolymers**

**Atul Chaudhari**

Department of Chemistry,

University College Cork,

Ireland.



# UCC

Coláiste na hOllscoile Corcaigh, Éire  
University College Cork, Ireland

This thesis is presented to the National University of Ireland for the  
degree of

***Doctor of Philosophy***

October 2015

Supervisor: Prof. Michael A Morris

Head of Department: Prof. Martyn Pemble

## **Declaration**

I Atul Chaudhari verify that this Thesis is my own work and I have not acquired a degree in this university or elsewhere on the foundation of this Ph.D thesis.

-----

Atul Chaudhari

Date:

# Acknowledgements

---

This dissertation is the result of almost four years of research at University College Cork, Cork, Ireland. I would like to express my sincere gratitude to many people whose continual support, both professionally and personally, have made this dissertation possible. The work in this dissertation is a direct result of the combined efforts and discussion of the block copolymer team.

First and foremost, I would like to thank my PhD supervisor, Prof. Michael A. Morris for his mentoring and continuous support throughout these years. It is my honour to have been able to work with Mick for the past four years. His commitment towards science and innovative ideas has been a source of inspiration. He consistently led our research team, and required our best efforts. He motivated me to work hard and follow ethical practices towards research. I regard his influence as the single biggest factor contributing to my growth from a student to a researcher. I will definitely miss the environment of his laboratory, which was great fun-filled experience.

I am equally thankful to my co-supervisor Prof. Justin D. Holmes for his insightful comments during the course of my research. I would also like to thank Matthew T. Shaw for his close supervision especially on the Intel project. He always provided me a comfort zone by providing a great encouragement and discussions with him were always fruitful and satisfactory. I am extremely lucky to have had worked with him, and I appreciate the unique input from him. I would also like to thank our collaborators at Intel for helpful discussion and financial support for this project.

No graduate experience can be successful without the support and assistance of colleagues and fellow students. This includes Dr. Dipu Borah, Dr. Parvaneh Mokarian, Dr. Sibin C. Padmanabhan, Dr. Atul Thorat, Dr. Ramsankar Senthamarai Kannan, Dr. Cian Cummins, who provided both expertise and camaraderie within the lab. Dr. Tandra Ghoshal, I would like to thank you for both help and friendship during my time in Cork. You were the biggest strength during my PhD research and cannot thank you enough for the energy, knowledge and

motivation you gave. I cannot sufficiently thank all the past and current members in the Mick's group for research discussion and friendship: Dr. Sozaraj Rasappa, Timothy Collins, Elsa Giraud, David Sullivan. I wish to extend my sincere gratitude to all the members of Lab 343 and 115 from Department of Chemistry in UCC. My sincere thanks to the administrative and technical staff of Chemistry department in UCC.

My colleagues and friends were my surrogate family away from home. Their love and care never let homesickness dampen my spirits. Thanks to the "*Marathi-mandal*" in Cork, for their love and friendship that I will cherish all my life. Indians in Cork, mini-India, were always there to entertain with loads of Indian festival celebrations and for making life in Cork very easy. Thanks Anushka for a wonderful friendship and for all the support. I will miss a big laugh-riot. AFM and SEM sessions were never stressful when you were around. More than a colleague and friend, we are family. I will miss you!!

I would like to share this great moment of my life with my family. I find myself at a loss of words while expressing my appreciation for my mother for her unconditional love, support and prayers. Her persistent confidence in me has always been my greatest strength. I cannot thank her enough for allowing me to pursue my interests. Special thanks to my siblings, Prashant and Vaishali. My sincere thanks to my Uncle Mr. Narendra Nerkar and brother-in-law, Mr. Rajendra Chaudhari for their support. Special thanks to dear Mr. and Mrs. Shirsath for their love and taking care of my mom during my stay abroad. Sincere gratitude to my grandparents, most loved and dearest, are the strongest pillars of my family. Love from kids back in India always made me smile and cannot thank enough to Megha, Tejas, Dipesh, Kunal, Yash, Mansi, Ashish and Mihir for giving me happiness. During my PhD, I got married to a beautiful girl, Shital. I thank you for all your support and love you bestowed upon me. I am deeply indebted to you for your continual smiling face, kindness, patience, and wisdom led my way through the last stage of my PhD. Thanks to my in-laws Mr. and Mrs. Baviskar for the support.

Finally, I thank my Dad who is not with us but watching us from the heaven. Will always miss you and love you until we meet again Dad. Thank you!!!

*To Aai*

# Abstract

---

Fabrication of nanoscale patterns through the bottom-up approach of self-assembly of phase-separated block copolymers (BCP) holds promise for nanoelectronics applications. For lithographic applications, it is useful to vary the morphology of BCPs by monitoring various parameters to make “from lab to fab” a reality. Here I report on the solvent annealing studies of lamellae forming polystyrene-*block*-poly(4-vinylpyridine) (PS-*b*-P4VP). The high Flory-Huggins parameter ( $\chi = 0.34$ ) of PS-*b*-P4VP makes it an ideal BCP system for self-assembly and template fabrication in comparison to other BCPs. Different molecular weights of symmetric PS-*b*-P4VP BCPs forming lamellae patterns were used to produce nanostructured thin films by spin-coating from mixture of toluene and tetrahydrofuran(THF). In particular, the morphology change from micellar structures to well-defined microphase separated arrangements is observed. Solvent annealing provides a better alternative to thermal treatment which often requires long annealing periods. The choice of solvent (single and dual solvent exposure) and the solvent annealing conditions have significant effects on the morphology of films and it was found that a block neutral solvent was required to realize vertically aligned PS and P4VP lamellae. Here, we have followed the formation of microdomain structures with time development at different temperatures by atomic force microscopy (AFM). The highly mobilized chains phase separate quickly due to high Flory-Huggins ( $\chi$ ) parameter. Ultra-small feature size (~10 nm pitch size) nanopatterns were fabricated by using low molecular weight PS-*b*-P4VP (PS and P4VP blocks of 3.3 and 3.1 kg mol<sup>-1</sup> respectively). However, due to the low etch contrast between the blocks, pattern transfer of the BCP mask is very challenging. To overcome the etch contrast problem, a novel and simple *in-situ* hard

mask technology is used to fabricate the high aspect ratio silicon nanowires. The lamellar structures formed after self-assembly of phase separated PS-*b*-P4VP BCPs were used to fabricate iron oxide nanowires which acted as hard mask material to facilitate the pattern transfer into silicon and forming silicon nanostructures.

The semiconductor and optical industries have shown significant interest in two dimensional (2D) molybdenum disulphide (MoS<sub>2</sub>) as a potential device material due to its low band gap and high mobility. However, current methods for its synthesis are not 'fab' friendly and require harsh environments and processes. Here, I also report a novel method to prepare MoS<sub>2</sub> layered structures via self-assembly of a PS-*b*-P4VP block copolymer system. The formation of the layered MoS<sub>2</sub> was confirmed by XPS, Raman spectroscopy and high resolution transmission electron microscopy.



# Table of Contents

---

Acknowledgements	II
Abstract	V
Table of Contents	VII
List of Figures	XI
List of Tables	XVI
List of Schemes	XVII
List of Publications	XVIII

## CHAPTER 1. *Introduction*

---

1.1	Motivation and Outline of Thesis	1
1.2	Conventional Lithographic Techniques	3
1.3	Block Copolymer Lithography	9
1.3.1	Introduction	9
1.3.2	Self-assembly of Block Copolymers	11
1.3.3	Block Copolymer thin films	15
1.3.4	Solvent Vapour Annealing	16
1.4	Self-assembly of PS- <i>b</i> -P4VP Block Copolymers	21
1.5	References	30

## CHAPTER 2. *The Effect of Solvent Vapour Annealing Conditions on the Thin Film Morphologies of Lamellar Forming Polystyrene-*b*-poly (4-vinylpyridine) Block Copolymers*

---

<b>2.1</b>	<b>Abstract</b>	<b>47</b>
<b>2.2</b>	<b>Introduction</b>	<b>47</b>
<b>2.3</b>	<b>Experimental</b>	<b>50</b>
2.3.1	Materials	50
2.3.2	Thin film preparation, solvent annealing and characterization	50
<b>2.4</b>	<b>Results and Discussion</b>	<b>51</b>
2.4.1	Micellization of PS- <i>b</i> -P4VP	51
2.4.2	Microphase separation by solvent selective annealing	53
2.4.3	Solvent vapour annealing with time	58
2.4.4	BCP reconstruction with ethanol	60
<b>2.5</b>	<b>Conclusions</b>	<b>61</b>
<b>2.6</b>	<b>References</b>	<b>63</b>

**CHAPTER 3. *The Effect of Solvent Vapour Annealing Conditions on the Thin Film Morphologies of Lamellar Forming Polystyrene-*b*-poly (4-vinylpyridine) Block Copolymers***

---

<b>3.1</b>	<b>Abstract</b>	<b>71</b>
<b>3.2</b>	<b>Introduction</b>	<b>71</b>
<b>3.3</b>	<b>Experimental</b>	<b>74</b>
3.3.1	Materials and methods	74
3.3.2	Thin film preparation, solvent annealing and characterization	75
<b>3.4</b>	<b>Results and Discussion</b>	<b>76</b>
3.4.1	Self-assembly of PS- <i>b</i> -P4VP by annealing in THF environment	78
3.4.2	Self-assembly of PS- <i>b</i> -P4VP by annealing in mixed solvent	84

	environment	
3.4.3	Fabrication of sub-7 nm features by solvent annealing	87
3.4.4	Effect of film thickness on the morphology of BCP thin films	91
3.4.5	Graphoepitaxy	93
<b>3.5</b>	<b>Conclusions</b>	<b>94</b>
<b>3.6</b>	<b>References</b>	<b>96</b>

## **CHAPTER 4. *Fabrication of Inorganic Nanostructured Etch Mask by Self-Assembly of Polystyrene-*b*-poly (4-vinylpyridine)***

---

<b>4.1</b>	<b>Abstract</b>	<b>104</b>
<b>4.2</b>	<b>Introduction</b>	<b>104</b>
<b>4.3</b>	<b>Experimental</b>	<b>107</b>
4.3.1	Materials and methods	107
4.3.2	Iron oxide nanowire patter fabrication	108
4.3.3	Characterization	108
<b>4.4</b>	<b>Results and Discussion</b>	<b>109</b>
4.4.1	Self-assembly of BCP by solvent annealing	109
4.4.2	BCP imaging by Helium Ion Microscopy	111
4.4.3	Etching of PS- <i>b</i> -P4VP	112
4.4.4	Iron oxide nanowires fabrication by inclusion technique	113
4.4.5	Pattern transfer of iron oxide nanowires into Si-substrate	116
<b>4.5</b>	<b>Conclusions</b>	<b>119</b>
<b>4.6</b>	<b>References</b>	<b>121</b>

## **CHAPTER 5. *Fabrication of a Layered MoS<sub>2</sub> Structure via the Self-Assembly of Block Copolymers***

---

<b>5.1</b>	<b>Abstract</b>	<b>128</b>
<b>5.2</b>	<b>Introduction</b>	<b>128</b>
<b>5.3</b>	<b>Experimental</b>	<b>130</b>
5.3.1	Materials	130
5.3.2	MoS <sub>2</sub> nanowire formation	131
5.3.3	Characterization	132
<b>5.4</b>	<b>Results and Discussion</b>	<b>133</b>
5.4.1	Self-assembly of BCP by solvent annealing	133
5.4.2	Molybdenum oxide nanowires fabrication by inclusion technique	134
5.4.3	Determination of the MoO <sub>x</sub> stoichiometry by XPS	135
5.4.4	Sulfurization of MoO <sub>3</sub> nanowires	136
<b>5.5</b>	<b>Conclusions</b>	<b>143</b>
<b>5.6</b>	<b>References</b>	<b>145</b>

## **CHAPTER 6. *Conclusions and Future work***

---

<b>6.1</b>	<b>Motivation and Outline of Thesis</b>	<b>155</b>
<b>6.2</b>	<b>Conventional Lithographic Techniques</b>	<b>159</b>

# List of Figures

---

**Figure 1.1.** Basic schematic illustration of 'pitch' and 'half-pitch'

**Figure 1.2.** Portrait of Aloys Senefelder by Lorenz Quaglio

**Figure 1.3.** Schematic illustration of photolithography process. Patterns are created on a substrate by using a UV light source to expose photoresist-coated surfaces through an optical mask.

**Figure 1.4.** Schematic representation of Electron Beam Lithography (EBL) to write either positive or negative patterns in the resist.

**Figure 1.5.** Schematic illustration of Hot-NIL and UV-NIL.

**Figure 1.6.** Block copolymer architectures

**Figure 1.7.** Typical phase diagram of a diblock copolymer, calculated using self-consistent mean field theory. The different phases are: L: Lamellar, C: hexagonally packed cylinders, S: Spheres packed in a bcc lattice, G: gyroid, S: closed packed spheres

**Figure 1.8.** Possible configurations of lamellae forming diblock copolymer: parallel lamellae with (a) symmetric wetting, (b) asymmetric wetting and (c) perpendicular lamellae at neutral surface. 'n' is integer (n=1, 2, 3...)

**Figure 1.9.** Solvent vapour annealing (SVA) in closed jar containing thin BCP film and vial of annealing solvent

**Figure 1.10.** (A) H-bonded supramolecule obtained by intermolecular H-bonding between pentadecylphenol and PS-*b*-P4VP block copolymer. (B) Schematic representation of nanostructure material obtained. (C) Lamellar-within-cylindrical structure before PDP removal. (D) After PDP removal, the cylindrical structure is obtained under mild conditions.

**Figure 1.11.** Schematic representation of the fabrication of oxide nanodots from (A) highly ordered self-assembled PS-*b*-PEO by solvent annealing method. (B) After activation of PEO cylinders. (C) Metal oxide precursor on top of the activated film by spin coating. (D) Oxide dots after UV/Ozone treatment.

**Figure 1.12.** Schematic illustration of the fabrication of Si nanowires. (A) Spin coated PS-*b*-PEO BCP (B) Solvent annealed phase separated PEO cylinders parallel to the substrate in the PS matrix (C) Activation of PEO cylinders (D) Metal precursor solution spin coated on the activated film (E) After UV/Ozone treatment (F) Si nanowires fabrication by silica and silicon ICP etch process.

**Figure 2.1.** AFM images of a PS<sub>20k</sub>-*b*-P4VP<sub>17k</sub> thin films, 0.5 wt% casting solution (A). (B) and (C) are SEM images of similar films formed at 0.3 wt%. The micelle nature of the film can be very clearly seen in (C).

**Figure 2.2.** Topographic AFM images (1x1 $\mu$ m) of PS<sub>9k</sub>-*b*-P4VP<sub>9.2k</sub> cast from toluene/THF (80/20) and solvent annealed at 50 °C for 4h in different saturated solvent vapour environments of: (A) pure toluene, (B) toluene/THF = 90/10, (C) toluene/THF = 80/20, (D) toluene/THF = 70/30, (E) toluene/THF = 60/40, (F) toluene/THF = 50/50, (G) toluene/THF = 40/60, (H) toluene/THF = 30/70, (I) toluene/THF = 20/80, (J) toluene/THF = 10/90 and (K) pure THF. All solvent compositions are given as (v/v). FFT patterns inset show the difference in the degree of order.

**Figure 2.3.** (A) The vapour pressures of a solution of the two liquids, toluene and THF at 50 °C, is the sum of the two individual vapour pressures, calculated by Raoult's law. (B) Vapour-Liquid equilibrium diagram of toluene and THF mixture.

**Figure 2.4.** AFM images of as-spun (A) PS<sub>20k</sub>-P4VP<sub>17k</sub> thin film casted from toluene/THF (80/20) and solvent annealed (B-F) PS<sub>20k</sub>-P4VP<sub>17k</sub> films at 50 °C for different time in THF vapour: (B)30 min, (C) 1h, (D) 2h, (E) 3h and (F) 6h. The lamellar domain structures are perpendicular to a substrate. FFT patterns inset show the difference in the degree of order.

**Figure 2.5.** Topographic AFM images (1  $\mu$ m x 1  $\mu$ m) of reconstructed PS<sub>9k</sub>-P4VP<sub>9.2k</sub> thin films for different time (A) 2min, (B) 5min, (C) 7min, (D) 10min and (E) 20min respectively. FFT patterns (inset) show the difference in the degree of order.

**Figure 3.1.** AFM topographic images of solvent annealed PS<sub>21k</sub>-*b*-P4VP<sub>21k</sub> thin films exhibiting lamellar structures after annealing at 40 °C (A-2 to A-9), 50 °C (B-2 to B-9) and 60 °C (C-2 to C-9) for 30 min to 7 h under THF atmosphere, respectively. The thickness of as-cast and solvent annealed film has a thickness of 33 nm and 35 nm  $\pm$  2 nm, respectively.

**Figure 3.2.** AFM topographic images of solvent annealed PS<sub>9k</sub>-*b*-P4VP<sub>9.2k</sub> thin films exhibiting lamellar structures after annealing at 40 °C (A-2 to A-9), 50 °C (B-2 to B-9) and 60 °C (C-2 to C-9) for 30 min to 7 h under THF atmosphere, respectively. The thickness of as-cast and solvent annealed film has a thickness of 28 nm and 29 nm  $\pm$  2 nm, respectively.

**Figure 3.3.** AFM topographic images of solvent annealed PS<sub>7.4k</sub>-*b*-P4VP<sub>7.7k</sub> thin films after annealing at 50 °C for 30 min to 6 h under THF (A-2 to A-4), toluene (B-2 to B-4) and a mixture of toluene/THF (50/50, v:v) (C-2 to C-8) atmosphere, respectively.

**Figure 3.4.** AFM topographic images of solvent annealed PS<sub>5k</sub>-*b*-P4VP<sub>5k</sub> thin films exhibiting lamellar structures after annealing at 40 °C (A-1 to A-6), 50 °C (B-1 to B-6) and 60 °C (C-1 to C-6) for 1 h to 6 h under a toluene atmosphere, respectively.

**Figure 3.5.** AFM topographic images of solvent annealed PS<sub>3.3k</sub>-*b*-P4VP<sub>3.1k</sub> thin films exhibiting lamellar structures after annealing at 40 °C (A-1 to A-7), 50 °C (B-1 to B-7) for 1 h to 6 h and 60 °C (C-1 to C-4) for 1 h to 4 h under toluene atmosphere, respectively.

**Figure 3.6.** AFM topographic images of solvent annealed PS<sub>7.4k</sub>-*b*-P4VP<sub>7.7k</sub> thin films after annealing at 50 °C for 6 h under toluene/THF (50/50, v:v), spin coated at: (A-1) 1000 rpm, (A-2) 1500 rpm, (A-3) 1800 rpm, (A-4) 2400 rpm, (A-5) 3000 rpm, (A-6) 4000 rpm and (A-7) 5000 rpm.

**Figure 3.7.** AFM topographic images of PS<sub>3.3k</sub>-*b*-P4VP<sub>3.1k</sub> thin films formed on patterned Si<sub>3</sub>N<sub>4</sub> substrates. Data shown are with Si<sub>3</sub>N<sub>4</sub> mesa and channel widths of (A) 30 nm and 50 nm, (B) 150 nm and 240 nm.

**Figure 3.8.** Pitch size versus the  $\chi N$  values of all PS-*b*-P4VP used in this study. 7.6 nm is an estimated value calculated by drawing an arbitrary line.

**Figure 4.1.** AFM topographic images of different molecular weight PS-*b*-P4VP BCPs after solvent annealing. The lamellae perpendicular to the substrates were observed in all the BCP systems: (A) PS<sub>20k</sub>-*b*-P4VP<sub>17k</sub>, (B) PS<sub>9k</sub>-*b*-P4VP<sub>9.2k</sub>, (C) PS<sub>7.4k</sub>-*b*-P4VP<sub>7.7k</sub>, (D) PS<sub>5k</sub>-*b*-P4VP<sub>5k</sub>, and (E) PS<sub>3.3k</sub>-*b*-P4VP<sub>3.1k</sub>.

**Figure 4.2.** (A) Chemical structure of PS-*b*-P4VP. (B) and (C) are HIM images of unetched PS<sub>9k</sub>-*b*-P4VP<sub>9.2k</sub> and PS<sub>5k</sub>-*b*-P4VP<sub>5k</sub>.

**Figure 4.3.** SEM image of PS<sub>9k</sub>-*b*-P4VP<sub>9.2k</sub> film post 30 s RIE with flow rate of 30 sccm CF<sub>4</sub> / 5 sccm O<sub>2</sub> at 15 mTorr.

**Figure 4.4.** Top-down SEM images of iron oxide nanowires formed by using (A) PS<sub>20k</sub>-*b*-P4VP<sub>17k</sub>, (B) PS<sub>9k</sub>-*b*-P4VP<sub>9.2k</sub>, (C) PS<sub>7.4k</sub>-*b*-P4VP<sub>7.7k</sub>, (D) PS<sub>5k</sub>-*b*-P4VP<sub>5k</sub> and (E) PS<sub>3.3k</sub>-*b*-P4VP<sub>3.1k</sub>. All scale bars represent 200 nm.

**Figure 4.5.** (A) XPS survey spectra recorded from the iron oxide nanowires on Si substrate after UV/Ozone treatment. (B) and (C) are the high resolution Fe2p and C1s spectra of iron oxide nanowires on the Si substrate.

**Figure 4.6.** (A) SEM image of iron oxide nanowires formed using PS<sub>20k</sub>-*b*-P4VP<sub>17k</sub> and (B) is SEM image of pattern transferred Si nanostructures, inset shows cross sectional SEM image.

**Figure 4.7.** Progressive Si etch after various etch periods (conditions C<sub>4</sub>F<sub>8</sub> and SF<sub>6</sub> at the flow rate of 90 sccm and 30 sccm, respectively at 10 Torr and 100°C). (A-1 to A-

5) are Si nanowires fabricated by using PS<sub>20k</sub>-*b*-P4VP<sub>17k</sub> at different etching times 10 s (A-1), 40 s (A-2), 90 s (A-3), 120 s (A-4) and 150 s (A-5). (B-1 to B-6) are Si nanowires fabricated by using PS<sub>9k</sub>-*b*-P4VP<sub>9.2k</sub> at different etching times 5 s (B-1), 10 s (B-2), 15 s (B-3), 20 s (B-4), 30 s (B-5) and 60 s (B-6).

**Figure 5.1.** Experimental setup of the quartz tube in the centre of the furnace containing sulphur flowers and MoO<sub>3</sub> samples (see text for details).

**Figure 5.2.** AFM topographic images of (A) as-cast and (B) phase separated PS-*b*-P4VP thin films after solvent annealing in THF for 6 h at 50 °C

**Figure 5.3.** AFM topography image (A), top-down SEM image (B) and (C) is SEM image of same sample at higher magnification of molybdenum oxide nanowires obtained after UV/Ozone treatment of self-assembled PS<sub>20k</sub>-*b*-P4VP<sub>17k</sub> for 3 h.

**Figure 5.4.** XPS spectra of (A) wide scan spectra (survey), (B) Mo 3*d*, (C) Mo 3*p* and (D) O 1*s* core level spectra of molybdenum oxide nanowires after UV/Ozone treatment.

**Figure 5.5.** Scanning electron micrographs of MoS<sub>2</sub> nanowires formed after sulfurization of MoO<sub>3</sub> nanowires by thermal evaporation of sulphur powders at: (A-B) 300 °C for 30 min, (C) 400 °C for 20 min and (D) 700 °C for 15 min.

**Figure 5.6.** MoS<sub>2</sub> nanopatterns analyzed by XPS and Raman spectroscopy. (A) XPS survey spectrum of the MoS<sub>2</sub> prepared at 300 °C. High resolution XPS spectra of (B) Mo 3*d* and S 2*s*; and (C) S 2*p*. (D) Raman spectrum of MoS<sub>2</sub> nanowires formed after sulfurization at 300 °C, 400 °C and 700 °C showing the E<sub>12g</sub> and A<sub>1g</sub> vibrational modes

**Figure 5.7.** (A) and (B) are the topographic AFM images of MoO<sub>3</sub> and MoS<sub>2</sub> nanowires, (C) and (D) are the height profiles of (A) and (B) respectively.

**Figure 5.8.** (A) TEM images of MoS<sub>2</sub> nanowires. (B) Enlarged HR-TEM image of the marked area in (A). (C) EDX mapping of MoS<sub>2</sub> nanowire revealing presence of S and Mo.

**Figure 5.9.** (A) is the AFM topography images of PS<sub>9k</sub>-*b*-P4VP<sub>9.2k</sub> after solvent annealing in THF for 6 h at 50 °C, (B) is the topographic AFM image of the MoO<sub>3</sub> nanowires obtained after UV/Ozone treatment of sample shown in (A), and (C) is SEM image of the MoS<sub>2</sub> nanowires obtained after sulfurization at 300 °C.

**Figure 6.1.** Topographic AFM images (1x1µm) of PS<sub>9k</sub>-*b*-P4VP<sub>9.2k</sub> cast from toluene/THF (80/20) and solvent annealed at 50 °C for 4h in different saturated solvent vapour environments of: (A) pure toluene, (B) toluene/THF =90/10, (C) toluene/THF =80/20, (D) toluene/THF =70/30, (E) toluene/THF =60/40, (F) toluene/THF =50/50, (G) toluene/THF =40/60, (H) toluene/THF =30/70, (I)



toluene/THF =20/80, (J) toluene/THF =10/90 and (K) pure THF. All solvent compositions are given as (v/v). FFT patterns inset show the difference in the degree of order.

**Figure 6.2.** AFM topographic images of different molecular weight PS-*b*-P4VP BCPs after solvent annealing. The lamellae perpendicular to the substrates were observed in all the BCP system: (A) PS<sub>20k</sub>-*b*-P4VP<sub>17k</sub>, (B) PS<sub>9k</sub>-*b*-P4VP<sub>9.2k</sub>, (C) PS<sub>7.4k</sub>-*b*-P4VP<sub>7.7k</sub>, (D) PS<sub>5k</sub>-*b*-P4VP<sub>5k</sub>, and (E) PS<sub>3.3k</sub>-*b*-P4VP<sub>3.1k</sub>. (F) Pitch size versus the  $\chi N$  values of all PS-*b*-P4VP used in this study. 7.6 nm is an estimated value calculated by drawing an arbitrary line.

**Figure 6.3.** Top-down SEM images of iron oxide nanowires formed by using (A) PS<sub>20k</sub>-*b*-P4VP<sub>17k</sub>, (B) PS<sub>9k</sub>-*b*-P4VP<sub>9.2k</sub>, (C) PS<sub>7.4k</sub>-*b*-P4VP<sub>7.7k</sub>, (D) PS<sub>5k</sub>-*b*-P4VP<sub>5k</sub> and (E) PS<sub>3.3k</sub>-*b*-P4VP<sub>3.1k</sub>. All scale bars represent 200 nm.

**Figure 6.4.** (A) TEM images of MoS<sub>2</sub> nanowires. (B) Enlarged HR-TEM image of the marked area in (A).

## List of Tables

---

**Table 2.1.** Molecular characteristics of the PS-*b*-P4VP Diblock Copolymer

**Table 2.2.** Hansen Solubility Parameters (MPa<sup>1/2</sup> for Relevant Materials)

**Table 3.1.** List of PS-*b*-P4VP BCPs used

**Table 3.2.** The Selectivity of the solvents and interaction parameter ( $\chi$ )

**Table 3.3.** Vapour Pressures of the Annealing Solvents at Different Temperatures

**Table 4.1** Molecular characteristics of block copolymers used

## List of Schemes

---

**Scheme 3.1.** Schematic of time development of the microdomain formation on thin symmetric PS-*b*-P4VP film. The gray and blue region represents PS and P4VP blocks. (A) is as-cast thin film, (B) is thin film after exposed to solvent vapours, (C-E) plausible microstructures after solvent annealing.

**Scheme 5.1.** Schematic of the formation of the MoO<sub>x</sub> nanowires. (A) PS-*b*-P4VP BCP spin coated on silicon wafer, (B) phase separated BCP thin film after solvent annealing, (C) loading of molybdenum precursor on/in the P4VP domains by spin coating and (D) fabrication of MoO<sub>x</sub> nanowires by UV/Ozone treatment.

## List of Publications

---

[1] Cummins, C.; Borah, D.; Rasappa, S.; Chaudhari, A.; Ghoshal, T.; O'Driscoll, B. M. D.; Carolan, P.; Petkov, N.; Holmes, J. D.; Morris, M. A.. *Journal of Materials Chemistry C* **2013**, *1* (47), 7941-7951.

[2] Borah, D.; Ghoshal, T.; Shaw, M. T.; Chaudhari, A.; Petkov, N.; Bell, A. P.; Holmes, J. D.; Morris, M. A. *Nanomater Nanotechnol* **2014**, *4* (25).

[3] Bell, A. P.; Senthamaraiannan, R.; Ghoshal, T.; Chaudhari, A.; Shaw, M. T.; Lesson, M.; Morris, M. A. *Proc. SPIE 9424, Metrology, Inspection, and Process Control for Microlithography XXIX* **2015**, 13

[4] Chaudhari, A.; Ghoshal, T.; Shaw, M. T.; Cummins, C.; Borah, D.; Holmes, J. D.; Morris, M. A., *Proc. SPIE 9051, Advances in Patterning Materials and Processes XXXI*, **2014**; pp 905110-905110-10.

[5] Chaudhari, A.; Ghoshal, T.; Shaw, M.T.; Cummins, C; Borah, D; Holmes, J.D.; Morris, M.A., The effect of solvent annealing conditions on the film morphologies of lamellar forming polystyrene-b-poly(4-vinylpyridine) *Applied Materials & Interfaces* **2015**. *Under revision*

[6] Atul Chaudhari, Tandra Ghoshal, Matthew T. Shaw, John O'Connell, Roisin A. Kelly, Colm Glynn, Colm O'Dwyer, Justin D. Holmes, Michael A. Morris, Fabrication of a Layered MoS<sub>2</sub> Structure via the Self-Assembly of Block Copolymers. *Advanced Materials Interfaces* **2015**. *Accepted*

# 1

## Introduction

---

### 1.1. Motivation and Outline of Thesis

Nanostructured materials have at least one dimension in the range from 1 to 100 nm. Nanomaterials can have advanced properties over macroscopic systems due to their nanoscale dimensions and have applications as electronic, biomedical, and optical materials.<sup>1-7</sup> One-dimensional (1D) nanostructures (e.g. rods, tubes, wires) are expected to play an important role as both interconnects and functional units in fabricating electronic, optoelectronic, electromechanical and electrochemical nanodevices.<sup>8,9</sup>

In 1965, co-founder of Intel, Gordon Moore, predicted that the number of transistors incorporated in a chip will approximately double every 24 months for about the same cost. This statement has held true to this day and is known as Moore's law.<sup>10</sup> In 1971, the Intel 4004 CPU had 2300 transistors on it. As of 2015, the highest transistor count in a commercial available CPU (in one chip) is over 4.3 billion transistors, in Intel's i5-core Xeon Ivy Bridge-Ex. If transistors were people, Intel's chip has almost the same number of transistors as the population of Asia at approximately 4.4 billion people. Because the chip size is constant, the scale of each transistor gets smaller, the density higher and transistor count increases at a regular pace to provide improvements in integrated circuit functionality and performance while decreasing costs per device. The semiconductor industry is driving to maintain the rapid speed of shrinking increased as the half-pitch, which is half the distance between identical features in an array (Fig. 1-1).

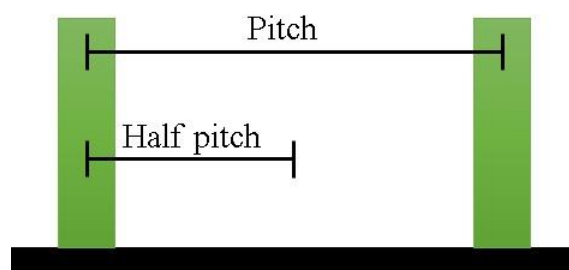


**Figure 1.1.** Basic schematic illustration of 'pitch' and 'half-pitch'

Top-down lithography has traditionally been the main technique for patterning structures that are used in high technological devices in industries. Currently, ultraviolet photolithography is able to bring the feature sizes down towards tens of nanometers but in coming years, photolithography may become less cost effective than alternative methods. According to the International Technology Roadmap for Semiconductor (ITRS-2013),<sup>11</sup> lithographic methods are becoming very expensive and technically highly challenging. Extreme-UV lithography (EUVL) remains the leading candidate for the 22 nm and 16 nm half-pitches, extending it to higher resolutions becomes a significant long-term challenge. EUVL with wavelength at 13.5 nm is recognized as the main hope of the industry to advance Moore's Law.<sup>12</sup> EUVL must overcome challenges such as delays in the production of high-power sources, needs for fast resists, defect-free and high-flatness masks to be cost-competitive at 10 nm or beyond. Lithography is the most expensive cost factor in integrated chip manufacturing and there are continued pressures.<sup>13</sup> E.g. in 1981, a 5 MB hard drive cost about \$3500 or \$700/MB. Today, in 2015, terabyte hard drives sell for about \$100 or \$0.0001/MB. The ITRS-2013 has also noted that Directed Self-Assembly (DSA) has shown significant progress but defectivity and positional accuracy are the biggest concerns which must see rapid improvement.<sup>12</sup>

## 1.2. Conventional Lithographic Techniques

### History

Printmaking methods for text were developed in China and date back to 220 AD.<sup>14</sup> The plate for an entire page would be made from a block of wood by pressing a hand-lettered page to its surface to leave character marks in ink and then carving out the surface around the characters. This type of printing is called as xylography. The disadvantage of this wood-block printing is that it took a long time to fabricate and has size limitations.

In 1040, moveable type printing was created by another Chinese worker named Bi Sheng who made individual characters out of clay and glued them together to form the printing plate.<sup>15</sup> This fabrication technique though saved time but it was not useful due to Chinese culture and language which has thousands of characters. In 1452, Johannes Gutenberg from Germany, invented the moveable press and he is best known for printing the first commercial Bible.<sup>16</sup> During the 18<sup>th</sup> century, publications were illustrated, usually with copper plate etchings and engraving. In the 19<sup>th</sup> century, in the wake of the Industrial Revolution, a broad array of new techniques were introduced that included wood engraving and notably lithography etc.<sup>17</sup>

Lithography (from Greek, *lithos*, meaning stone and *graphein*, meaning to write), was invented in 1796 by a Bavarian author Aloys Senefelder.<sup>18, 19</sup> Using this method, it was possible to produce a large number of prints from a single drawing executed on a block of limestone. Lithography uses a very simple chemical process to create an image. The principle of lithography, relying upon simple chemical principles-the mutual repulsion of oil and water and the mutual attraction of salt and water. The image is drawn on the surface of the print plate with a fat or oil-based medium (hydrophobic) e.g. something like a wax crayon. Then a mixture of nitric acid and gum Arabic is spread over the stone. This solution was used to create a hydrophilic layer of calcium nitrate salt and gum Arabic on all the non-written surface. Then

the stone was moistened with water, which attracted to the layer of gum and salt created by the acid wash. Then the printing ink was rolled over the image. A sheet of paper then placed over the surface to transfer the inked image onto the paper. The name lithography became universal due to the inscription on Lorenz Quaglio's famous 1818 portrait of Senefelder, as shown in Fig. 1.2, that reads: "*Aloys Senefelder: Erfinder der Lithographie and der Chemischen Druckerey*", which means Aloys Senefelder: Inventor of Lithography and Chemical Printing.

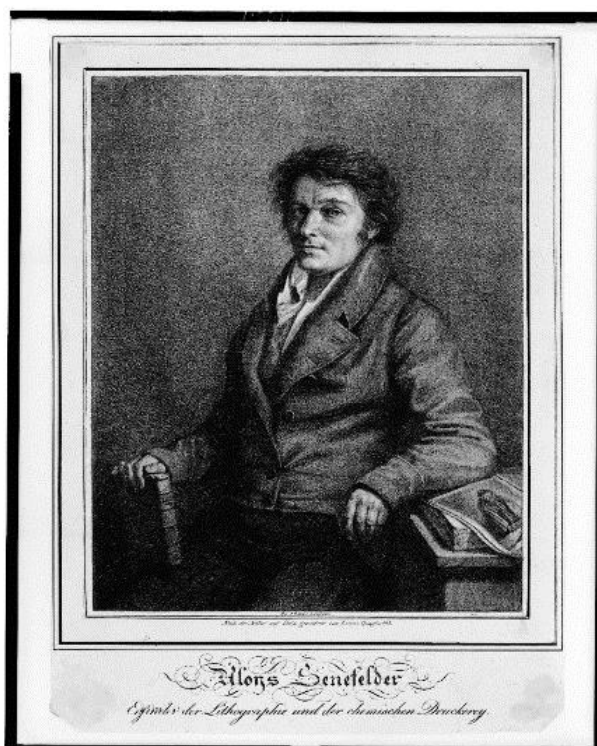


**Figure 1.2.** Portrait of Aloys Senefelder by Lorenz Quaglio

Until the 20th century, nearly all printing techniques were developed and optimized for the storage of records meant to be accessed by the human eye; therefore, resolution beyond what the naked eye could observe ( $\sim 50 \mu\text{m}$ ) was not a strong driving force.<sup>20</sup> Microlithography and nanolithography methods of pattern formation on lithographic principle are capable of structuring material on a fine scale. In next part of the introduction, various modern lithographic techniques are discussed. Their relationship to the work of Senefelder is obvious.



## Photolithography

Photolithography is a three-step process of deposition, exposure and development to pattern a layer of photosensitive polymer (photoresist). Photolithography which is also known as optical lithography is widely used in the semiconductor industry to produce micron-sized features where a selective part of a thin film can be controllably etched.<sup>21-23</sup>

In photolithography, the photoresist is spin coated on the substrate which is then exposed in a photolithography tool under UV light source using an optical mask as shown in Fig. 1.3. The photomask is created by a photographic process and developed onto a substrate. The cheapest masks use ordinary photographic emulsion on soda lime glass, while Chrome-on-Quartz glass is used for the high-resolution deep UV lithography. In the last step, an alkaline solution is used for the development process for few minutes which dissolves the exposed photoresist, leaving behind the unexposed resist.

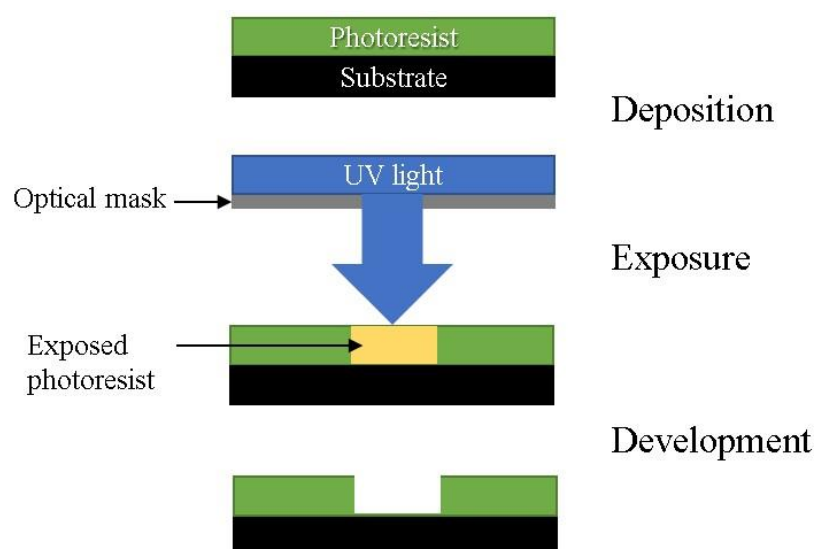


**Figure 1.3.** Schematic illustration of photolithography process. Patterns are created on a substrate by using a UV light source to expose photoresist-coated surfaces through an optical mask.

Photolithography is an advantageous lithographic process because of its capability to achieve high throughput at low cost, and which has the capability of simultaneous fabrication on large

areas to form many features. However, the major limitation is the light source resolution and which is determined by the Rayleigh equation, where the resolution is proportional to the exposure wavelength and inversely proportional to the numerical aperture of the optical system. Because of this the resolution in photolithography can be improved by reducing the wavelength of the light source but secondary factors such as the photoresist materials, photomask and the processing equipment can all have an effect on the practical resolution achievable.<sup>10</sup>

### **Electron Beam Lithography**

Electron-beam lithography (EBL) is a technique used for the fabrication of micro- and nanostructures, based on the chemical modification of polymer resist films caused by electron irradiation.<sup>24, 25</sup> In EBL, the resist is exposed by a focused beam of electrons consistently moving in the plane of the pattern. As shown in Fig. 1.4, the concept of EBL is similar to photolithography or any other lithographies. The substrate is coated with a resist coating. After exposure to the electron beam, the patterns can be written on the substrates. The exposed areas can be dissolved in a specific solvent to get positive patterns in the resists. As an alternative the e-beam can be used to cross-link the resist to form a solvent resistant area. The unexposed areas can then be dissolved to give negative patterns as shown in Fig. 1.4. In simple words, positive resists leave positive patterns while negative patterns are formed due to negative resists.

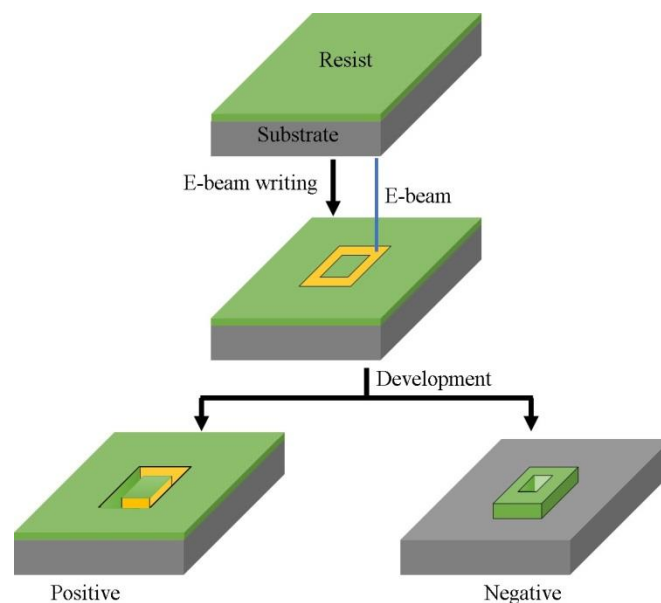


**Figure 1.4.** Schematic representation of Electron Beam Lithography (EBL) to write either positive or negative patterns in the resist.

Unlike photolithography, EBL is a mask-free direct writing system. The electron beam is controlled by a computer and, therefore, there is no need of masks or templates. Due to the sequential scanning of the image, EBL is time consuming process because of the increase in exposure time. EBL has a resolution down to a few nanometers with a large depth of focus. But due to high cost and very low throughput, EBL has limitations in mass-production industries. For example, to expose an area of  $1 \text{ cm}^2$  would require approximately 10 days, whereas to write on  $700 \text{ cm}^2$  surface area of a 300 mm silicon wafer, the time required will be about 20 years. However, multi-beam e-beam systems may improve the practicality of the methodology.<sup>26</sup>

A single-step approach to form patterned polymer brushes on oxide surfaces by EBL has been reported by Rastogi et.al.<sup>27</sup> The polymer brushes consisting of an e-beam sensitive compound, like poly(methyl methacrylate) (PMMA), were first grown on blanket substrates by surface-initiated atom-transfer radical polymerization (ATRP), and then exposed to an electron beam

to carry out chain scission and thus achieve direct nanoscale patterns. Self-assembled monolayers (SAM) of different polymers were patterned on silicon substrates with a resolution down to 50 nm using direct e-beam patterning.

### Nanoimprint Lithography

Regarded as one of the most non-conventional lithographic methods, nanoimprint lithography (NIL) is considered as a possible alternative to photolithography due to its low cost, high throughput and high resolution. Since the invention of NIL by Stephen Chou et al.<sup>28-32</sup> to date, techniques such as thermal embossing<sup>33</sup> and UV nanoimprint lithography (UV-NIL)<sup>33</sup> have been incorporated into the field of NIL as shown in Fig. 1.5.

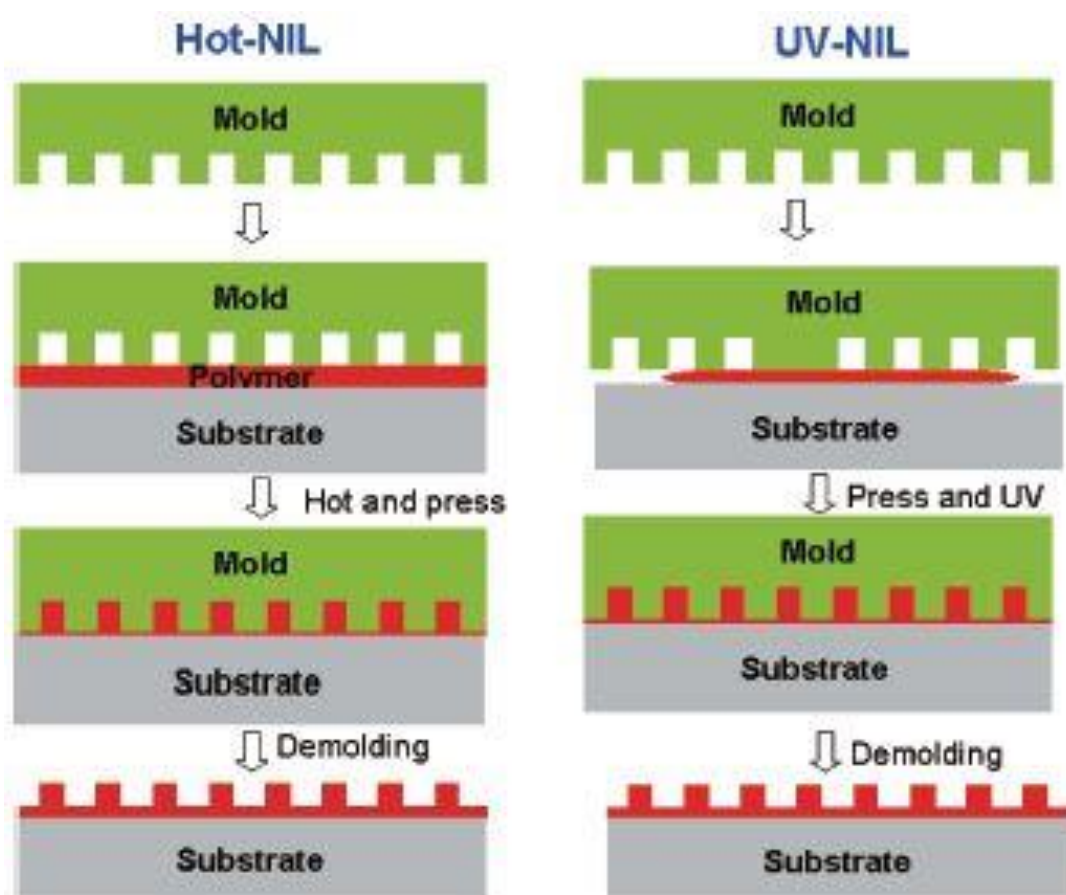


**Figure 1.5.** Schematic illustration of Hot-NIL and UV-NIL. (Adapted from Ref. 34)

The substrate is first spin coated with polymer resists and then the mold is pressed on the substrate. The mold is removed to have imprinted patterns on the substrate from the mold

template. To avoid air-bubble while pressing the mold, the imprinting should be done in vacuum. In UV-NIL, instead of using a polymer on the substrate, photo-curable resist is used. A transparent mold is pressed and UV exposure is used to cure the solution.

### **1.3. Block copolymer Lithography**

#### **1.3.1. Introduction**

Current optical photolithography technology approaches the limits for achievable feature size and, hence, novel methods of fabrication on the sub-20 nm scale are thought to be of great importance. As mentioned earlier, electron beam lithography (EBL), photolithography and nanoimprint lithography (NIL) are all “top-down” processes which may be able to fabricate future sub 14 nm-node wafer technology. Top-down processes are time consuming, expensive and has a resolution limit which further rely on pattern transfer through masks. As an alternative, bottom-up processes are emerging as viable alternatives for the fabrication of nanoscale features.

A polymer is composed of a repeating molecular unit, called *mer*. Copolymers are formed by arranging two distinct monomers to form random, alternating, or block patterns. These polymers have special geometrical arrangements depends on polymerization techniques to form star, comb, brush, ladder, or dendritic architectures. Here, the focus will be on a special type of copolymer, block copolymers (BCPs). For industrial applications, block copolymers have been used as solubilizers, oil additives, compatibilizers, foams, and as thermoplastic elastomers.<sup>35</sup> BCPs are a unique class of soft-materials with the ability to self-assemble into well-ordered microdomains on the nanometer scale.<sup>36, 37</sup> BCPs can be defined as a class of polymers formed by covalently connecting two or more different monomers, which are often immiscible.<sup>38</sup> Due to the structural diversity within block copolymers, diblock, triblock or multiblock copolymers can be formed by incorporating two, three or multiple blocks,

respectively. Also, various architectures can be formed during synthesis such as linear, branched, miktoarm block copolymers, as shown in Fig. 1.6.

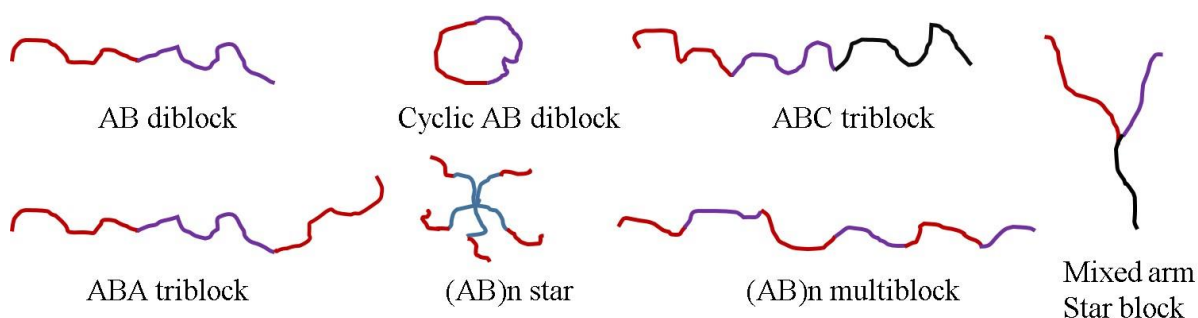


**Figure 1.6.** Block copolymer architectures

Linear block copolymers generally comprise two or more polymer chains in sequence. Linear BCPs are typically synthesized by living anionic polymerization, conducted as early as 1956.<sup>39</sup> During polymerization, an alkali or alkaline earth metal act as a catalyst which is reacted with the first monomer and creates a reactive carbanionic site that initiate chain propagation. In this manner the first monomer is polymerized and after its complete consumption, the second monomer is added, which again is polymerized to completion. After polymerization, the reaction is terminated by adding a terminating agent. The synthesized diblock copolymer then can be isolated by precipitating in a nonsolvent. It must be noted that the carbanion formed by the first monomer must be able to initiate the polymerization of the second monomer (more nucleophilic). Under careful control of the polymerization reaction, polymers with close to ideal polydispersity can be synthesized. This is indicated by the polydispersity index (PDI) which is the measure of the overall distribution of molecular weights of the synthesized polymer chains, given by,

$$\text{PDI} = \frac{M_w}{M_n}$$

where,  $M_w$  is the weight-average molar mass and  $M_n$  is the number-average molar mass. The larger the polydispersity index, the broader the molecular weight distribution. Generally, a monodisperse polymer where all the chain lengths are equal (e.g. proteins) has an  $M_w/M_n=1$ . The best controlled synthetic polymers available have  $M_w/M_n$  of 1.02 to 1.10.

In this thesis, we have studied in detailed the self-assembly of diblock block copolymer polystyrene-*block*-poly (4-vinylpyridine) (PS-*b*-P4VP), and its self-assembly by solvent annealing techniques. PS-*b*-P4VP was first synthesized by anionic polymerization as reported by Grosius et.al.<sup>40</sup>

### 1.3.2. Self-assembly of Block Copolymers

As stated above, BCPs consist of chemically distinct polymer chains covalently bonded to form a single polymer chain molecule. Self-assembly of BCPs is an equilibrium process representing a balance between repulsive and attractive forces between the two different blocks. Due to their mutual repulsion, dissimilar blocks lead to segregate into different domains whilst similar blocks aggregate. Self-assembly is a temperature dependent process. At lower temperature, enthalpic forces of attractive and repulsion dominate the phase separation, while at higher temperature; entropy dominates, driving the polymers towards a homogeneous mixing of blocks. It must be noted that, phase separation will only occur when the Gibbs free energy of mixing is greater than zero. Flory-Huggins theory,<sup>41</sup> is the classical theory for calculating the free energy of mixing. The Gibbs free energy of mixing for two homopolymers is given by the Flory-Huggins equation:

$$\frac{\Delta G_{\text{mix}}}{RT} = \left[ \frac{\phi_A}{N_A} \right] \ln \phi_A + \left[ \frac{\phi_B}{N_B} \right] \ln \phi_B + \chi_{FH} \phi_A \phi_B$$

Where  $\phi$ ,  $N$ , and  $\chi$  are the volume fraction, degree of polymerization (the total number of repeating units) and the Flory-Huggins segmental interaction parameters respectively. Most of the understanding of microphase separation of BCPs is centred on the Flory-Huggins interaction parameter, which is related to the enthalpic change due to the incompatibility of the two different blocks. The phase behaviour of BCPs is strongly affected by the temperature.<sup>42</sup>  $\chi$  is inversely proportional to temperature and is given by a relationship of the general term:

$$\chi = a + \frac{b}{T}$$

where, 'a' and 'b' are both constants (determined experimentally). Usually 'b' has positive values. Another parameter that strongly influences the BCPs behaviour is the total degree of polymerization  $N$ . Since  $\chi$  is a measure of dissimilarity between the blocks,  $\chi N$  represents the total dissimilarity over the whole BCP system. As the temperature increases,  $\chi$  decreases and if the  $\chi N$  value is sufficiently low, the BCP will not phase separate and undergoes an order-disorder transition (ODT). The extent of segregation of BCPs depend on the  $\chi N$  value. BCPs phase behaviour can be divided in three regimes according to the value of  $\chi N$ ; strong segregation limit (SSL,  $\chi N > 100$ ), weak segregation limit (WSL,  $\chi N \sim 10$ ) and intermediate segregation limit ( $10 < \chi N < 100$ ). A simple phase diagram is shown in Fig. 1.7. The focus of this thesis will be on diblock copolymer forming lamellar morphologies ( $f \sim 0.5$ ) in the strong and intermediate segregation limit.

Helfand and coworkers developed the self-consistent field (SCF) theory, for the strong segregation limit (SSL), to calculate the free energies, chain conformation and composition profiles of BCPs.<sup>43-45</sup> The weak-segregation limit used the Landau-Ginzburg approach to analyse the free energy was described by Leibler.<sup>46</sup> Another method was developed by Matsen and coworkers to analyse the ordering of BCPs in bulk and in thin films using mean field theory (MFT).<sup>47-50</sup> This implementation of SCF theory predicts the phase diagrams and represents



state-of-the-art for modelling the ordering of soft materials. A phase diagram derived using self-consistent mean field theory to predict the morphologies for a particular phase fraction is shown in Fig. 1.7. Different morphologies from the self-assembly of BCPs can be obtained by varying the relative volume fraction of blocks,  $f$ . Asymmetric diblock copolymers form spherical and cylindrical microdomains with increase in volume fraction of the minor block. The lamellar morphology can be seen when both the blocks have same volume fraction (symmetric diblock copolymer). The morphologies shown in Fig. 1.7 are determined for bulk materials. Whereas, for lithographic applications, thin films are desired.

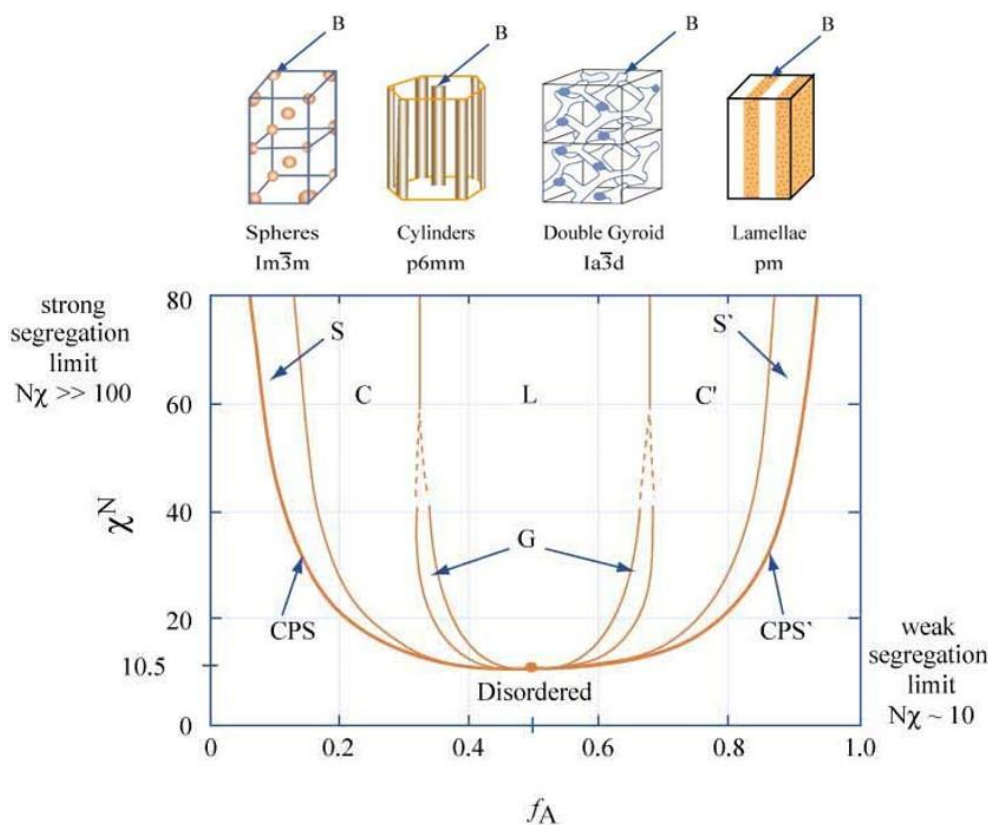


**Figure 1.7.** Typical phase diagram of a diblock copolymer, calculated using self-consistent mean field theory. The different phases are: L: Lamellar, C: hexagonally packed cylinders, S: Spheres packed in a bcc lattice, G: gyroid, S: closed packed spheres

As can be seen from Fig. 1.7, phase boundaries are vertical in the SSL, but become curved with lowering  $\chi N$ . BCPs with volume fractions near the phase boundary between two morphologies

can allow thermally induced order-to-order transition (OOT), since  $\chi$  varies according to the change in temperature. In the case of lamellar morphology ( $f = 0.5$ ), the stretching energies of the blocks are balanced and the molecules pack into flat interfaces. Whereas, the asymmetric blocks favours curvature of the interface toward the minority domain which stretch but this stretching is compensated by relaxation of the larger block matrix. The lamellar phase remains stable to  $f = 0.375$ , because no other structure offers a small enough interfacial curvature.<sup>51</sup> There is a lower limit of  $\chi N = 10.5$ , below which phase separation cannot usually be achieved.

BCP thin films can be formed by different techniques like dip-coating, flow-coating, and spin-coating.<sup>52-54</sup> During these techniques, the solvent may be evaporated slowly to achieve the thermodynamic equilibrium, although this is usually not seen in spin coating where solvent evaporation is very rapid. The casting of BCPs is usually performed by two primary methods mainly, spin coating and flow coating. In spin coating, the BCP solution is prepared in a volatile solvent and is deposited on a substrate undergoing rapid rotation. During rotation, the solution flows off to form a uniform thin film. After spin coating, the solvent trapped inside the BCP thin film is subject to solvent evaporation which leaves a film with low surface roughness. The final film thickness depends on the nature of the polymer solution (surface tension, drying rate and concentration). Zhang et al,<sup>55</sup> have reported that the surface morphology of BCPs can be altered by flow-coating. Flow-coating of BCP films creates higher residual stress by stretching the polymer chains into non-equilibrium conformations. After spin coating, the residual film thickness largely depends on the spinning speed and the concentration of the BCP solution. The film thickness is also found to be dependent on the molecular weight and the molecular weight distribution (PDI) of the BCPs.<sup>56</sup> In this thesis, we have only used the spin-coating method to prepare the thin films of block copolymers. Silicon wafers were used for spin-coating due to the flat surface and industrial importance. The surface energy difference between substrate and BCPs should be minimal to avoid dewetting. The substrate can be modified by

surface treatment or other substrates can be used to better match the surface energy of the deposited BCP to avoid dewetting.<sup>57-59</sup>

### 1.3.3. Block copolymer thin films

Thin films of BCPs can be used as templates or etch masks in lithography. The thickness of thin polymer film can be controlled by the concentration of the polymer solution and the spin speed to coat the polymer solution on a substrate. However, the phase behaviour of BCP thin films are more complicated compared to BCP bulk due to the interfacial energies as well as the commensurability between the film thickness ( $t$ ), the microdomain spacing ( $L_0$ ) and confinement effects imposed at both polymer-substrate and polymer-air interfaces. For a lamellae-forming BCP thin film three possible configuration are as shown in Fig. 1.8.

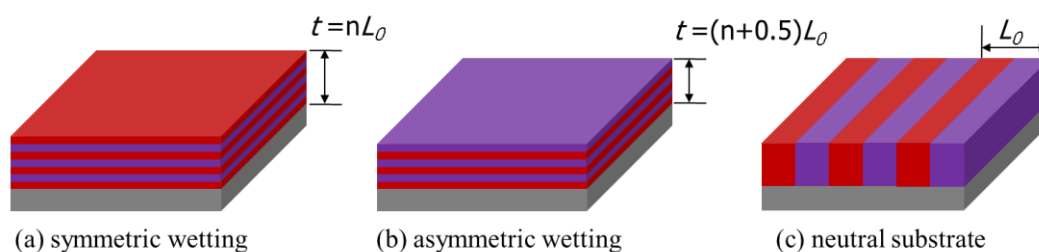


**Figure 1.8.** Possible configurations of lamellae forming diblock copolymer: parallel lamellae with (a) symmetric wetting, (b) asymmetric wetting and (c) perpendicular lamellae at neutral surface. ‘ $n$ ’ is integer ( $n=1, 2, 3\dots$ )

In BCP thin films, the orientation of the BCP microdomains is critical for BCP lithographic applications. Due to the high aspect ratio, perpendicular orientation of either cylinder or lamellae microdomains are favoured. Different surface energies of both blocks hinder the perpendicular orientation since segregation of one block to the interface is favoured. The covalently bonded blocks prefer parallel orientation to the substrate due to the strong preferential interaction of one block to the surface of the film or the substrate interface. If the same block is found at substrate or at air interface, symmetric wetting is observed ( $t = nL_0$ ), as

shown in Fig. 1.8 (a). However, if one of the block preferentially wets the interface either with the substrate or air, an asymmetric wetting is formed ( $t = (n+0.5)/Lo$ ), as shown in Fig. 1.8 (b). Whereas, if the substrate surface becomes neutral, when there is no preference for blocks to wet the confining surfaces, to perpendicularly oriented lamellae with low free energy can be formed, as illustrated in Fig. 1.8 (c). When the substrate surface is neutral, i.e. the interfacial interactions of both blocks are equally favourable (or unfavourable), there is no preferential segregation of the components to the interfaces. When the thickness of the film is not commensurate to the equilibrium lamellar spacing, the orientation can change depend on the interfacial energy and either holes or island will form maintaining the parallel orientation to adjust the local film thickness.<sup>60</sup>

The surface selectivity can be minimized to obtain perpendicular orientations in thin films using various surface treatments. These include random copolymer brushes,<sup>61, 62</sup> crosslinked random copolymers,<sup>63</sup> functionalized random copolymers,<sup>64</sup> and self-assembled monolayers (SAM).<sup>64</sup>

#### **1.3.4. Solvent Vapour Annealing of Block copolymer thin films**

Due to the fast solvent evaporation, during spin coating, it is likely that the BCP chains get trapped into nonequilibrium state of ‘frozen’ state leaving the microdomains disorganized and in poorly ordered arrangements. It is difficult to obtain an ordered morphology of as-cast films, regardless of careful precautions taken during film preparation. To enhance the ordering of the BCP microdomains, either thermal annealing or solvent vapour annealing (SVA) are introduced to increase the mobility of the polymer chains to facilitate the microphase separation and annihilation of defects.

**Thermal annealing** is the simplest and was initially the most commonly used technique for aligning the BCP thin film morphologies. BCP thin films are generally placed in a heated

chamber above the glass transition temperature ( $T_g$ ) of both blocks and kept at elevated temperature for a certain time before cooling the thin films to room temperature. During heating, the polymer chains become mobile and rearrange via enthalpically driven thermodynamics and allow increases in ordering by minimizing the non-equilibrium effects at the surface due to casting and, thus, equilibrium morphology is approached.<sup>65, 66</sup> For example, the most commonly used BCP system, polystyrene-*block*-polymethylmethacrylate (PS-*b*-PMMA) usually undergoes thermal annealing at temperatures between 160 °C and 250 °C. Heating the BCP thin film above its  $T_g$  also removes any residual solvent in the film from coating. To avoid unwanted chemical contact or contamination, thermal annealing is carried out either in vacuum or under inert atmosphere for the required time.<sup>67</sup> Thermal annealing is found to be a molecular weight dependence method; for high molecular weight systems slow diffusion hinders the chain rearrangement and annealing for long periods (144 h) is not enough to obtain long range ordering.<sup>68, 69</sup> Due to the required temperature window, extensive annealing times, the kinetics of the order-disorder transition, thermal annealing may not be useful for all BCP systems. BCPs with high  $\chi N$ , are often difficult to process with thermal annealing due to the thermal degradation of BCP at high temperature since the temperature used is above ODT.

**Solvent vapour annealing (SVA)**,<sup>70</sup> is another effective annealing technique for fabrication of highly ordered vertically orientated lamellar and cylindrical microdomains in thin BCP films. In the SVA technique, the BCP films absorb solvent in the form of a vapour. To achieve long-range ordered morphologies without using elevated temperature, vapours of a “good” solvent are exposed to the thin films. A good solvent is one which facilitates solvent swelling. Despite a lack of complete understanding of mechanism of SVA, a few key points are summarized and discussed further below.

1. The solvent vapour acts as a plasticizer which imparts significant mobility to the BCP chains to reduce  $T_g$  of blocks below ambient temperature. This is an alternative to thermal annealing to achieve a higher chain mobility.<sup>71-74</sup>
2. Solvent trapped in thin films affects the interaction between blocks (i.e. separates chains) which leads to change in morphology by reducing the  $\chi_{\text{eff}}$ .
3. The presence of solvent vapour may establish an interface that is preferential to one block at the free surface and so may help to orientate the microdomains.

Libera and coworkers were one of the first groups to report that solvent evaporation could be used to increase the ordering and orientation of BCP microdomains.<sup>75, 76</sup> To control BCP morphology, various ratios of selective and partially selective solvents can be used.<sup>77, 78</sup> By increasing the vapour pressure of the solvent the degree of solvent vapour uptake in the film will be increased and so increase the chain mobility. The absorbed solvent will also successively decrease interfacial interactions between blocks. As reported by Lai et al.,<sup>79</sup> selective solvents can swell the domain spacing over the value for the bulk diblock copolymer. Niu et al. has shown that the residual solvent remaining in BCP films can also play a role in the ordered structure formation, which is not possible to observe by thermal annealing.<sup>80</sup> Due to swelling in thin film, the  $L_0$  of the film can be greater than the bulk  $L_0$ , affecting commensurability of the film.<sup>71, 81</sup>

Because of this complex array of solvent effects, it must be noted that during SVA, the order and orientation of the BCP thin films can respond to multiple processes and so depend upon a balance of the kinetics associated with each process. Thus, the morphology of the film by spin-coating or during SVA may be very different to that of the BCP in the bulk.

In the SVA technique, the introduction of the solvent vapour in the annealing chamber can be carried out in two different ways. In the first method, as shown in Fig. 1.9, the as-cast thin film

of BCP and the annealing solvent or mixture of solvents in glass vial is placed in an airtight chamber to process the solvent annealing. This is a ‘static’ technique. The chamber or reservoir can be replaced by an airtight glass bottle. The vapour pressure inside the chamber can be determined by the amount of solvent in the glass vial, the volume of chamber, the surface area of the solvent, humidity, temperature as well as the annealing time. This setup is not ideal as monitoring vapour pressure is not possible.

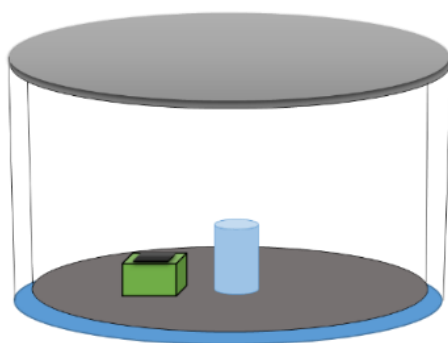


**Figure 1.9.** Solvent vapour annealing (SVA) in closed jar containing thin BCP film and vial of annealing solvent

In another approach, custom made annealing apparatus are used,<sup>82</sup> and the solvent vapours are carried by compressed inert gas bubbling into the annealing chamber rather than direct exposure as explained earlier. This is a more ‘dynamic’ methodology. The partial vapour pressure of solvent vapour can be controlled by changing the relative mixing ratio of solvent vapour in the inert gas flow with a pure inert gas flow. Due to the dilution of solvent vapour by inert gases, use of high vapour pressures is somewhat limited. Gotrik et al successfully used solvothermal annealing to align a polystyrene-*block*-polydimethylsiloxane (PS-*b*-PDMS) cylinder forming copolymer to generate arrays of hexagonally packed cylinders using a custom apparatus, which enables a solvent vapour annealing and a thermal quenching step to remove the solvent in the film.<sup>83</sup>

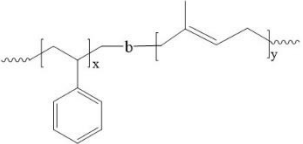
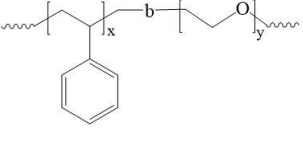
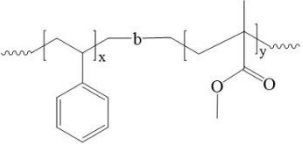
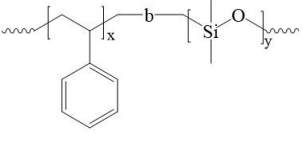
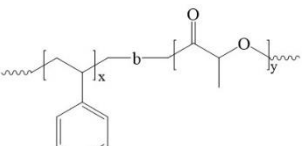
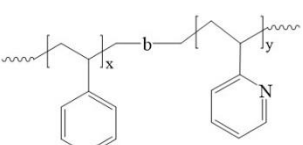
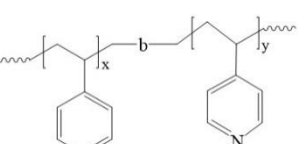
Solvent vapour annealing is more complex than thermal annealing, since choosing an ideal solvent is important. Hence, different morphologies in BCP films can be observed when annealed in different solvent vapours. Interaction between the blocks as well as their volume fractions can be changed while SVA, due to the differences in solubility of the block in a specific solvent, can lead to changes in morphology from that predicted by composition. The use of ideal non-selective organic solvents (i.e. without preferential adsorption on one of the blocks) is rare. If the solvent is highly selective to one block it leads to non-favourable interactions and can shift the morphology into non-equilibrium structures.<sup>77, 79, 81, 84, 85</sup> In the case of neutral solvent (both blocks are equally soluble in the solvent), a neutral surface to orient the microdomains perpendicular to the surface plane will be formed. If the equilibrium concentration of the solvent in the BCP is too high, it can lead to high chain mobility and minimization of the block-block interaction. This can drive the system into a disordered state although during solvent removal from the film the microdomains can self-assemble at the surface.<sup>74</sup> SVA provides a simple route to phase separate BCPs and allow self-assembly to generate different morphologies under different solvent vapours. An extensive review on the SVA in thin BCP films has been reported by Sinturel et al.<sup>70</sup> Different orientations of the cylindrical microdomains of polystyrene-*block*-polyethylene oxide (PS-*b*-PEO) thick films could be achieved by using different solvent evaporation rates.<sup>86</sup> SVA of high  $\chi$  block copolymers is of particular interest since in the last decade this have been used to generate smaller feature sizes. Thus, BCPs like PS-*b*-PDMS, PS-*b*-PEO, PS-*b*-P2VP, and PS-*b*-P4VP etc. are solvent vapour annealed under different environment to yield nanostructured microdomains.<sup>77, 81, 87-96</sup>



#### 1.4. Self-assembly of PS-*b*-P4VP Block Copolymers

There has been an increase in interest on study of BCPs with high Flory-Huggins interaction parameter,  $\chi$ . This allows microphase separation to be achieved for lower molecular weight BCPs and, so, smaller domain periodic structures can be formed. In particular, as shown in Table 1.1, PS-*b*-P4VP BCP has a larger  $\chi$  value than PS-*b*-PI, PS-*b*-PEO, PS-*b*-PMMA, PS-*b*-PDMS, PS-*b*-PLA and PS-*b*-P2VP BCPs, thus enabling microphase separation at very low molecular weight and the formation of highly ordered microdomains of features with sizes less than 10 nm is possible. It should also be noted that the interfacial energies of the different blocks can play an important role in controlling domain orientation in BCP thin films. In PS-*b*-P4VP, PS and P4VP have similar surface tensions of 41 nMm<sup>-1</sup> and 48 nMm<sup>-1</sup> respectively, at the air/polymer interfaces. Hence, there is little real preference for one block at the surface.

**Table 1.1. Structures and Flory- Huggins parameters for different block copolymers**

BCPs	Structure	Flory-Huggins parameter ( $\chi$ )	$\chi$ at 25°C	Reference
PS- <i>b</i> -PI		$33T^{-1} - 0.0228$	$\sim 0.09$	62
PS- <i>b</i> -PEO		$29.8T^{-1} - 0.023$	$\sim 0.08$	64
PS- <i>b</i> -PMMA		$4.46T^{-1} + 0.028$	$\sim 0.043$	63
PS- <i>b</i> -PDMS		$68T^{-1} + 0.037$	$\sim 0.265$	64
PS- <i>b</i> -PLA		$98.1T^{-1} - 0.112$	$\sim 0.22$	61
PS- <i>b</i> -P2VP		$63T^{-1} - 0.033$	$\sim 0.18$	65
PS- <i>b</i> -P4VP	 PS                  P4VP	NA	$\sim 0.34$	66

Another complexity possible in these systems is the ordering to form self-assembled structures in solution. The block copolymers can often be combinations of hydrophobic and hydrophilic moieties. Self-assembly of the BCP into micelles is possible and can lead to formation of well-defined arrangements of various sizes and shapes in dilute solution. Both, polar (water) and non-polar (toluene, chloroform) solvents can form micelles or inverse micelles. In the case of PS-*b*-P4VP, when dissolved in toluene, the formation of micellar structures is observed. Toluene is a selective solvent for PS while P4VP is insoluble in toluene. Upon dissolution at a low concentration solution (critical micelle concentration is 0.065 mg mL<sup>-1</sup>), PS-*b*-P4VP BCPs show strong spherical micellization. Because of the preferential interaction of toluene with the PS block the micelles have a PS corona and the P4VP block is in the core. When the casting solution is spin-coated on the substrate surface, these micelles can survive spin coating/solvent evaporation in the given conditions and form a monolayer or monolayers of densely packed, robust hemi-micelles on the substrate surface and form a disordered hexagonal arrangement. It must be noted that, the size of the micelle formed depends on the length of the polymer block (degree of polymerization). Micellar cores can be considered as nanoreactors in which inorganic precursors can be loaded to fabricate uniform nanoparticles.<sup>97</sup> Usually, the precursor is loaded into the micellar core simply by stirring the precursor metal salt in the micellar solution. With the strong interaction of the polymer with metal ions, metal ions are bound as polymeric ligands or as counterions. In PS-*b*-P4VP, P4VP is a strong metal-chelating agent and large number of different metal ions can be loaded into the P4VP core of the micelles.<sup>98-</sup><sup>100</sup> This type of chemistry will form an important part of this work as will be described.

The pyridine block present in PS-*b*-P4VP is the active functional component. Due to the presence of the heterocyclic nitrogen containing aromatic group (pyridine) it is hydrophilic in nature. The N-atom is in sp<sup>2</sup> hybridization state, the lone pair of electrons on nitrogen does not take part in the aromatic ring structure. Electronegativity of nitrogen is greater than carbon

which generates a dipole moment in the vinylpyridine molecule that allows easy protonation of pyridine. This property of pyridine (pyridinium cations) is used in complex formation with metallic salts. The P4VP block can be easily modified by protonation, coordination chemistry, ionization and supramolecular chemistry, which allows additional control at nanoscale dimensions. Addition of small molecules by H-bonding (supramolecular chemistry) can allow the formation of nonporous materials. The additives can then be simply removed by dissolving in a suitable solvent. The supramolecular PS-*b*-P4VP BCP system has been well studied in bulk and in thin films. The small molecules are introduced to alter the relative volume fraction of the P4VP block inducing morphological changes to form a variety of hierarchical assemblies by intermolecular hydrogen bonding. Ikkala and ten Brinke and co-workers reported the bulk structures of PS-*b*-P4VP complexed with 3-*n*-pentadecyl phenol (PDP).<sup>101-106</sup> The sample preparation is very simple, the BCPs and small molecules are usually dissolved in organic solvents to obtain a low concentration solution and then annealed in suitable conditions. Stamm and coworkers studied thin films from the supramolecular assembly of PS-*b*-P4VP and 2-(4'-hydroxybenzeneazo) benzoic acid (HABA).<sup>78, 107-109</sup> Nonporous structures derived from PS-*b*-P4VP was also studied by using different additives: 4-*n*-nonadecylphenol (NDP),<sup>110</sup> 4-dodecylbenzenesulfonic acid (DBSA),<sup>111</sup> phosphoric acid (H<sub>3</sub>PO<sub>4</sub>),<sup>112</sup> fullerene (C<sub>60</sub>),<sup>113</sup> phenolic resin,<sup>114</sup> 1-pyrenebutyric acid,<sup>115</sup> 1-naphthol (NOH) and 1-napthoic acid (NCOOH),<sup>116-118</sup> the EDOT family: ((3,4-ethylenedioxythiophene) (EDOT), 3,4-(2,2-dimethylpropylenedioxy) thiophene (ProDOT), and hydroxymethyl -3,4-ethylenedioxythiophene (HMeDOT)),<sup>119</sup> and cholesteryl hemisuccinate (CholHS).<sup>120</sup> Lee et al, in 1988, reported one of the first examples of a nanoporous polymer from an ordered block copolymer.<sup>121</sup> In BCPs, nanoporous films can be made by removing one of the blocks by etching,<sup>122-124</sup> hydrolysis,<sup>125</sup> ozonolysis,<sup>126</sup> or by depolymerisation.<sup>127</sup> As an alternative to these

above mentioned harsh conditions, comparatively easy and mild conditions can be achieved by using noncovalent H-bonds to form the nanostructured materials.<sup>128</sup>

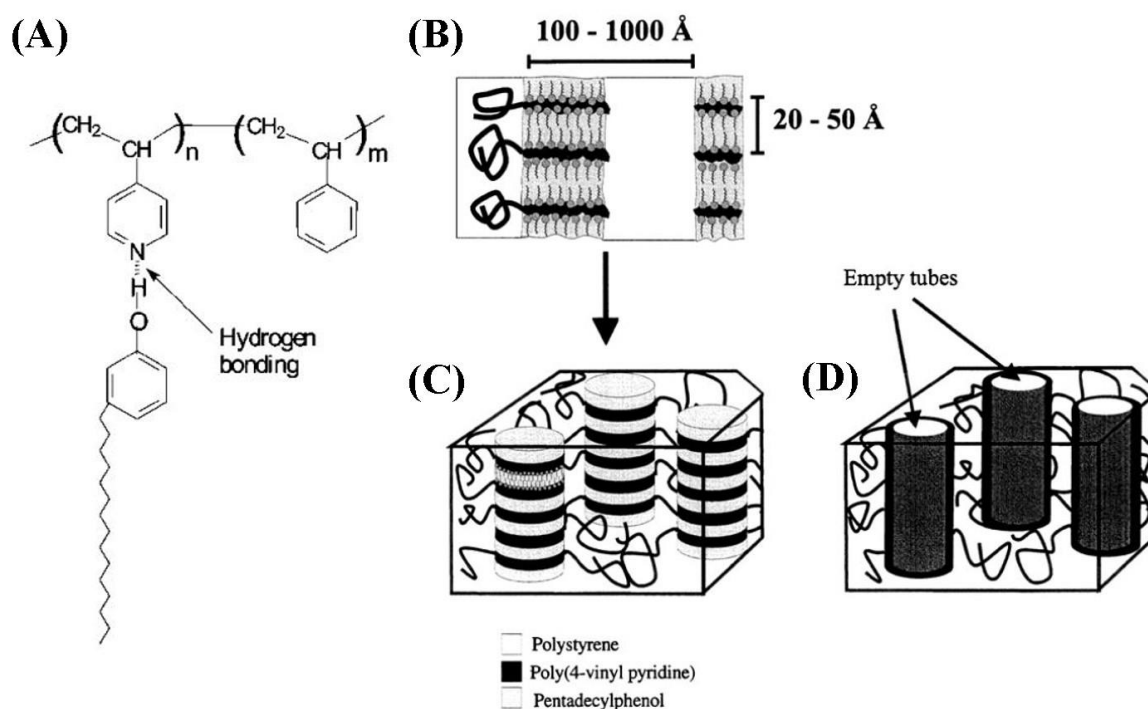


**Figure 1.10.** (A) H-bonded supramolecule obtained by intermolecular H-bonding between pentadecylphenol and PS-P4VP block copolymer. (B) Schematic representation of nanostructure material obtained. (C) Lamellar-within-cylindrical structure before PDP removal. (D) After PDP removal, the cylindrical structure is obtained under mild conditions. (Adapted from Ref. 102)

The H-bonding interaction between pyridine (from PS-*b*-P4VP) and phenol has been used. Pyridine acts as the H-bond acceptor whereas phenol acts as H-bond donor. As shown in Fig. 1.10, the self-assembly of block copolymers by using phenols resulted in formation of hierarchical porous structures. PS was used for the glassy rigid state and the P4VP block forms H-bonding with stoichiometric amounts of pentadecylphenol (PDP), which results in formation of comb coil diblock copolymer. The cylindrical morphology in a glassy rigid PS matrix was formed, where P4VP-PDP blocks were organized in a lamellar phase within the cylinders. In

the later stage, PDP was removed by washing, resulting in hollow cylinders with P4VP brushes on the walls. In the same way, different additives (listed above) can be used to generate nanoporous structures.

In another method, as reported by Ghoshal et al,<sup>129</sup> nanoporous structures can be generated by a simple solvation process rather than complex chemical co-ordination between precursor and one of the block of BCP, as shown in Fig. 1.11.<sup>130</sup>

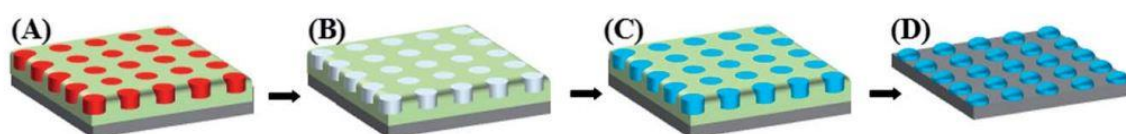


**Figure 1.11.** Schematic representation of the fabrication of oxide nanodots from (A) highly ordered self-assembled PS-*b*-PEO by solvent annealing method. (B) After activation of PEO cylinders. (C) Metal oxide precursor on top of the activated film by spin coating. (D) Oxide dots after UV/Ozone treatment. (Adapted from ref. 129)

As shown in Fig. 1.11, Ghoshal et al. used an asymmetric PS-*b*-PEO diblock copolymer to fabricate oxide nanodots on a silicon substrate. A BCP solution was prepared from toluene to yield a 0.9 wt% solution. A thin film was then fabricated by spin coating on to a silicon substrate. Solvent annealing was performed in mixed vapours of toluene-water (50:50, v/v) for 1 h. The phase segregated thin films were then immersed in ethanol to “activate” the film. It is unknown what this does but it appears to partially etch the PEO block leaving behind a partially nanoporous film. Different oxide nanodots were fabricated by dissolving the salt to form precursor solutions and spin coating on the nanoporous film. UV/Ozone treatment was used to oxidise the inorganic components in the film and also to remove the organic residues. Ghoshal et al.<sup>131</sup> have also reported the fabrication of nanowires by a similar inclusion technique as shown in Figure 1.12.

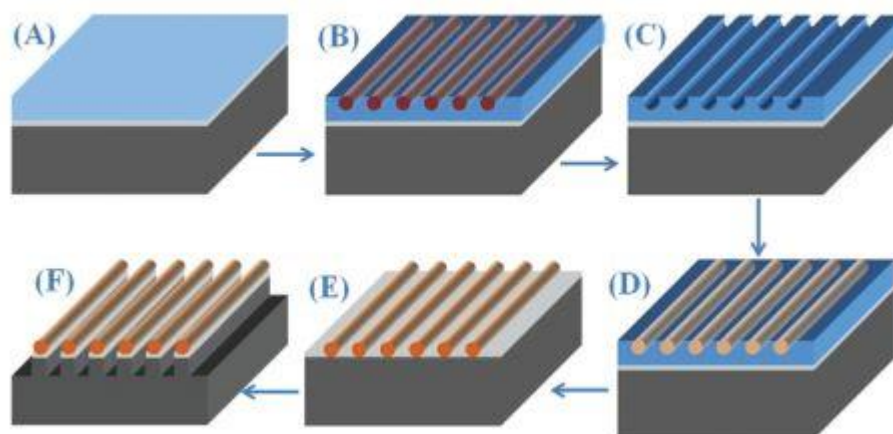


**Figure 1.12.** Schematic illustration of the fabrication of Si nanowires. (A) Spin coated PS-*b*-PEO BCP (B) Solvent annealed phase separated PEO cylinders parallel to the substrate in the PS matrix (C) Activation of PEO cylinders (D) Metal precursor solution spin coated on the activated film (E) After UV/Ozone treatment (F) Si nanowires fabrication by silica and silicon ICP etch process. (Adapted from ref. 131)

Solvent annealing of thin films of asymmetric PS-*b*-PEO systems in toluene produces hexagonally arranged PEO cylinders parallel to the substrate in PS matrix. These PEO cylinders can be activated to generate a nanoporous template for the metal ion inclusion. Iron oxide nanowires were then prepared by spin coating a metal ion precursor solution followed by UV/Ozone treatment. Si nanowires were fabricated by a sequential silica and silicon ICP etch respectively. A similar approach was used for the fabrication of Si nanowires by Cummins et al.<sup>132</sup> A cylinder forming asymmetric PS-*b*-P4VP block copolymer, with a P4VP minor component, phase separates upon solvent annealing and generates cylinder parallel to the substrate. After phase separation, the metal ion precursor solution was spin coated and the UV/Ozone treatment was used to oxidise the precursor to form oxide nanowires and remove the polymers. This was then followed by silica and silicon etching in a plasma chamber.

However, despite the success of these procedures the use of cylindrical structures is not considered ideal. The thickness of the films is limited to a single layer of cylinders and, further, the curved shapes formed are not ideal for pattern transfer to a substrate. Because of these limitations a lamellar form is considered ideal. This thesis addresses the development of a simple method to self-assemble lamellar block copolymers (BCPs) by a solvent annealing technique, to control the BCP-induced feature spacing, and to build nanostructure templates by using BCP thin films. For the first time, the inclusion process will be used for lamellar forming systems of very low dimension. In the following chapters, the fabrication strategies, experimental designs, and the characterization of the generated nanostructures will be presented. This thesis focuses on the study of the assembly of block copolymers as:

1. The morphological study of high  $\chi$  self-assembled BCPs in selective solvents.
2. Feature size control.
3. The application of BCPs to generate hard masks.
4. The fabrication of 2-dimensional (2D) materials

Specifically, this research focused on the self-assembly of lamellar forming poly (styrene)-*block*-poly-(4-vinylpyridine) (PS-*b*-P4VP).

In Chapter 2, the large molecular weight lamellar PS-*b*-P4VP block copolymer self-assembly by solvent vapour annealing is discussed. The microphase morphology and orientation control by a solvent effect is also shown.

In Chapter 3, feature size control of PS-*b*-P4VP block copolymer self-assembly is shown to generate sub 6-nm half pitch patterns. In this chapter the solvent influence on the structure, which is in contrast with large molecular weight, is discussed.

In Chapter 4, a novel, simple and *in situ* hard mask technology to generate metal oxide nanowires by block copolymer inclusion technique is discussed.



In Chapter 5, the 2D layered MoS<sub>2</sub> fabrication by using block copolymer self-assembly is discussed. By using large molecular weight PS-*b*-P4VP block copolymer, systematically MoO<sub>3</sub> nanowires are fabricated (which also can be used as hard masks). A simple sulfurization route was developed to form MoS<sub>2</sub> at different temperatures. By TEM analysis, a few layers of MoS<sub>2</sub> structure were fabricated.

Finally, the main conclusions of this work will be summarized and an outlook for their potential applications will be given in the final chapter.

## 1.5. References

1. Vlachopoulos, N.; Liska, P.; Augustynski, J.; Graetzel, M., Very efficient visible light energy harvesting and conversion by spectral sensitization of high surface area polycrystalline titanium dioxide films. *Journal of the American Chemical Society* **1988**, *110* (4), 1216-1220.
2. Siegel, R. W., Cluster-Assembled Nanophase Materials. *Annual Review of Materials Science* **1991**, *21* (1), 559-578.
3. Pascual, J. I.; Méndez, J.; Gómez-Herrero, J.; Baró, A. M.; Garcia, N.; Landman, U.; Luedtke, W. D.; Bogachek, E. N.; Cheng, H.-P., Properties of Metallic Nanowires: From Conductance Quantization to Localization. *Science* **1995**, *267* (5205), 1793-1795.
4. Murray, C. B.; Kagan, C. R.; Bawendi, M. G., Self-Organization of CdSe Nanocrystallites into Three-Dimensional Quantum Dot Superlattices. *Science* **1995**, *270* (5240), 1335-1338.
5. Landauer, R., Conductance determined by transmission: probes and quantised constriction resistance. *Journal of Physics: Condensed Matter* **1989**, *1* (43), 8099.
6. Heath, J. R., The Chemistry of Size and Order on a Nanometer Scale. *Science* **1995**, *270* (5240), 1315-1316.
7. Dresselhaus, M. S., Physics and chemistry of nanometer-scale materials: Symposium summary, looking outward and beyond. *Materials Science and Engineering: B* **1993**, *19* (1-2), 192-197.
8. Yuan, J.; Müller, A. H. E., One-dimensional organic-inorganic hybrid nanomaterials. *Polymer* **2010**, *51* (18), 4015-4036.

9. Xia, Y.; Yang, P.; Sun, Y.; Wu, Y.; Mayers, B.; Gates, B.; Yin, Y.; Kim, F.; Yan, H., One-Dimensional Nanostructures: Synthesis, Characterization, and Applications. *Advanced Materials* **2003**, *15* (5), 353-389.
10. Harriott, L. R., Limits of lithography. *Proceedings of the IEEE* **2001**, *89* (3), 366-374.
11. International Technology Roadmap for Semiconductor. 2013 Edition.
12. International Technology Roadmap for Semiconductor. 2013 Edition. Executive summary. 6.
13. de Diaz, S. L. M.; Fowler, J. W.; Pfund, M. E.; Mackulak, G. T.; Hickie, M., Evaluating the impacts of reticle requirements in semiconductor wafer fabrication. *Semiconductor Manufacturing, IEEE Transactions on* **2005**, *18* (4), 622-632.
14. Netto, B., Caves of the thousand Buddhas: Chinese art from the Silk Route. By Roderrick Whitfield and Anne Farrer. with contributions by S.J. Vainker and Jessica Rawson. Edited by Anne Farrer. pp. 208. front., 151 col., 75 bl. and wh. illus. London, British Museum Publications, 1990. £19.95. *Journal of the Royal Asiatic Society (Third Series)* **1992**, *2* (01), 129-131.
15. Ronan, C., The Shorter Science and Civilisation in China. *Cambridge University Press* **1994**, *4*.
16. Rees, F., Johannes Gutenberg: Inventor of the Printing Press. *Compass Point Books* **2006**.
17. Colta, I., The Print in the Nineteenth Century. *Heilbrunn Timeline of Art History. New York: The Metropolitan Museum of Art* **2004**, 2000.

18. Meggs, P. B.; Purvis, A. W., *Meggs' history of graphic design*. John Wiley & Sons: Hoboken, N.J., 2012.
19. Weaver, P., *The technique of lithography*. Batsford: London, 1964.
20. Carter, K. R., An Age-Old Printing Process Goes Nano. *ACS Nano* **2010**, *4* (2), 595-598.
21. Thompson, L. F.; Kerwin, R. E., Polymer Resist Systems for Photo- And Electron Lithography. *Annual Review of Materials Science* **1976**, *6* (1), 267-301.
22. Levenson, M. D.; Viswanathan, N. S.; Simpson, R. A., Improving resolution in photolithography with a phase-shifting mask. *Electron Devices, IEEE Transactions on* **1982**, *29* (12), 1828-1836.
23. Dill, F. H., Optical lithography. *Electron Devices, IEEE Transactions on* **1975**, *22* (7), 440-444.
24. Henderson, R. C., Device fabrication by electron-beam lithography. In *Electron-Beam Technology in Microelectronic Fabrication*, Brewer, G. R., Ed. Academic Press: 1980; pp 217-257.
25. Rai-Choudhury, P., SPIE Handbook of Microlithography, Micromachining and Microfabrication. *Volume 1: Microlithography*.
26. Chang, T. H. P.; Mankos, M.; Lee, K. Y.; Muray, L. P., Multiple electron-beam lithography. *Microelectronic Engineering* **2001**, 57–58, 117-135.
27. Rastogi, A.; Paik, M. Y.; Tanaka, M.; Ober, C. K., Direct Patterning of Intrinsically Electron Beam Sensitive Polymer Brushes. *ACS Nano* **2010**, *4* (2), 771-780.

28. Chou, S. Y.; Krauss, P. R.; Renstrom, P. J., Nanoimprint lithography. *Journal of Vacuum Science & Technology B* **1996**, *14* (6), 4129-4133.
29. Chou, S. Y.; Krauss, P. R.; Zhang, W.; Guo, L.; Zhuang, L., Sub-10 nm imprint lithography and applications. *Journal of Vacuum Science & Technology B* **1997**, *15* (6), 2897-2904.
30. Chou, S. Y.; Krauss, P. R.; Renstrom, P. J., Imprint Lithography with 25-Nanometer Resolution. *Science* **1996**, *272* (5258), 85-87.
31. Chou, S. Y.; Krauss, P. R.; Renstrom, P. J., Imprint of sub-25 nm vias and trenches in polymers. *Applied Physics Letters* **1995**, *67* (21), 3114-3116.
32. Chou, S. Y.; Krauss, P. R., Imprint lithography with sub-10 nm feature size and high throughput. *Microelectronic Engineering* **1997**, *35* (1-4), 237-240.
33. Greener, J.; Li, W.; Ren, J.; Voicu, D.; Pakhareenko, V.; Tang, T.; Kumacheva, E., Rapid, cost-efficient fabrication of microfluidic reactors in thermoplastic polymers by combining photolithography and hot embossing. *Lab on a Chip* **2010**, *10* (4), 522-524.
34. Weimin, Z.; Guoquan, M.; Jing, Z.; Yanbo, L.; Jinhe, W.; Yanping Zhang, Feng, S., Nanoimprint lithography: a processing technique for nanofabrication advancement. *Nano-Micro Letters* **2011**, *3* (2), 135-140.
35. Khandpur, A. K.; Foerster, S.; Bates, F. S.; Hamley, I. W.; Ryan, A. J.; Bras, W.; Almdal, K.; Mortensen, K., Polyisoprene-Polystyrene Diblock Copolymer Phase Diagram near the Order-Disorder Transition. *Macromolecules* **1995**, *28* (26), 8796-8806.
36. Hamley, I. W., Ordering in thin films of block copolymers: Fundamentals to potential applications. *Progress in Polymer Science* **2009**, *34* (11), 1161-1210.

37. Bates, F.; Fredrickson, G., Block Copolymers - Designer Soft Materials. *Phys. Today* **1999**, 52 (2), 32-38.
38. Hamley, I. W., *The physics of block copolymers*. Oxford University Press: Oxford, 1998.
39. Szwarc, M.; Levy, M.; Milkovich, R., Polymerization Initiated by Electron Transfer to Monomer. A new method of formation of block copolymers. *Journal of the American Chemical Society* **1956**, 78 (11), 2656-2657.
40. Grosius, P.; Gallot, Y.; Skoulios, A., Synthèse et propriétés des copolymères séquences styrène-vinylpyridine. Étude des structures mésomorphes obtenues en milieu solvant préférentiel. *European Polymer Journal* **1970**, 6 (2), 355-361.
41. Flory, P. J., *Principles of Polymer Chemistry*. Cornell University Press: 1953.
42. Russell, T. P.; Hjelm, R. P.; Seeger, P. A., Temperature dependence of the interaction parameter of polystyrene and poly(methyl methacrylate). *Macromolecules* **1990**, 23 (3), 890-893.
43. Helfand, E. W., Z. R., Developments in Block Copolymers-1, Chapter 4. *Applied Science, London* **1982**, I. Goodman, Ed.
44. Helfand, E.; Wasserman, Z. R., Block Copolymer Theory. 4. Narrow Interphase Approximation. *Macromolecules* **1976**, 9 (6), 879-888.
45. Helfand, E., Block Copolymer Theory. III. Statistical Mechanics of the Microdomain Structure. *Macromolecules* **1975**, 8 (4), 552-556.
46. Leibler, L., Theory of Microphase Separation in Block Copolymers. *Macromolecules* **1980**, 13 (6), 1602-1617.

47. Matsen, M. W., The standard Gaussian model for block copolymer melts. *Journal of Physics: Condensed Matter* **2002**, *14* (2), R21.
48. Matsen, M. W.; Schick, M., Self-assembly of block copolymers. *Current Opinion in Colloid & Interface Science* **1996**, *1* (3), 329-336.
49. Matsen, M. W.; Schick, M., Stable and unstable phases of a diblock copolymer melt. *Physical Review Letters* **1994**, *72* (16), 2660-2663.
50. Matsen, M. W.; Bates, F. S., Unifying Weak- and Strong-Segregation Block Copolymer Theories. *Macromolecules* **1996**, *29* (4), 1091-1098.
51. Matsen, M. W.; Bates, F. S., Origins of Complex Self-Assembly in Block Copolymers. *Macromolecules* **1996**, *29* (23), 7641-7644.
52. Böker, A.; Müller, A. H. E.; Krausch, G., Nanoscopic Surface Patterns from Functional ABC Triblock Copolymers. *Macromolecules* **2001**, *34* (21), 7477-7488.
53. Huang, H.; Zhang, F.; Hu, Z.; Du, B.; He, T.; Lee, F. K.; Wang, Y.; Tsui, O. K. C., Study on the Origin of Inverted Phase in Drying Solution-Cast Block Copolymer Films. *Macromolecules* **2003**, *36* (11), 4084-4092.
54. Zhang, X.; Berry, B. C.; Yager, K. G.; Kim, S.; Jones, R. L.; Satija, S.; Pickel, D. L.; Douglas, J. F.; Karim, A., Surface Morphology Diagram for Cylinder-Forming Block Copolymer Thin Films. *ACS Nano* **2008**, *2* (11), 2331-2341.
55. Zhang, X.; Douglas, J. F.; Jones, R. L., Influence of film casting method on block copolymer ordering in thin films. *Soft Matter* **2012**, *8* (18), 4980-4987.

56. Schubert, D.; Dunkel, T., Spin coating from a molecular point of view: its concentration regimes, influence of molar mass and distribution. *Mat Res Innovat* **2003**, 7 (5), 314-321.
57. Muller-Buschbaum, P.; S. Gutmann, J.; Stamm, M., Dewetting of confined polymer films: an X-ray and neutron scattering study. *Physical Chemistry Chemical Physics* **1999**, 1 (17), 3857-3863.
58. Limary, R.; Green, P. F., Dewetting Instabilities in Thin Block Copolymer Films: Nucleation and Growth. *Langmuir* **1999**, 15 (17), 5617-5622.
59. Hamley, I. W.; Hiscutt, E. L.; Yang, Y. W.; Booth, C., Dewetting of Thin Block Copolymer Films. *Journal of Colloid and Interface Science* **1999**, 209 (1), 255-260.
60. Maaloum, M.; Ausserre, D.; Chatenay, D.; Coulon, G.; Gallot, Y., Edge profile of relief 2D domains at the free surface of smectic copolymer thin films. *Physical Review Letters* **1992**, 68 (10), 1575-1578.
61. Zalusky, A. S.; Olayo-Valles, R.; Wolf, J. H.; Hillmyer, M. A., Ordered Nanoporous Polymers from Polystyrene–Polylactide Block Copolymers. *Journal of the American Chemical Society* **2002**, 124 (43), 12761-12773.
62. Ren, Y.; Lodge, T. P.; Hillmyer, M. A., Synthesis, Characterization, and Interaction Strengths of Difluorocarbene-Modified Polystyrene–Polyisoprene Block Copolymers. *Macromolecules* **2000**, 33 (3), 866-876.
63. Zhao, Y.; Sivaniah, E.; Hashimoto, T., SAXS Analysis of the Order–Disorder Transition and the Interaction Parameter of Polystyrene-block-poly(methyl methacrylate). *Macromolecules* **2008**, 41 (24), 9948-9951.



64. Cochran, E. W.; Morse, D. C.; Bates, F. S., Design of ABC Triblock Copolymers near the ODT with the Random Phase Approximation. *Macromolecules* **2003**, *36* (3), 782-792.
65. Dai, K. H.; Kramer, E. J., Determining the temperature-dependent Flory interaction parameter for strongly immiscible polymers from block copolymer segregation measurements. *Polymer* **1994**, *35* (1), 157-161.
66. Alberda van Ekenstein, G. O. R.; Meyboom, R.; ten Brinke, G.; Ikkala, O., Determination of the Flory–Huggins Interaction Parameter of Styrene and 4-Vinylpyridine Using Copolymer Blends of Poly(styrene-co-4-vinylpyridine) and Polystyrene. *Macromolecules* **2000**, *33* (10), 3752-3756.
67. Mansky, P.; Russell, T. P.; Hawker, C. J.; Mays, J.; Cook, D. C.; Satija, S. K., Interfacial Segregation in Disordered Block Copolymers: Effect of Tunable Surface Potentials. *Physical Review Letters* **1997**, *79* (2), 237-240.
68. Yokoyama, H.; Kramer, E. J.; Rafailovich, M. H.; Sokolov, J.; Schwarz, S. A., Structure and Diffusion of Asymmetric Diblock Copolymers in Thin Films: A Dynamic Secondary Ion Mass Spectrometry Study. *Macromolecules* **1998**, *31* (25), 8826-8830.
69. Yokoyama, H.; Kramer, E. J., Mutual Diffusion of Asymmetric Block Copolymers with Homopolymers. *Macromolecules* **2000**, *33* (5), 1871-1877.
70. Sinturel, C.; Vayer, M.; Morris, M.; Hillmyer, M. A., Solvent Vapor Annealing of Block Polymer Thin Films. *Macromolecules* **2013**, *46* (14), 5399-5415.
71. Cavicchi, K. A.; Berthiaume, K. J.; Russell, T. P., Solvent annealing thin films of poly(isoprene-b-lactide). *Polymer* **2005**, *46* (25), 11635-11639.

72. Zettl, U.; Knoll, A.; Tsarkova, L., Effect of Confinement on the Mesoscale and Macroscopic Swelling of Thin Block Copolymer Films. *Langmuir* **2010**, *26* (9), 6610-6617.
73. Di, Z.; Posselt, D.; Smilgies, D.-M.; Papadakis, C. M., Structural Rearrangements in a Lamellar Diblock Copolymer Thin Film during Treatment with Saturated Solvent Vapor. *Macromolecules* **2010**, *43* (1), 418-427.
74. Kim, S. H.; Misner, M. J.; Xu, T.; Kimura, M.; Russell, T. P., Highly Oriented and Ordered Arrays from Block Copolymers via Solvent Evaporation. *Advanced Materials* **2004**, *16* (3), 226-231.
75. Kim, G.; Libera, M., Kinetic Constraints on the Development of Surface Microstructure in SBS Thin Films. *Macromolecules* **1998**, *31* (8), 2670-2672.
76. Kim, G.; Libera, M., Morphological Development in Solvent-Cast Polystyrene–Polybutadiene–Polystyrene (SBS) Triblock Copolymer Thin Films. *Macromolecules* **1998**, *31* (8), 2569-2577.
77. Bosworth, J. K.; Paik, M. Y.; Ruiz, R.; Schwartz, E. L.; Huang, J. Q.; Ko, A. W.; Smilgies, D.-M.; Black, C. T.; Ober, C. K., Control of Self-Assembly of Lithographically Patternable Block Copolymer Films. *ACS Nano* **2008**, *2* (7), 1396-1402.
78. Tokarev, I.; Krenek, R.; Burkov, Y.; Schmeisser, D.; Sidorenko, A.; Minko, S.; Stamm, M., Microphase Separation in Thin Films of Poly(styrene-block-4-vinylpyridine) Copolymer–2-(4'-Hydroxybenzeneazo)benzoic Acid Assembly. *Macromolecules* **2005**, *38* (2), 507-516.

79. Lai, C.; Russel, W. B.; Register, R. A., Scaling of Domain Spacing in Concentrated Solutions of Block Copolymers in Selective Solvents. *Macromolecules* **2002**, *35* (10), 4044-4049.
80. Niu, S.; Saraf, R. F., Stability of Order in Solvent-Annealed Block Copolymer Thin Films. *Macromolecules* **2003**, *36* (7), 2428-2440.
81. Jung, Y. S.; Ross, C. A., Solvent-Vapor-Induced Tunability of Self-Assembled Block Copolymer Patterns. *Advanced Materials* **2009**, *21* (24), 2540-2545.
82. Cavicchi, K. A.; Russell, T. P., Solvent Annealed Thin Films of Asymmetric Polyisoprene–Polylactide Diblock Copolymers. *Macromolecules* **2007**, *40* (4), 1181-1186.
83. Gotrik, K. W.; Ross, C. A., Solvothermal Annealing of Block Copolymer Thin Films. *Nano Letters* **2013**, *13* (11), 5117-5122.
84. Paik, M. Y.; Bosworth, J. K.; Smilges, D.-M.; Schwartz, E. L.; Andre, X.; Ober, C. K., Reversible Morphology Control in Block Copolymer Films via Solvent Vapor Processing: An in Situ GISAXS Study. *Macromolecules* **2010**, *43* (9), 4253-4260.
85. Wang, J.-Y.; Chen, W.; Roy, C.; Sievert, J. D.; Russell, T. P., Influence of Ionic Complexes on Phase Behavior of Polystyrene-*b*-poly(methyl methacrylate) Copolymers. *Macromolecules* **2008**, *41* (3), 963-969.
86. Lin, Z. Q.; Kim, D. H.; Wu, X. D.; Boosahda, L.; Stone, D.; LaRose, L.; Russell, T. P., A Rapid Route to Arrays of Nanostructures in Thin Films. *Advanced Materials* **2002**, *14* (19), 1373-1376.
87. Cummins, C.; Kelly, R. A.; Gangnaik, A.; Georgiev, Y. M.; Petkov, N.; Holmes, J. D.; Morris, M. A., Solvent Vapor Annealing of Block Copolymers in Confined Topographies:

Commensurability Considerations for Nanolithography. *Macromolecular Rapid Communications* **2015**, *36* (8), 762-767.

88. Cummins, C.; Borah, D.; Rasappa, S.; Chaudhari, A.; Ghoshal, T.; O'Driscoll, B. M. D.; Carolan, P.; Petkov, N.; Holmes, J. D.; Morris, M. A., Self-assembly of polystyrene-block-poly(4-vinylpyridine) block copolymer on molecularly functionalized silicon substrates: fabrication of inorganic nanostructured etchmask for lithographic use. *Journal of Materials Chemistry C* **2013**, *1* (47), 7941-7951.

89. Knoll, A.; Lyakhova, K. S.; Horvat, A.; Krausch, G.; Sevink, G. J. A.; Zvelindovsky, A. V.; Magerle, R., Direct imaging and mesoscale modelling of phase transitions in a nanostructured fluid. *Nat Mater* **2004**, *3* (12), 886-891.

90. Seppala, J. E.; Lewis, R. L.; Epps, T. H., Spatial and Orientation Control of Cylindrical Nanostructures in ABA Triblock Copolymer Thin Films by Raster Solvent Vapor Annealing. *ACS Nano* **2012**, *6* (11), 9855-9862.

91. Knoll, A.; Horvat, A.; Lyakhova, K. S.; Krausch, G.; Sevink, G. J. A.; Zvelindovsky, A. V.; Magerle, R., Phase Behavior in Thin Films of Cylinder-Forming Block Copolymers. *Physical Review Letters* **2002**, *89* (3), 035501.

92. Albert, J. N. L.; Bogart, T. D.; Lewis, R. L.; Beers, K. L.; Fasolka, M. J.; Hutchison, J. B.; Vogt, B. D.; Epps, T. H., Gradient Solvent Vapor Annealing of Block Copolymer Thin Films Using a Microfluidic Mixing Device. *Nano Letters* **2011**, *11* (3), 1351-1357.

93. Tang, C.; Lennon, E. M.; Fredrickson, G. H.; Kramer, E. J.; Hawker, C. J., Evolution of Block Copolymer Lithography to Highly Ordered Square Arrays. *Science* **2008**, *322* (5900), 429-432.

94. Bitá, I.; Yang, J. K. W.; Jung, Y. S.; Ross, C. A.; Thomas, E. L.; Berggren, K. K., Graphoepitaxy of Self-Assembled Block Copolymers on Two-Dimensional Periodic Patterned Templates. *Science* **2008**, *321* (5891), 939-943.
95. Jeong, J. W.; Park, W. I.; Kim, M.-J.; Ross, C. A.; Jung, Y. S., Highly Tunable Self-Assembled Nanostructures from a Poly(2-vinylpyridine-*b*-dimethylsiloxane) Block Copolymer. *Nano Letters* **2011**, *11* (10), 4095-4101.
96. Jung, Y. S.; Ross, C. A., Orientation-Controlled Self-Assembled Nanolithography Using a Polystyrene–Polydimethylsiloxane Block Copolymer. *Nano Letters* **2007**, *7* (7), 2046-2050.
97. Förster, S.; Antonietti, M., Amphiphilic Block Copolymers in Structure-Controlled Nanomaterial Hybrids. *Advanced Materials* **1998**, *10* (3), 195-217.
98. Antonietti, M.; Heinz, S.; Schmidt, M.; Rosenauer, C., Determination of the Micelle Architecture of Polystyrene/Poly(4-vinylpyridine) Block Copolymers in Dilute Solution. *Macromolecules* **1994**, *27* (12), 3276-3281.
99. Klingelhöfer, S.; Heitz, W.; Greiner, A.; Oestreich, S.; Förster, S.; Antonietti, M., Preparation of Palladium Colloids in Block Copolymer Micelles and Their Use for the Catalysis of the Heck Reaction. *Journal of the American Chemical Society* **1997**, *119* (42), 10116-10120.
100. Förster, S.; Zisenis, M.; Wenz, E.; Antonietti, M., Micellization of strongly segregated block copolymers. *The Journal of Chemical Physics* **1996**, *104* (24), 9956-9970.
101. Ruokolainen, J.; Saariaho, M.; Ikkala, O.; ten Brinke, G.; Thomas, E. L.; Torkkeli, M.; Serimaa, R., Supramolecular Routes to Hierarchical Structures: Comb-Coil Diblock Copolymers Organized with Two Length Scales. *Macromolecules* **1999**, *32* (4), 1152-1158.

102. Mäki-Ontto, R.; de Moel, K.; de Odorico, W.; Ruokolainen, J.; Stamm, M.; ten Brinke, G.; Ikkala, O., "Hairy Tubes": Mesoporous Materials Containing Hollow Self-Organized Cylinders with Polymer Brushes at the Walls. *Advanced Materials* **2001**, *13* (2), 117-121.
103. Polushkin, E.; Alberda van Ekenstein, G. O. R.; Knaapila, M.; Ruokolainen, J.; Torkkeli, M.; Serimaa, R.; Bras, W.; Dolbnya, I.; Ikkala, O.; ten Brinke, G., Intermediate Segregation Type Chain Length Dependence of the Long Period of Lamellar Microdomain Structures of Supramolecular Comb-Coil Diblocks. *Macromolecules* **2001**, *34* (14), 4917-4922.
104. Valkama, S.; Ruotsalainen, T.; Nykänen, A.; Laiho, A.; Kosonen, H.; ten Brinke, G.; Ikkala, O.; Ruokolainen, J., Self-Assembled Structures in Diblock Copolymers with Hydrogen-Bonded Amphiphilic Plasticizing Compounds. *Macromolecules* **2006**, *39* (26), 9327-9336.
105. de Moel, K.; Alberda van Ekenstein, G. O. R.; Nijland, H.; Polushkin, E.; ten Brinke, G.; Mäki-Ontto, R.; Ikkala, O., Polymeric Nanofibers Prepared from Self-Organized Supramolecules. *Chemistry of Materials* **2001**, *13* (12), 4580-4583.
106. Ruotsalainen, T.; Turku, J.; Hiekkataipale, P.; Vainio, U.; Serimaa, R.; Brinke, G. t.; Harlin, A.; Ruokolainen, J.; Ikkala, O., Tailoring of the hierarchical structure within electrospun fibers due to supramolecular comb-coil block copolymers: polystyrene-block-poly(4-vinyl pyridine) plasticized by hydrogen bonded pentadecylphenol. *Soft Matter* **2007**, *3* (8), 978-985.
107. Sidorenko, A.; Tokarev, I.; Minko, S.; Stamm, M., Ordered Reactive Nanomembranes/Nanotemplates from Thin Films of Block Copolymer Supramolecular Assembly. *Journal of the American Chemical Society* **2003**, *125* (40), 12211-12216.

108. Böhme, M.; Kuila, B.; Schlörb, H.; Nandan, B.; Stamm, M., Thin films of block copolymer supramolecular assemblies: Microphase separation and nanofabrication. *physica status solidi (b)* **2010**, *247* (10), 2458-2469.
109. Nandan, B.; Vyas, M. K.; Böhme, M.; Stamm, M., Composition-Dependent Morphological Transitions and Pathways in Switching of Fine Structure in Thin Films of Block Copolymer Supramolecular Assemblies. *Macromolecules* **2010**, *43* (5), 2463-2473.
110. Ruokolainen, J.; Brinke, G. t.; Ikkala, O., Supramolecular Polymeric Materials with Hierarchical Structure-Within-Structure Morphologies. *Advanced Materials* **1999**, *11* (9), 777-780.
111. Kosonen, H.; Valkama, S.; Ruokolainen, J.; Torkkeli, M.; Serimaa, R.; ten Brinke, G.; Ikkala, O., One-dimensional optical reflectors based on self-organization of polymeric comb-shaped supramolecules. *Eur. Phys. J. E* **2003**, *10* (1), 69-75.
112. Tiitu, M.; Torkkeli, M.; Serimaa, R.; Mäkelä, T.; Ikkala, O. T., Self-assembly and flow alignment of protonically conducting complexes of polystyrene-block-poly(4-vinylpyridine) diblock copolymer with phosphoric acid. *Solid State Ionics* **2005**, *176* (13–14), 1291-1299.
113. Laiho, A.; Ras, R. H. A.; Valkama, S.; Ruokolainen, J.; Österbacka, R.; Ikkala, O., Control of Self-Assembly by Charge-Transfer Complexation between C60 Fullerene and Electron Donating Units of Block Copolymers. *Macromolecules* **2006**, *39* (22), 7648-7653.
114. Valkama, S.; Nykänen, A.; Kosonen, H.; Ramani, R.; Tuomisto, F.; Engelhardt, P.; ten Brinke, G.; Ikkala, O.; Ruokolainen, J., Hierarchical Porosity in Self-Assembled Polymers: Post-Modification of Block Copolymer–Phenolic Resin Complexes by Pyrolysis Allows the Control of Micro- and Mesoporosity. *Advanced Functional Materials* **2007**, *17* (2), 183-190.

115. Kuila, B. K.; Gowd, E. B.; Stamm, M., Supramolecular Assembly of Poly(styrene)-b-poly(4-vinylpyridine) and 1-Pyrenebutyric Acid in Thin Film and Their Use for Nanofabrication. *Macromolecules* **2010**, *43* (18), 7713-7721.
116. Roland, S.; Gaspard, D.; Prud'homme, R. E.; Bazuin, C. G., Morphology Evolution in Slowly Dip-Coated Supramolecular PS-b-P4VP Thin Films. *Macromolecules* **2012**, *45* (13), 5463-5476.
117. Roland, S.; Pellerin, C.; Bazuin, C. G.; Prud'homme, R. E., Evolution of Small Molecule Content and Morphology with Dip-Coating Rate in Supramolecular PS-P4VP Thin Films. *Macromolecules* **2012**, *45* (19), 7964-7972.
118. Roland, S.; Prud'homme, R.; Bazuin, C. G., Supramolecular PS-P4VP diblock copolymer thin films slowly dip-coated from chloroform solutions. *Sci. China Chem.* **2013**, *56* (1), 33-39.
119. Hagaman, D.; Enright, T. P.; Sidorenko, A., Block Copolymer Supramolecular Assembly beyond Hydrogen Bonding. *Macromolecules* **2012**, *45* (1), 275-282.
120. Korhonen, J. T.; Verho, T.; Rannou, P.; Ikkala, O., Self-Assembly and Hierarchies in Pyridine-Containing Homopolymers and Block Copolymers with Hydrogen-Bonded Cholesteric Side-Chains. *Macromolecules* **2010**, *43* (3), 1507-1514.
121. Lee, J. S.; Hirao, A.; Nakahama, S., Polymerization of monomers containing functional silyl groups. 5. Synthesis of new porous membranes with functional groups. *Macromolecules* **1988**, *21* (1), 274-276.
122. Crossland, E. J. W.; Kamperman, M.; Nedelcu, M.; Ducati, C.; Wiesner, U.; Smilgies, D. M.; Toombes, G. E. S.; Hillmyer, M. A.; Ludwigs, S.; Steiner, U.; Snaith, H. J., A Bicontinuous Double Gyroid Hybrid Solar Cell. *Nano Letters* **2009**, *9* (8), 2807-2812.



123. Crossland, E. J. W.; Nedelcu, M.; Ducati, C.; Ludwigs, S.; Hillmyer, M. A.; Steiner, U.; Snaith, H. J., Block Copolymer Morphologies in Dye-Sensitized Solar Cells: Probing the Photovoltaic Structure–Function Relation. *Nano Letters* **2009**, *9* (8), 2813-2819.
124. Park, S.; Wang, J.-Y.; Kim, B.; Xu, J.; Russell, T. P., A Simple Route to Highly Oriented and Ordered Nanoporous Block Copolymer Templates. *ACS Nano* **2008**, *2* (4), 766-772.
125. Joo, W.; Yang, S. Y.; Kim, J. K.; Jinnai, H., Nanohole Structure Prepared by a Polystyrene-block-poly(methyl methacrylate)/poly(methyl methacrylate) Mixture Film. *Langmuir* **2008**, *24* (21), 12612-12617.
126. Mansky, P.; Harrison, C. K.; Chaikin, P. M.; Register, R. A.; Yao, N., Nanolithographic templates from diblock copolymer thin films. *Applied Physics Letters* **1996**, *68* (18), 2586-2588.
127. Li, M.; Douki, K.; Goto, K.; Li, X.; Coenjarts, C.; Smilgies, D. M.; Ober, C. K., Spatially Controlled Fabrication of Nanoporous Block Copolymers. *Chemistry of Materials* **2004**, *16* (20), 3800-3808.
128. Ikkala, O.; ten Brinke, G., Functional Materials Based on Self-Assembly of Polymeric Supramolecules. *Science* **2002**, *295* (5564), 2407-2409.
129. Ghoshal, T.; Shaw, M. T.; Bolger, C. T.; Holmes, J. D.; Morris, M. A., A general method for controlled nanopatterning of oxide dots: a microphase separated block copolymer platform. *Journal of Materials Chemistry* **2012**, *22* (24), 12083-12089.
130. Yun, S.-H.; Sohn, B.-H.; Jung, J. C.; Zin, W.-C.; Lee, J.-K.; Song, O., Tunable Magnetic Arrangement of Iron Oxide Nanoparticles in Situ Synthesized on the Solid Substrate from Diblock Copolymer Micelles. *Langmuir* **2005**, *21* (14), 6548-6552.

131. Ghoshal, T.; Senthamaraikannan, R.; Shaw, M. T.; Holmes, J. D.; Morris, M. A., Fabrication of Ordered, Large Scale, Horizontally-Aligned Si Nanowire Arrays Based on an In Situ Hard Mask Block Copolymer Approach. *Advanced Materials* **2014**, *26* (8), 1207-1216.

132. Cummins, C.; Gangnaik, A.; Kelly, R. A.; Borah, D.; O'Connell, J.; Petkov, N.; Georgiev, Y. M.; Holmes, J. D.; Morris, M. A., Aligned silicon nanofins via the directed self-assembly of PS-b-P4VP block copolymer and metal oxide enhanced pattern transfer. *Nanoscale* **2015**, *7* (15), 6712-6721.

# 2

## The Effect of Solvent Vapour Annealing Conditions on the Thin Film Morphologies of Lamellar Forming Polystyrene-*block*-Poly(4-vinylpyridine) Block Copolymers

---

### 2.1. Abstract

In this work, we report a very simple and efficient method to form lamellar structures of symmetric polystyrene-*block*-poly(4-vinylpyridine) (PS-*b*-P4VP) BCP thin films with vertical (to the surface plane) orientated lamellae using a solvent annealing approach. The methodology does not require any brush chemistry to engineer a neutral surface and it is the block neutral nature of the film-solvent vapour interface that defined the orientation of the lamellae. The microphase separated structure of two different molecular weight lamellar forming PS-*b*-P4VP block copolymers formed under solvent vapour annealing was monitored using atomic force microscopy (AFM) so as to understand morphology changes of the film under solvent exposure. In particular, the morphology changed from micellar structures to well-defined microphase separated arrangements. The choice of solvent (single and dual solvent exposure) and the solvent annealing conditions had important effects on morphology of the films and it was found that a block neutral solvent was required to realize vertically aligned P4VP lamellae. The results of exposure of phase separated films to ethanol are also described.

### 2.2. Introduction

Block copolymers (BCPs) of two or more chemically immiscible polymer chains can, under certain conditions, phase separate to form well-ordered morphologies with feature sizes of around 5 to 50 nm in thin films.<sup>1</sup> BCPs may be one of the most useful classes of nanomaterials

because of their ability to self-assemble and subsequently template organic, inorganic, semiconducting, metallic or biologically relevant materials.<sup>2-11</sup> The BCP equilibrium, self-assembled structures that can form are lamellar, cylindrical, spherical as well as more complex gyroid and other 3D arrangements depending on their composition. The domain and spacing sizes of the patterns varies with block molecular weight. The Flory-Huggins interaction parameter ( $\chi$ ), a measure of block chemical dissimilarity, combined with the degree of polymerization ( $N$ ) dictates if the structure will formed will be ordered<sup>12, 13</sup> with a  $\chi N$  value of  $>10.5$  needed for the spontaneous formation of microphase separated structures.<sup>14, 15</sup> Spin-coating from dilute solvent onto flat substrates is the most convenient method of thin film formation but the as-spun films are usually in a non-equilibrium state due to the competition between microphase separation and vitrification as solvent evaporation proceeds.<sup>16</sup> Self-assembly of BCPs can be achieved through annealing the BCP thin film under a suitable environment, either at elevated temperature using thermal annealing<sup>17, 18</sup> or by annealing in solvent vapour.<sup>19-25</sup> Of particular interest here is solvent vapour annealing (SVA) since well-defined film patterns can be achieved at much lower process temperatures/times than thermal annealing. In solvent annealing, the solvent vapour permeates, swells and separates the polymer chains providing mobility by lowering the effective glass transition temperature.

Because of their potential as an “on-chip” etch mask in integrated circuit manufacture, orientational control (i.e. direction vertical or parallel to the substrate plane) is a critical issue.<sup>26, 27</sup> This can be challenging particularly for lamellar systems where preferential interface interactions and surface energies can result in horizontal orientations and/or preferential wetting layers.<sup>28</sup> Examples include polystyrene-*b*-polymethylmethacrylate (PS-*b*-PMMA) which is well studied for device applications but requires a well-defined random polymer brush layer on top of the silicon substrate to provide ideally oriented patterns.<sup>29</sup> Polystyrene-*b*-polydimethylsiloxane (PS-*b*-PDMS) is another potential material for circuit fabrication but

generally requires a carefully controlled brush layer or substrate molecular functionalization.<sup>30</sup> Other potential solutions include “capping layers” but a simple method was first demonstrated by Libera and co-workers,<sup>31</sup> that solvent evaporation upon casting could orientate asymmetric, cylinder-forming during solvent evaporation. However, this mechanism is not clear and other authors suggest that the chemistry of the solvent vapour at the polymer surface drives orientational control.<sup>25</sup>

An ideal line-forming BCP pattern for circuit fabrication would be lamellar-forming (since pattern transfer from cylindrical arrangements is challenging)<sup>27</sup> and have high  $\chi$  (since they can phase separate into small domain size/spacings, have smaller inter-domain diffusion regions and produce patterns with less defects). The use of high- $\chi$  BCPs is, however, challenging since it is difficult to ensure perpendicular orientation of the blocks to the substrate plane and, further, obtaining well-ordered, defect free patterns can be kinetically slow.<sup>32</sup> At room temperature, the  $\chi$  parameter of PS-*b*-P4VP ( $\chi \sim 0.34$ )<sup>33</sup> is considerably higher than those of PS-*b*-PDMS ( $\chi \sim 0.26$ ),<sup>34</sup> PS-*b*-PMMA ( $\chi \sim 0.06$ ),<sup>35</sup> PS-*b*-P2VP ( $\chi \sim 0.18$ ),<sup>36</sup> PS-*b*-PEO ( $\chi \sim 0.08$ ).<sup>37</sup> Further, the surface energies of PS and P4VP are similar and so limit phase separation at interfaces<sup>38</sup> whilst the functionality of the block is ideal for inclusion of inorganics for enhancement of etch contrast. Thus, the PS-*b*-P4VP system has significant potential in device fabrication. However, the self-assembly of lamellar forming systems of high  $\chi$  is challenging due to a strong tendency towards micelle formation in number of common polymer solvents such as toluene.<sup>39</sup> Indeed, this strong micellization has been used for the incorporation of metals and semiconducting materials into the P4VP core in solvents favouring PS.<sup>40,41</sup> Sohn and co-workers<sup>42</sup> have shown long range lateral ordering of PS-*b*-P4VP micelles is possible. Generally, the micelles formed by lamellar PS-*b*-P4VP are robust and resistant to both thermal and solvent annealing and in order to form microphase separated domain structures, careful attention to the selection of both casting and annealing solvents is required.<sup>16</sup>

SVA methodologies are well developed. This chapter extends the understanding of SVA by extension to an important BCP which shows very strong tendency to form micelles in both solution and thin films and provides details of a robust solvent annealing method to form periodic, orientationally controlled, lamellar structures and provide understanding of the nature of the SVA solvent needed to affect these arrangements.

## 2.3. Experimental

### 2.3.1. Materials

Two different PS-*b*-P4VP BCPs were purchased from Polymer Source Inc. (Montreal, Canada). Table 2.1 shows the molecular characteristics of the polymers used in this work. BCP were used without any further purification. Reagent grade toluene, tetrahydrofuran (THF) and ethanol were purchased from Sigma-Aldrich.

**Table 2.1.** Molecular characteristics of the PS-*b*-P4VP Diblock Copolymer

Polymer	Total $M_n$ ( $\times 10^3$ g/mol)	$M_w/M_n$	P4VP fraction	BCP morphology (*)
PS <sub>20k</sub> - <i>b</i> -P4VP <sub>17k</sub>	37.0	1.08	0.46	L
PS <sub>9k</sub> - <i>b</i> -P4VP <sub>9.2k</sub>	18.2	1.09	0.51	L

\*L= Lamellae forming

### 2.3.2. Thin film preparation, solvent annealing and characterization

The polymers used were generally dissolved in toluene-THF mixtures to yield 0.5 weight % solutions and were stirred overnight at room temperature to ensure complete solution. A toluene-THF (80/20, v:v) mixture was found to be the optimum composition providing periodic arrangements in short times (see below). Substrates were silicon (100) wafers with an interfacial oxide of 2 nm and were cleaned by sonicating for 15 min in toluene, followed by 10 min in THF and then dried under a stream of nitrogen. A final cleaning using a UV/ozone

treatment for 15 min was performed. The cleaning procedure lowered the water contact angle significantly ( $36^\circ$  for bare silicon and  $0^\circ$  for UV/ozone cleaned) making the surface more hydrophilic. This resulted in a more uniform, high coverage thin film presumably due to increased affinity to the P4VP block. Thin films of required thickness were prepared by spin-coating the polymer solutions onto the substrates at 3000 rpm for 30 s using a Speciality Coating Systems G3P-8 spin-coater. Solvent annealing was used to generate well-defined periodic structures. The samples were placed in a glass bottle (100 mL size) containing a smaller vial holding 10 mL of solvent. As-cast samples were then solvent annealed at  $50^\circ\text{C}$  for a range of different times (30 min to 6 h). The annealed samples were immediately removed from the vials and kept at room temperature for few minutes to ensure the rapid and complete evaporation of the solvent. The rapid removal time was used so that swollen features were kinetically “frozen-in” for analysis. All samples were analysed using atomic force microscopy (AFM, Park Systems XE-100) and topographic images were collected in non-contact tapping mode. Secondary electron microscopy (SEM, FEI Inspect F) was also used as an imaging method.

## 2.4 Results and Discussion

### 2.4.1 Micellization of PS-*b*-P4VP

A 0.5 wt% solution used here for spin casting is well above the known critical micelle solution for PS-*b*-P4VP ( $0.065\text{ mgmL}^{-1}$ ) and strong spherical micellization is expected when dissolved in toluene.<sup>43</sup> Because of the preferential interaction of toluene with the PS block the micelles have a PS corona and the P4VP block in the core.<sup>44</sup> When the casting solution is spin-coated on the substrate surface, these micelles survive spin coating/solvent evaporation and in the conditions used here, form a monolayer of densely packed, robust hemi-micelles on the substrate surface and form a disordered hexagonal arrangement (Figure 2.1(A)). In the AFM

image, lighter colours correspond to the P4VP block and the darker colour to PS. The formation of strong spherical micellization in these mixtures is observed by the bluish translucent colour of the polymer solution.<sup>45</sup> Below, 0.5 wt% casting solution concentrations, the micelles become progressively less densely packed and it is possible to resolve the micelle structure using SEM (0.3 wt%). In Figure 2.1(B), the micelles do not cover the whole surface and open areas of the substrate can be seen. At higher resolution, Figure 2.1(C), a densely packed P4VP core can be clearly observed as a bright sphere with the less densely packed PS corona seen as tendrils extending across the substrate. It can be seen that the PS component has collapsed to the substrate either the result of surface interactions and/or the removal of the solvent.

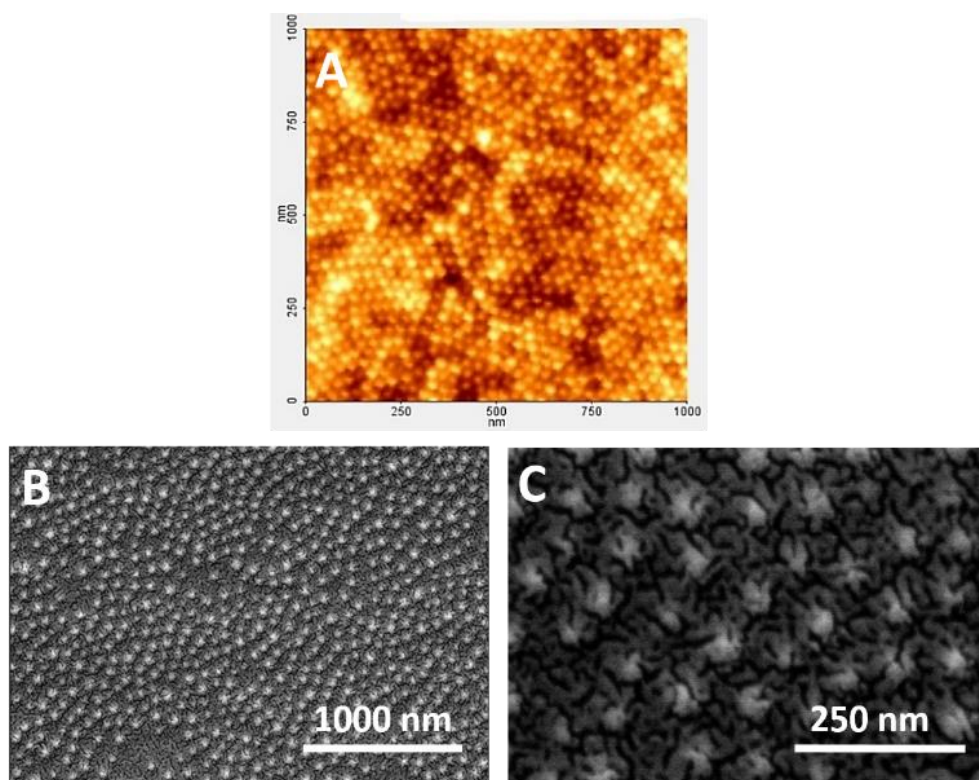


**Figure 2.1.** AFM images of a PS<sub>20k</sub>-*b*-P4VP<sub>17k</sub> thin films, 0.5 wt% casting solution (A). (B) and (C) are SEM images of similar films formed at 0.3 wt%. The micelle nature of the film can be very clearly seen in (C).



### 2.4.2 Microphase separation by solvent selective annealing

In order to rearrange these films into microphase separated structures, extensive annealing was needed. Thermal annealing was not very effective and instead solvent annealing was found to be much more efficacious. As previously reported,<sup>16</sup> the choice of solvent is dictated by the materials' solvent parameter. For these strongly micelle forming systems, it is suggested that a solvent that is effectively neutral (favours both blocks) is required as this negates micelle formation. The Hildebrand solubility parameter can be used to indicate the similarity of the solvent to a polymer and, hence, solubility.<sup>46</sup> However, for the PS-*b*-P4VP system this approach is somewhat over simple since P4VP has considerable polarity. In this case, the Hansen solubility parameters are more useful providing estimates of individual contributions for dispersive (van der Waals), polar and hydrogen bonding.<sup>47</sup> Table 2.2 lists known Hansen solubility parameters for the materials used here. Toluene is poor solvent for the P4VP block because of its low polarity but a reasonable solvent for PS, THF is a good solvent for the P4VP block because of the good match with both its polarity and hydrogen bonding. Overall, it could be argued, that THF appears to be a better solvent for the block copolymer than toluene alone (since it has a reasonably similar dispersion component to PS as well as a polar component for THF) and hence it was used as the primary component in the casting solutions described above.

**Table 2.2.** Hansen Solubility Parameters (MPa<sup>1/2</sup> for Relevant Materials)

Material	$\delta_d$	$\delta_p$	$\delta_h$
Toluene	18.0	1.4	2.0
THF	16.8	5.7	8.0
Ethanol	15.8	8.8	19.4
PS	18.6	0.2	0.0
P4VP	18.1	6.8	7.2
PS- <i>b</i> -P4VP	19.3	5.9	0.9

Note to table: Hansen Solubility Parameters were taken from various sources.<sup>48-50</sup>

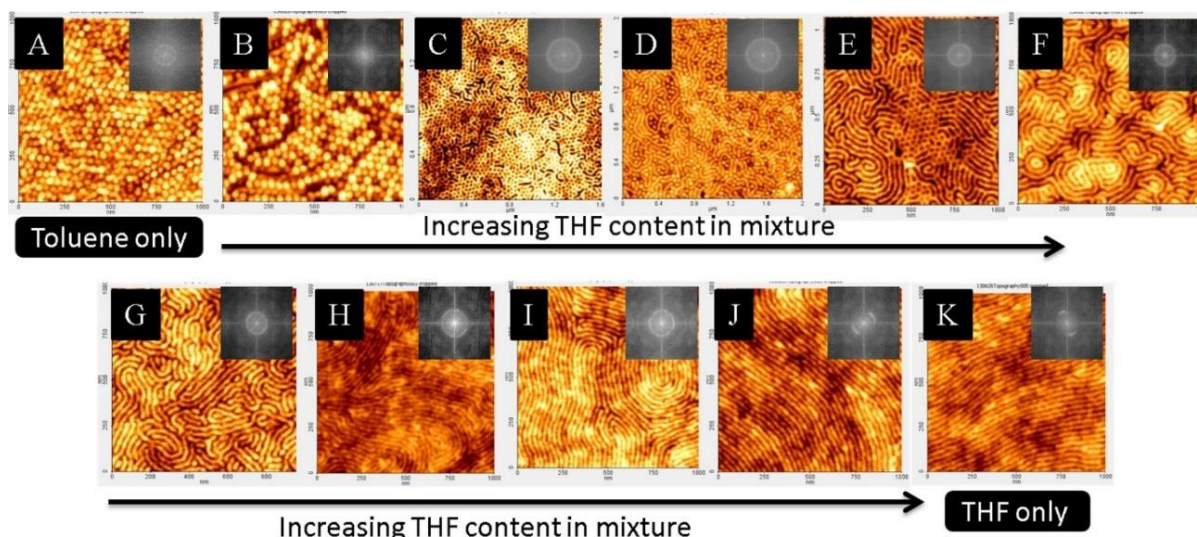


**Figure 2.2.** Topographic AFM images ( $1 \times 1 \mu\text{m}$ ) of  $\text{PS}_{9\text{k}}\text{-}b\text{-P4VP}_{9.2\text{k}}$  cast from toluene/THF (80/20) and solvent annealed at  $50\text{ }^\circ\text{C}$  for 4 h in different saturated solvent vapour environments of: (A) pure toluene, (B) toluene/THF = 90/10, (C) toluene/THF = 80/20, (D) toluene/THF = 70/30, (E) toluene/THF = 60/40, (F) toluene/THF = 50/50, (G) toluene/THF = 40/60, (H) toluene/THF = 30/70, (I) toluene/THF = 20/80, (J) toluene/THF = 10/90 and (K) pure THF. All solvent compositions are given as (v/v). FFT patterns inset show the difference in the degree of order.

The more neutral nature of THF can be verified by the AFM data presented in Figure 2.2 where the results of solvent annealing a  $\text{PS}_{9\text{k}}\text{-}b\text{-P4VP}_{9.2\text{k}}$  BCP in various toluene/THF mixtures ( $50\text{ }^\circ\text{C}$ , 4 h). In Figure 2.2 (A-K), there is a distinct change of morphology from micelle structures to well-defined microphase separated arrangements. For convenience, the solvent vapour annealing (SVA) conditions can be divided into three distinct regions: (I) SVA in pure toluene, (II) SVA in toluene rich mixture of toluene/THF and (III) SVA in a THF rich mixture.

#### **SVA in pure toluene (Figure (2.2A)):**

As postulated earlier, solvent annealing in toluene is ineffective in altering the morphology of the as-cast films from their micelle type structure because it is a poor solvent for the P4VP

block. The mean spacing for both as-cast and solvent annealed micelles remains unchanged as measured by AFM (~28 nm). The BCP forms a P4VP rich core and a PS corona because of the favourable interactions of the polymer for the PS block. Even extended annealing periods of 24 h had no measurable effect on film morphology. It should be noted that whilst the morphology is largely unaltered, changes in the order of the micelle arrangement can be seen with significantly greater order seen after solvent annealing. Larger areas of a well-defined hexagonal arrangement can be seen compared to the image in Figure 2.1(A). This is evidenced by the changes in the FFT (Fast Fourier Transform) data.

### **SVA in a toluene rich mixture of toluene/THF (Figure 2.2(B-F)):**

The addition of even small amounts of THF to the toluene, solvent annealing procedure had a noticeable effect on the morphology. A 90/10 (v/v) mixture did not alter the morphology but changes in spacing and apparent feature size can be seen with increase in micellar size to around 29 nm consistent with some swelling of the P4VP core by the addition of THF. Note, that although the swelling is not directly observed its effect is seen by inclusion of free volume caused by rapid solvent loss during removal from the chamber. Further addition of THF (80/20, v/v), Figure 2.2(C) begins to transform the micelle structure into a structure suggestive of a microphase separated arrangement with a change in height variation across the substrate decreasing from 5-6 nm for micelle structures to 2-3 nm for the phase separated like patterns. The image seen in Figure 2.2(C) is more complex than might be imagined since both lines and cylinder or sphere arrangements can be seen. It seems unlikely that enough solvent swelling is seen to result in a gross composition change to form either cylinder or spherical microphase separated structures. In AFM, the lighter regions of the image are due to the P4VP block and it would appear that this initial structure represents a transition between a micelle arrangement and a microphase separated structure and might be a type of perforated lamellar structure with PS lamellae changing orientation so as to emerge from the surface.<sup>51-53</sup> At compositions of

70/30 and 60/40 v/v (Figure 2.2(D) and 2.2(E)), the structure becomes more regular with regions of a lamellar-like pattern emerging together with remnants of the hexagonal spherical/cylinder arrangement. At a 50/50 (v/v) ratio of toluene/THF (Figure 2.2(F)), the lamellar phase extends across the entire substrate and any ‘dot’ like structures can be described as defects within the gross morphology. It is also worth stressing that in these studies we saw no evidence of a microphase separated lamellar structure oriented parallel to the surface plane. This suggests that the use of the THF as a co-solvent in the anneal process provides a ‘neutral’ interface that promotes vertical orientation of the lamellae.

### **SVA in THF rich mixture (Figure 2.2(G-K))**

Between 50% and 100% v/v THF the lamellar arrangement is maintained. The only noticeable visual change is an increase of the persistence length of the aligned domains and an increase in ‘grain size’. At 90% and 100% THF, the persistence length exceeds 100 nm. The reason for the well-ordered nature of the system clearly relates to the neutrality of the THF solvent which lowers the interactions between the PS and P4VP by effectively separating blocks and increasing chain mobility, allowing defect annihilation.<sup>25</sup> This would contrast a more block selective system since this would primarily result in selective block swelling whilst maintaining block-to-block interfaces. The domain-to-domain spacing was estimated at 25 nm. This is significantly lower than for spacings observed with toluene rich SVA and this is consistent with reduced THF swelling of the PS component compared to toluene as suggested by the data in Table 2.2. It, thus, appears that THF is an ‘ideal’ annealing solvent for this PS-*b*-P4VP system.

It should also be noted that both the kinetics of phase separation and the equilibrium structure are modified by solvents because of the effective vapour pressures during solvent annealing. It is important to note that at 50 °C these two solvents have quite different saturated vapour

pressures with measured values of 93.7 mm Hg and 435 mm Hg for toluene and THF, respectively. Since this is an ideal solution, Raoult's law<sup>54</sup> is obeyed and can be used to sketch the expected vapour pressure through the composition range (Figure 2.3(A)) and the amount of THF in the vapour phase (Figure 2.3(B)). As can be seen, increased THF content results in increased vapour pressure of THF compared to toluene. One manifestation of this is seen in increasing thickness of the films as measured by ellipsometry. As cast films and toluene annealed films have a measured thickness of 26 nm but as the THF content increases, the film thickness increases to 30 nm. It is suggested this is because of increased swelling during solvent annealing followed by rapid de-swelling of the films on exposure to atmosphere. This results in increased (trapped) free volume as the film becomes kinetically 'frozen' and a higher film thickness compared to less swollen films.

The data in Figure 2.3 also helps to explain the variation in morphology observed across the whole concentration range because even at low THF liquid content, the vapour is highly enriched in THF. This explains the dramatic change in morphology at low THF content and the consistency (little change with toluene content) of the morphological data at higher THF content (Figure 2.2).

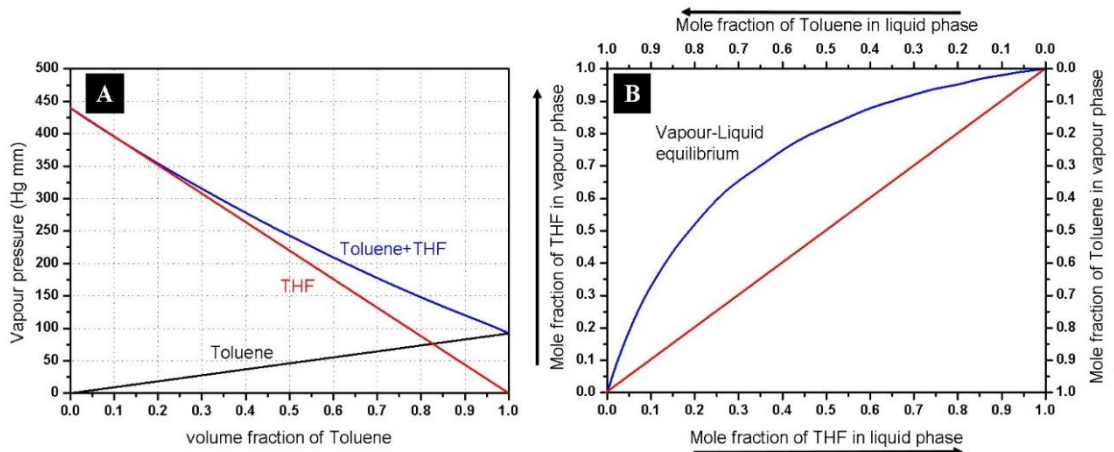


**Figure 2.3.** (A) The vapour pressures of a solution of the two liquids, toluene and THF at 50 °C, is the sum of the two individual vapour pressures, calculated by Raoult’s law. (B) Vapour-Liquid equilibrium diagram of toluene and THF mixture.

Similar dependence on composition was seen for the larger molecular weight PS<sub>20k</sub>-*b*-P4VP<sub>17k</sub> system but is not reported here for brevity.

### 2.4.3. Solvent vapour annealing with time

It is also important to explore the kinetics of the SVA process. Similar results were seen for both BCPs and data shown in Figure 2.4 of the PS<sub>20k</sub>-*b*-P4VP<sub>17k</sub> are indicative of the microphase separation of both systems. Figure 2.4 describes the effects of SVA time of thin films spin-coated from 0.5 wt% solutions of PS<sub>20k</sub>-*b*-P4VP<sub>17k</sub> from toluene/THF (80/20) and solvent annealed in THF. As-cast film thickness was 28 nm measured by ellipsometry and had the expected dried micellar structure (Figure 2.4(A)). After a SVA period of 30 min (Figure 2.4(B)), it is clear that the swelling of the films leads to merging of the P4VP cores and the formation of elongated micelle structures. Note that the size of the spherical micelles in Figure 2.4(A) is 35 nm by AFM and where visible in Figure 2.4(B) are generally about half the diameter of similar structures seen after extended solvent annealing and the elongated micelles seen in Figure 2.4(B) Note, however that a few more swollen spherical structures can also be

seen. The data suggest that at the lower SVA times that the film is not completely swollen by the THF and that Fig. 2.4B represents a rearrangement sponsored by the swelling. Note that it is assumed the swollen morphology is maintained due to freezing-in of the structure during rapid solvent evaporation.

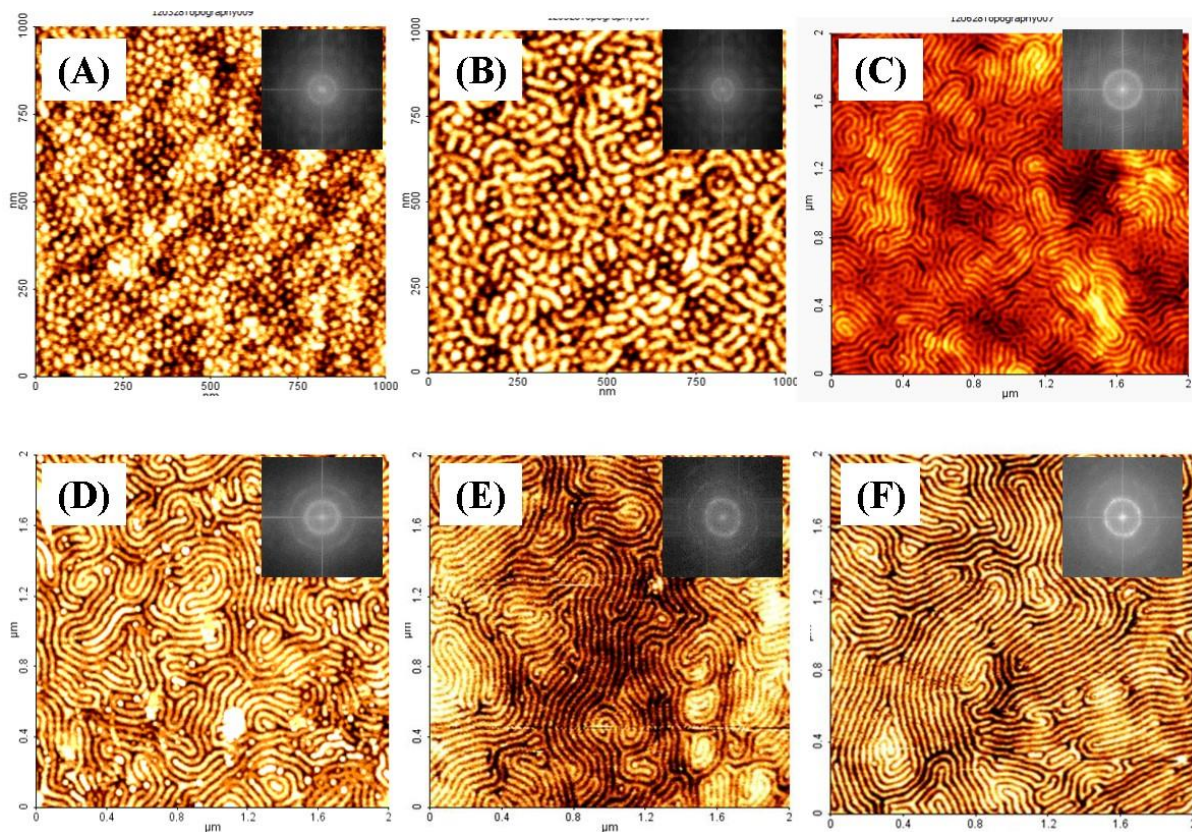


**Figure 2.4.** AFM images of as-spun (A) PS<sub>20k</sub>-P4VP<sub>17k</sub> thin film casted from toluene/THF (80/20) and solvent annealed (B-F) PS<sub>20k</sub>-P4VP<sub>17k</sub> films at 50 °C for different time in THF vapour: (B)30 min, (C) 1h, (D) 2h, (E) 3h and (F) 6h. The lamellar domain structures are perpendicular to a substrate. FFT patterns inset show the difference in the degree of order.

After a solvent annealing time of 1 h (Figure 2.4(C)), the micelle type structure has now transitioned to a distinct lamellar microphase separated pattern across most of the substrate with only isolated regions of dot like structures. This phase transition is likely related to the degree of swelling. At low swelling, short SVA times; micelles survive (from spin-coating) because chain mobility is low. As the initial time increases, solvent swelling increases causing

chain mobility and attaining the equilibrium phase-separated structure. With further increase in solvent annealing time (Figures 2.4(D-F)), the film becomes flat with increasing order and lower defectivity as the annealing time is increased. The thickness of the solvent annealed film after 6 h is measured at 31 nm and is consistent with an increased free volume as seen above. The domain spacing is 35 nm as measured by AFM. Note that these films are significantly less well ordered than those formed by similar treatment of the lower molecular weight PS-*b*-P4VP (compare Figure 2.4(F)) and Figure 2.2(K). This is thought to be because of diffusion limitations of the longer chains.

#### 2.4.4. BCP reconstruction with ethanol

PS-*b*-P4VP films are often subject to ethanol treatment to cause ‘reconstruction’. This process is used to enhance the etching contrast between both PS and P4VP blocks as well providing a template for insertion of metal ions into the P4VP block.<sup>55</sup> In light of the SVA studies here it was thought worthwhile to extend the work to ethanol. Ethanol is a non-acidic polar solvent which selectively swells the P4VP block (table 2.2). The pyridine groups present in P4VP are non-ionized and can interact with ethanol via hydrogen bonding. Due to the weak hydrogen bonding it is not expected that the P4VP block is chemically decomposed or removed from the BCP (since the covalent bond strength is high) but is more likely to swell and provide larger feature sizes than the lamella formed after solvent annealing. As shown in Fig. 2.5, a number of 3 h solvent annealed microphase separated PS<sub>9k</sub>-P4VP<sub>9.2k</sub> thin film are reconstructed by immersing them in anhydrous ethanol for different times (between 2 and 20 min) to study the swelling (and/or solubility) behaviour of the P4VP block. When the PS<sub>9k</sub>-P4VP<sub>9.2k</sub> film is immersed in ethanol for 2 min (Fig 2.5-A) followed by drying under nitrogen gas, the P4VP domains become partially swollen and the centre-to-centre distance between lamella is increased from 25 to 26 nm, by AFM, compared to a PS<sub>9k</sub>-P4VP<sub>9.2k</sub> thin film which did not



receive an ethanol exposure. During further reconstruction (in ethanol) for times between 5 and 20 min (Fig 2.5(B-E)) the P4VP chains further swell to 30 nm. It is also clear that at these extended exposures ethanol sufficiently swells P4VP domain and can lead to local areas of the pattern where the structure is damaged (black areas in the AFM images). The damage appears to relate to some dissolution of chains and probably results from the swollen chains weakening the polymer-substrate attachment (delamination). As exposure increases and particularly at a longer swelling time (~20 min or more), due to high degree of swelling, the surface of the BCP layer became increasingly rough as significant material is delaminated.

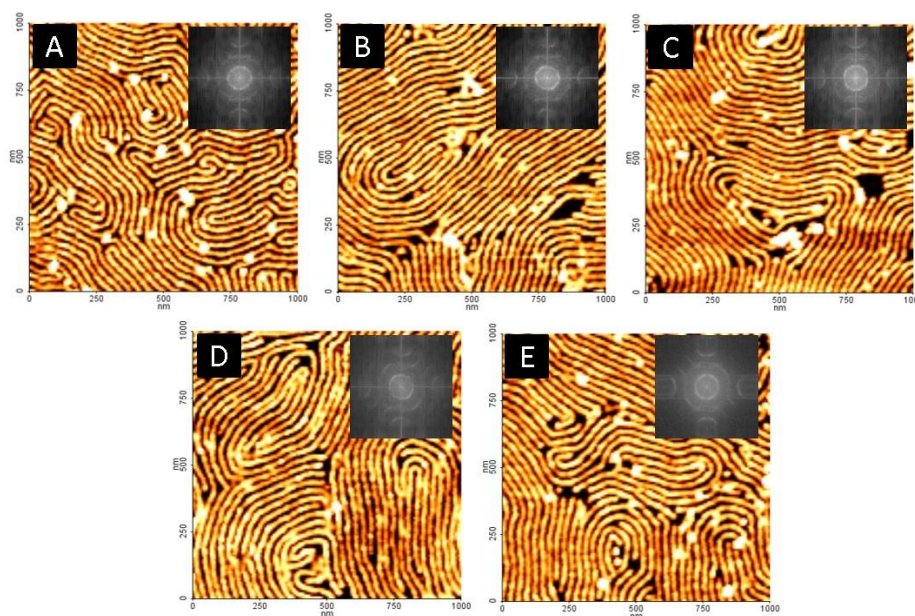


**Figure 2.5.** Topographic AFM images (1  $\mu\text{m}$  x 1  $\mu\text{m}$ ) of reconstructed PS<sub>9k</sub>-P4VP<sub>9.2k</sub> thin films for different time in ethanol for (A) 2min, (B) 5min, (C) 7min, (D) 10min and (E) 20min respectively. FFT patterns (inset) show the difference in the degree of order.

## 2.5 Conclusions

In this work it was found that extended SVA of micellar PS-*b*-P4VP films in THF vapour results in well-defined microphase separated structures. This work contrasts dramatically with previous work by Kim et al.<sup>56</sup> who have reported that when toluene cast PS-*b*-P4VP thin films

containing micelles are solvent annealed in THF there are morphological changes but micelle structures persist. Our observations are consistent with the THF being a good solvent for the BCP and somewhat neutral in its interactions with both blocks. The agreement of the phase behaviour and the THF Hansen solubility parameters with those of PS-*b*-P4VP is consistent with this mechanism. It must be stressed that PS-*b*-P4VP Hansen parameters are not well-established and over analysis is possible. There is generally a paucity of high quality data on both solvent parameters and interaction parameters for these PS-*b*-P4VP systems (as well as other BCPs) despite the considerable research work in this area.

One of the main differences in the work of Kim et al<sup>56</sup> and here is the solvent annealing temperature (25 °C and 50 °C respectively) and differences may be explained by variation of these terms with temperature. However we can conclude that THF solvent annealing can be used to generate well-defined arrangements of PS-*b*-P4VP lamellar structures and ordain long range order and vertical orientation of the lamellae to the surface plane. For these high- $\chi$  systems, it does appear that solvent annealing in neutral solvents is important in generating well-defined arrangements. The method is robust and reliable and offers a simple means to generate these structures with possibly important applications of device fabrication. Cylinder forming PS-*b*-P4VP has been shown to be applicable in this area<sup>55, 57, 58</sup> but lamellar systems have advantages compared to cylindrical structures.<sup>28</sup>

## 2.6 References

1. Bates, F. S.; Fredrickson, G. H., Block Copolymer Thermodynamics: Theory and Experiment. *Annual Review of Physical Chemistry* **1990**, *41* (1), 525-557.
2. Chai, J.; Wang, D.; Fan, X.; Buriak, J. M., Assembly of aligned linear metallic patterns on silicon. *Nat Nano* **2007**, *2* (8), 500-506.
3. Ghoshal, T.; Senthamaraiyannan, R.; Shaw, M. T.; Holmes, J. D.; Morris, M. A., "In situ" hard mask materials: a new methodology for creation of vertical silicon nanopillar and nanowire arrays. *Nanoscale* **2012**, *4* (24), 7743-7750.
4. Gu, X.; Dorsey, P.; Russell, T. P., High Density and Large Area Arrays of Silicon Oxide Pillars with Tunable Domain Size for Mask Etch Applications. *Advanced Materials* **2012**, *24* (40), 5505-5511.
5. Kim, D. H.; Jia, X.; Lin, Z.; Guarini, K. W.; Russell, T. P., Growth of Silicon Oxide in Thin Film Block Copolymer Scaffolds. *Advanced Materials* **2004**, *16* (8), 702-706.
6. Kim, D. H.; Kim, S. H.; Lavery, K.; Russell, T. P., Inorganic Nanodots from Thin Films of Block Copolymers. *Nano Letters* **2004**, *4* (10), 1841-1844.
7. Kim, D. H.; Sun, Z.; Russell, T. P.; Knoll, W.; Gutmann, J. S., Organic-Inorganic Nanohybridization by Block Copolymer Thin Films. *Advanced Functional Materials* **2005**, *15* (7), 1160-1164.
8. Li, X.; Lau, K. H. A.; Kim, D. H.; Knoll, W., High-Density Arrays of Titania Nanoparticles Using Monolayer Micellar Films of Diblock Copolymers as Templates. *Langmuir* **2005**, *21* (11), 5212-5217.

9. Spatz, J. P.; Mössmer, S.; Hartmann, C.; Möller, M.; Herzog, T.; Krieger, M.; Boyen, H.-G.; Ziemann, P.; Kabius, B., Ordered Deposition of Inorganic Clusters from Micellar Block Copolymer Films. *Langmuir* **2000**, *16* (2), 407-415.
10. Xu, J.; Hong, S. W.; Gu, W.; Lee, K. Y.; Kuo, D. S.; Xiao, S.; Russell, T. P., Fabrication of Silicon Oxide Nanodots with an Areal Density Beyond 1 Teradots Inch<sup>-2</sup>. *Advanced Materials* **2011**, *23* (48), 5755-5761.
11. Farrell, R.; Fitzgerald, T.; Borah, D.; Holmes, J.; Morris, M., Chemical Interactions and Their Role in the Microphase Separation of Block Copolymer Thin Films. *International Journal of Molecular Sciences* **2009**, *10* (9), 3671.
12. Herr, D. J. C., Directed block copolymer self-assembly for nanoelectronics fabrication. *Journal of Materials Research* **2011**, *26* (02), 122-139.
13. Kim, H.-C.; Park, S.-M.; Hinsberg, W. D., Block Copolymer Based Nanostructures: Materials, Processes, and Applications to Electronics. *Chemical Reviews* **2010**, *110* (1), 146-177.
14. Lodge, T. P.; Dalvi, M. C., Mechanisms of Chain Diffusion in Lamellar Block Copolymers. *Physical Review Letters* **1995**, *75* (4), 657-660.
15. Leibler, L., Theory of Microphase Separation in Block Copolymers. *Macromolecules* **1980**, *13* (6), 1602-1617.
16. O'Driscoll, S.; Demirel, G.; Farrell, R. A.; Fitzgerald, T. G.; O'Mahony, C.; Holmes, J. D.; Morris, M. A., The morphology and structure of PS-*b*-P4VP block copolymer films by solvent annealing: effect of the solvent parameter. *Polymers for Advanced Technologies* **2011**, *22* (6), 915-923.

17. Xiao, S.; Yang, X.; Edwards, E. W.; La, Y.-H.; Nealey, P. F., Graphoepitaxy of cylinder-forming block copolymers for use as templates to pattern magnetic metal dot arrays. *Nanotechnology* **2005**, *16* (7), S324.
18. Kim, H.-C.; Russell, T. P., Ordering in thin films of asymmetric diblock copolymers. *Journal of Polymer Science Part B: Polymer Physics* **2001**, *39* (6), 663-668.
19. Di, Z.; Posselt, D.; Smilgies, D.-M.; Papadakis, C. M., Structural Rearrangements in a Lamellar Diblock Copolymer Thin Film during Treatment with Saturated Solvent Vapor. *Macromolecules* **2010**, *43* (1), 418-427.
20. Xuan, Y.; Peng, J.; Cui, L.; Wang, H.; Li, B.; Han, Y., Morphology Development of Ultrathin Symmetric Diblock Copolymer Film via Solvent Vapor Treatment. *Macromolecules* **2004**, *37* (19), 7301-7307.
21. Gotrik, K. W.; Ross, C. A., Solvothermal Annealing of Block Copolymer Thin Films. *Nano Letters* **2013**, *13* (11), 5117-5122.
22. Peng, J.; Kim, D. H.; Knoll, W.; Xuan, Y.; Li, B.; Han, Y., Morphologies in solvent-annealed thin films of symmetric diblock copolymer. *The Journal of Chemical Physics* **2006**, *125* (6), 064702.
23. Lodge, T. P.; Pudil, B.; Hanley, K. J., The Full Phase Behavior for Block Copolymers in Solvents of Varying Selectivity. *Macromolecules* **2002**, *35* (12), 4707-4717.
24. Niu, S.; Saraf, R. F., Stability of Order in Solvent-Annealed Block Copolymer Thin Films. *Macromolecules* **2003**, *36* (7), 2428-2440.
25. Sinturel, C.; Vayer, M.; Morris, M.; Hillmyer, M. A., Solvent Vapor Annealing of Block Polymer Thin Films. *Macromolecules* **2013**, *46* (14), 5399-5415.

26. Bang, J.; Jeong, U.; Ryu, D. Y.; Russell, T. P.; Hawker, C. J., Block Copolymer Nanolithography: Translation of Molecular Level Control to Nanoscale Patterns. *Advanced Materials* **2009**, *21* (47), 4769-4792.
27. Morris, M. A., Directed self-assembly of block copolymers for nanocircuitry fabrication. *Microelectronic Engineering* **2015**, *132*, 207-217.
28. Stoykovich, M. P.; Nealey, P. F., Block copolymers and conventional lithography. *Materials Today* **2006**, *9* (9), 20-29.
29. Edwards, E. W.; Stoykovich, M. P.; Müller, M.; Solak, H. H.; de Pablo, J. J.; Nealey, P. F., Mechanism and kinetics of ordering in diblock copolymer thin films on chemically nanopatterned substrates. *Journal of Polymer Science Part B: Polymer Physics* **2005**, *43* (23), 3444-3459.
30. Borah, D.; Rasappa, S.; Senthamaraiannan, R.; Kosmala, B.; Shaw, M. T.; Holmes, J. D.; Morris, M. A., Orientation and Alignment Control of Microphase-Separated PS-*b*-PDMS Substrate Patterns via Polymer Brush Chemistry. *ACS Applied Materials & Interfaces* **2013**, *5* (1), 88-97.
31. Kim, G.; Libera, M., Morphological Development in Solvent-Cast Polystyrene–Polybutadiene–Polystyrene (SBS) Triblock Copolymer Thin Films. *Macromolecules* **1998**, *31* (8), 2569-2577.
32. Durand, W. J.; Blachut, G.; Maher, M. J.; Sirard, S.; Tein, S.; Carlson, M. C.; Asano, Y.; Zhou, S. X.; Lane, A. P.; Bates, C. M.; Ellison, C. J.; Willson, C. G., Design of high- $\chi$  block copolymers for lithography. *Journal of Polymer Science Part A: Polymer Chemistry* **2015**, *53* (2), 344-352.

33. Zha, W.; Han, C. D.; Lee, D. H.; Han, S. H.; Kim, J. K.; Kang, J. H.; Park, C., Origin of the Difference in Order–Disorder Transition Temperature between Polystyrene-*block*-poly(2-vinylpyridine) and Polystyrene-*block*-poly(4-vinylpyridine) Copolymers. *Macromolecules* **2007**, *40* (6), 2109-2119.
34. Nose, T., Coexistence curves of polystyrene/ poly(dimethylsiloxane) blends. *Polymer* **1995**, *36* (11), 2243-2248.
35. Bucholz, T. L.; Loo, Y.-L., Phase Behavior of Near-Monodisperse Semifluorinated Diblock Copolymers by Atom Transfer Radical Polymerization. *Macromolecules* **2006**, *39* (18), 6075-6080.
36. Hammond, M. R.; Cochran, E.; Fredrickson, G. H.; Kramer, E. J., Temperature Dependence of Order, Disorder, and Defects in Laterally Confined Diblock Copolymer Cylinder Monolayers. *Macromolecules* **2005**, *38* (15), 6575-6585.
37. Frielinghaus, H.; Hermsdorf, N.; Almdal, K.; Mortensen, K.; Messe, L.; Corvazier, L.; Fairclough, J. P. A.; Ryan, A. J.; Olmsted, P. D.; Hamley, I. W., Micro- vs. macro-phase separation in binary blends of poly(styrene)-poly(isoprene) and poly(isoprene)-poly(ethylene oxide) diblock copolymers. *Europhysics Letters* **2001**, *53*, 680-686.
38. Torikai, N.; Noda, I.; Karim, A.; Satija, S. K.; Han, C. C.; Matsushita, Y.; Kawakatsu, T., Neutron Reflection Studies on Segment Distribution of Block Chains in Lamellar Microphase-Separated Structures. *Macromolecules* **1997**, *30* (10), 2907-2914.
39. Park, S.-Y.; Sul, W.-H.; Chang, Y.-J., A Study on the Selectivity of Toluene/Ethanol Mixtures on the Micellar and Ordered Structures of Poly(styrene-*b*-4-vinylpyridine) Using Small-angle X-ray Scattering, Generalized Indirect Fourier Transform, and Transmission Electron Microscopy. *Macromolecules* **2007**, *40* (10), 3757-3764.

40. Kim, J.; Lee, J.; Lee, D., Self-assembled block copolymers: Bulk to thin film. *Macromol. Res.* **2008**, *16* (4), 267-292.
41. Roman, G.; Martin, M.; Joachim, P. S., Block copolymer micelle nanolithography. *Nanotechnology* **2003**, *14* (10), 1153.
42. Yun, S.-H.; Yoo, S. I.; Jung, J. C.; Zin, W.-C.; Sohn, B.-H., Highly Ordered Arrays of Nanoparticles in Large Areas from Diblock Copolymer Micelles in Hexagonal Self-Assembly. *Chemistry of Materials* **2006**, *18* (24), 5646-5648.
43. Tassin, J. F.; Siemens, R. L.; Tang, W. T.; Hadziioannou, G.; Swalen, J. D.; Smith, B. A., Kinetics of adsorption of block copolymers revealed by surface plasmons. *The Journal of Physical Chemistry* **1989**, *93* (5), 2106-2111.
44. Aizawa, M.; Buriak, J. M., Block Copolymer-Templated Chemistry on Si, Ge, InP, and GaAs Surfaces. *Journal of the American Chemical Society* **2005**, *127* (25), 8932-8933.
45. Chang, C.-Y.; Lee, Y.-C.; Wu, P.-J.; Liou, J.-Y.; Sun, Y.-S.; Ko, B.-T., Micellar Transitions in Solvent-Annealed Thin Films of an Amphiphilic Block Copolymer Controlled with Tunable Surface Fields. *Langmuir* **2011**, *27* (23), 14545-14553.
46. Brandrup, J.; Immergut, E. H.; Grulke, E. A., *Polymer handbook*. Wiley: New York, 1999.
47. Charles, M. H., Solubility Parameters - An Introduction. In *Hansen Solubility Parameters*, CRC Press: 2007; pp 1-26.
48. Manias, E.; Utracki, L., Thermodynamics of Polymer Blends. In *Polymer Blends Handbook*, Utracki, L. A.; Wilkie, C. A., Eds. Springer Netherlands: 2014; pp 171-289.



49. Utracki, L.; Mukhopadhyay, P.; Gupta, R. K., Polymer Blends: Introduction. In *Polymer Blends Handbook*, Utracki, L. A.; Wilkie, C. A., Eds. Springer Netherlands: 2014; pp 3-170.
50. Hansen, C. M.; Smith, A. L., Using Hansen solubility parameters to correlate solubility of C60 fullerene in organic solvents and in polymers. *Carbon* **2004**, *42* (8–9), 1591-1597.
51. Park, I.; Park, S.; Park, H.-W.; Chang, T.; Yang, H.; Ryu, C. Y., Unexpected Hexagonally Perforated Layer Morphology of PS-*b*-PMMA Block Copolymer in Supported Thin Film. *Macromolecules* **2006**, *39* (1), 315-318.
52. Yin, Y.; Sun, P.; Jiang, R.; Li, B.; Chen, T.; Jin, Q.; Ding, D.; Shi, A.-C., Simulated annealing study of asymmetric diblock copolymer thin films. *The Journal of Chemical Physics* **2006**, *124* (18), 184708.
53. Tsarkova, L.; Knoll, A.; Krausch, G.; Magerle, R., Substrate-Induced Phase Transitions in Thin Films of Cylinder-Forming Diblock Copolymer Melts. *Macromolecules* **2006**, *39* (10), 3608-3615.
54. Kugel, R. W., Raoult's Law: Binary Liquid-Vapor Phase Diagrams: A Simple Physical Chemistry Experiment. *Journal of Chemical Education* **1998**, *75* (9), 1125.
55. Cummins, C.; Borah, D.; Rasappa, S.; Chaudhari, A.; Ghoshal, T.; O'Driscoll, B. M. D.; Carolan, P.; Petkov, N.; Holmes, J. D.; Morris, M. A., Self-assembly of polystyrene-*block*-poly(4-vinylpyridine) block copolymer on molecularly functionalized silicon substrates: fabrication of inorganic nanostructured etchmask for lithographic use. *Journal of Materials Chemistry C* **2013**, *1* (47), 7941-7951.

56. Kim, T. H.; Huh, J.; Hwang, J.; Kim, H.-C.; Kim, S. H.; Sohn, B.-H.; Park, C., Ordered Arrays of PS-*b*-P4VP Micelles by Fusion and Fission Process upon Solvent Annealing. *Macromolecules* **2009**, *42* (17), 6688-6697.

57. Cummins, C.; Gangnaik, A.; Kelly, R. A.; Borah, D.; O'Connell, J.; Petkov, N.; Georgiev, Y. M.; Holmes, J. D.; Morris, M. A., Aligned silicon nanofins via the directed self-assembly of PS-*b*-P4VP block copolymer and metal oxide enhanced pattern transfer. *Nanoscale* **2015**, *7* (15), 6712-6721.

58. Cummins, C.; Kelly, R. A.; Gangnaik, A.; Georgiev, Y. M.; Petkov, N.; Holmes, J. D.; Morris, M. A., Solvent Vapor Annealing of Block Copolymers in Confined Topographies: Commensurability Considerations for Nanolithography. *Macromolecular Rapid Communications* **2015**, *36* (8), 762-767.

# 3

## Self-Assembly of High- $\chi$ PS-*b*-P4VP Block Copolymer for Formation of sub-7 nm Feature Size Structures by a Solvent Vapour Anneal Process.

---

### 3.1. Abstract

‘High  $\chi$ ’ block copolymers (BCPs), where  $\chi$  is the Flory-Huggins interaction parameter, have attracted a great deal of interest. This is because they can microphase separate at very small domain size when low molecular weight BCPs are used. Different molecular weight symmetric lamellae forming polystyrene-*block*-poly(4-vinylpyridine) (PS-*b*-P4VP) BCPs were used to produce nanostructured thin films by spin-coating from mixtures of toluene and THF. The as-cast thin films form micellar structures which transformed into regularly arranged lamellar patterns under solvent annealing in solvents of varied selectivity. The choice of solvent used for annealing allows for control of the self-assembled pattern morphology. Here, we have followed the formation of microdomain structures with time at different temperatures by atomic force microscopy (AFM). Ultra-small feature size (~10 nm pitch size) nanopatterns were fabricated by using low molecular weight PS-*b*-P4VP (PS and P4VP blocks of 3.3 and 3.1 kg mol<sup>-1</sup> respectively).

### 3.2. Introduction

To achieve extremely small feature size, high-resolution patterns below 16 nm on substrates of electronic materials is challenging. It is well understood that further improvements will be accompanied by increase in cost and throughput. It is expected that state-of-the-art 193 nm

immersion lithography will go beyond the 22 nm node but will struggle to achieve sub-12 nm structures.<sup>1</sup> Alternatives such as electron-beam (EBL) and extreme ultraviolet (EUV) lithographies can deliver the required feature size, but they still face significant technical problem of throughput and the cost, so it is difficult to predict their usefulness for next generation devices.<sup>2-5</sup> Block copolymers (BCPs) are composed of two incompatible blocks and due to their capabilities to self-assemble into periodic structures of nanometre-sized domain arrangements including spheres, cylinder, gyroid, perforated lamellae and alternating lamellae by microphase separation, are thought to be excellent candidate for next generation lithography.<sup>6-14</sup> The propensity of BCPs to self-assemble is determined by two factors:  $\chi N$ , (where  $\chi$  is the Flory-Huggins interaction parameter<sup>15</sup> and  $N$  is the number of monomers in the diblock copolymer (degree of polymerization)) and the volume fraction of each block ( $f$ ).  $\chi N$  is a measure of the segregation strength and in case of a symmetric diblock copolymer ( $f = 0.5$ ), it should be greater than 10.4 to self-assemble.<sup>16</sup> An order-disorder transition will occur when  $\chi N$  falls below 10.4 as dictated by low  $\chi$  parameters, low molecular weight of the BCP or by higher temperature. In the strong segregation limit ( $\chi N \gg 10$ ), the domain period of the microphase separated can be described as  $d \sim N^{2/3} \chi^{1/6}$ . The domain period of nanostructures can be decreased by reducing  $N$  whilst maintaining an appropriate  $\chi N$  over the critical value for phase-separation and by increasing the  $\chi$  parameter.<sup>16</sup> Over the years, a great deal of effort has been focused on decreasing the domain spacing of the BCPs, exerting control over the orientation on the phase separated domains and aligning structures to a preferred direction in the substrate plane. The symmetric diblock-copolymers self-assembles into a lamellar morphology, however, the pattern orientation can be challenging to control. It is generally thought that they preferentially orientate with the lamellae parallel to the substrate interface due to preferential wetting at both substrate and air interface of the block copolymer film.<sup>17</sup>

However, by balancing the wetting of the polymer blocks to the substrate, lamellae can be oriented perpendicular to the substrate.

The most studied lamellar BCP system, symmetric poly (styrene-*block*-methyl methacrylate) (PS-*b*-PMMA) with relatively weak interaction parameter ( $\chi = 0.04$ ) restricts the pitch size to 20 nm and, hence, use in next-generation lithographic applications is somewhat limited.<sup>18-20</sup> For this reason, different high  $\chi$  BCP systems have been studied to demonstrate sub-10 nm features. As can be seen above, by having high  $\chi$ , the BCP can phase separate into small domain structures with smaller inter-domain diffusion regions and produce patterns with less defects. At room temperature, the  $\chi$  parameter of PS-*b*-P4VP ( $\chi \sim 0.34$ )<sup>21</sup> is considerably higher than those of PS-*b*-PDMS ( $\chi \sim 0.26$ ),<sup>22</sup> PS-*b*-PMMA ( $\chi \sim 0.04$ ),<sup>23</sup> PS-*b*-P2VP ( $\chi \sim 0.18$ )<sup>24</sup> and PS-*b*-PEO ( $\chi \sim 0.08$ ).<sup>25</sup> PS-*b*-PDMS is very well studied - it is well reported that if one of the block contains inorganic moiety, it readily enhances the etching contrast between the blocks as well as increasing the  $\chi$  value.<sup>26-39</sup> It should also be noted that for many of these high  $\chi$  BCPs, thermal annealing cannot provide chain mobility due to the significantly lower interdiffusivity of BCP chains.<sup>40</sup> However, solvent vapour annealing can provide the chain mobility in polymer chains, significantly more important to control the orientation and microdomain nanostructure morphology.

In this chapter, we report the self-assembly of a high  $\chi$  block copolymer, poly (styrene-*block*-4-vinylpyridine) (PS-*b*-P4VP), to form sub-7 nm half-pitch patterns on a silicon substrate. The PS-*b*-P4VP used in this study is a class of non-ionic, amphiphilic block copolymers. The Flory-Huggins interaction parameter for PS-*b*-P4VP falls in the wide range of 0.4-7.5 as compared to 0.1 for PS-*b*-P2VP, reported by Clarke et.al.<sup>41</sup> thus the microphase separation of PS-*b*-P4VP of lower molecular weight systems is possible and so smaller domain spacing structures can be formed. It is also stressed that although the  $\chi$  parameter is high, the surface tension of PS is

only a little smaller than the surface tension of P4VP ( $\gamma_{PS} = 40.7 \text{ mNm}^{-1}$ ,  $\gamma_{PVP} = 45.1 \text{ mNm}^{-1}$ ) and although this can drive PS segregation to the free surface<sup>42</sup>, at normal temperatures, it is expected that wetting layers will not form the polymer/air interface and it should be possible to form perpendicularly oriented nanostructures without chemical modification of the substrate surface.<sup>43</sup>

### 3.3. Experimental

#### 3.3.1. Materials and methods

Diblock copolymers of poly(styrene-*b*-4-vinylpyridine) (PS-*b*-P4VP) of roughly symmetric block compositions were purchased from Polymer Source, Inc. (Montreal, Canada). The different molecular weight BCPs studied are summarized in Table 3.1. The polymers were used without further purification and modification. Reagent grade toluene, tetrahydrofuran (THF) and ethanol (dehydrated) were purchased from Sigma-Aldrich and used without further purification. The planar substrates used were polished, test grade 8" silicon <100> wafers (*p*-type, B-doped, thickness 650  $\mu\text{m}$ ) with a native oxide layer of  $\sim 2 \text{ nm}$ . The native oxide was not removed during the studies. The topographically patterned  $\text{Si}_3\text{N}_4$  substrates with pitches in the range of 50–500 nm, variable mesa widths of 30–1500 nm and depth of 60 nm were fabricated via 193 nm UV-lithography and processed by means of conventional mask and etch techniques.

**Table 3.1. List of PS-*b*-P4VP BCPs used**

Polymer	Total $M_n$ ( $\times 10^3$ g/mol)	$M_w/M_n$	P4VP fraction	BCP morphology (*)
PS <sub>21k</sub> - <i>b</i> -P4VP <sub>21k</sub>	42.0	1.15	0.5	L
PS <sub>9k</sub> - <i>b</i> -P4VP <sub>9.2k</sub>	18.2	1.09	0.51	L
PS <sub>7.4k</sub> - <i>b</i> -P4VP <sub>7.7k</sub>	15.1	1.08	0.51	L
PS <sub>5k</sub> - <i>b</i> -P4VP <sub>5k</sub>	10	1.1	0.5	L
PS <sub>3.3k</sub> - <i>b</i> -P4VP <sub>3.1k</sub>	6.4	1.2	0.48	L

\*L= Lamellae forming

### 3.3.2. Thin film preparation, solvent annealing and characterization

All PS-*b*-P4VP polymer samples were dissolved in a mixture of toluene and THF (80/20, v/v) to yield a 0.5 wt% polymer solution. The solution was kept stirring overnight to ensure the complete solubility of the polymer. The Si substrate was cleaned by sonicating in toluene and THF for 15 min, respectively and dried under a stream of nitrogen. A UV/Ozone treatment was used as a final cleaning procedure. The water contact angle was measured on untreated and UV/Ozone treated silicon. The UV/Ozone treatment makes the silicon surface more hydrophilic (37° for bare silicon and 0° for UV/Ozone cleaned). The thin film samples were prepared by spin-coating at 3000 rpm for 30 s on freshly cleaned silicon wafers using a Speciality Coating Systems G3P-8 spin-coater. To study the structural evolution of PS-*b*-P4VP diblock thin films, solvent annealing was performed in glass jars (100 mL) containing 10 mL of annealing solvent at 50 °C for 30 min to 6 h. The solvent used for annealing were varied according to the molecular weight of the polymer. After the desired annealing time, the samples were removed from the glass jars and allowed to evaporate the trapped solvent at ambient

conditions. All thin films did not exhibit any major swelling during annealing and were transparent. All samples were analysed using atomic force microscopy (AFM, Park Systems XE-100) and topographic images were collected in non-contact tapping mode under ambient conditions using silicon microcantilever probe tips with a force constant of  $42 \text{ Nm}^{-1}$  and resonance frequency  $\sim 285 \text{ KHz}$ . The scan rate was  $1.0 \text{ Hz}$  and scan line were  $256 \text{ pixels}$ . Topographic and phase images were recorded simultaneously. PS-*b*-P4VP BCP film thicknesses were measured with a spectroscopic ellipsometer (J.A. Woollam) at a fixed angle of incidence of  $70^\circ$ , on at least three different places on the sample and values were averaged as the film thickness.

### 3.4. Results and Discussion

To alleviate the difficulties associated with thermal annealing to form phase separated morphologies, we have instead used solvent vapour annealing. It has been well reported that the type of solvents used for annealing plays an important role in the morphology of block copolymers thin films.<sup>44-48</sup> In this chapter, we have limited our study to only two solvents, viz. THF and toluene. Toluene and THF both are PS selective solvent, since  $\chi_{\text{PS-solvent}} < 0.5$  and  $\chi_{\text{P4VP-solvent}} > 0.5$ . It must be noted that for a polymer to be soluble in a solvent at any temperature,  $\chi$  must be below  $0.5$ .<sup>49</sup> Table 3.2 shows that toluene is a more selective solvent for PS than THF.



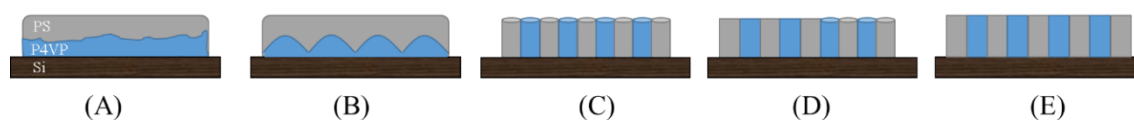
**Table 3.2. The Selectivity of the solvents and interaction parameter ( $\chi$ )**

Solvent	Molar Volume cm <sup>3</sup> mol <sup>-1</sup>	$\delta_{\text{Solvent}}$ MPa <sup>1/2</sup> (a)	$\chi_{\text{PS}}$ (b)				$\chi_{\text{P4VP}}$ (b)			
			25°C	40°C	50°C	60°C	25°C	40°C	50°C	60°C
Toluene	106.9	18.2	0.3469	0.3465	0.3463	0.3461	1.03	0.9972	0.9769	0.9578
THF	81.7	19.4	0.3611	0.36	0.3594	0.3588	0.5985	0.5861	0.5785	0.5713

(a) Solubility parameters value taken from *Physical Properties of Polymers Handbook*.<sup>50</sup> (b)

The selectivity values of the solvents were estimated with  $\chi = \chi_{\text{H}} + \chi_{\text{S}} = \{V_{\text{s}} (\delta_{\text{s}} - \delta_{\text{p}})^2 / RT\} + 0.34$ ;  $V_{\text{s}}$  denotes the molar volume and  $\delta$  is the solubility parameter for solvent (s) and polymer (p). The solubility parameters for PS and P4VP are, 18.6 and 22.2 MPa<sup>1/2</sup> respectively.

According to the volume fraction of each component in all the PS-*b*-P4VP samples, these BCPs should form the lamellar structure. However, in some cases, the system can form P4VP cylinders in the PS matrix because of a volume fraction change caused by the higher degree of swelling of the PS matrix than the P4VP. The swelling of the polymer block is dependent on the solvent selectivity, which is described in detail later in this chapter. Different morphologies can arise, as shown in Scheme 3.1, by changing various parameter such as solvent(s), temperature, time of annealing etc. We have investigated the microphase separation in all block copolymer system under toluene, THF and toluene/THF (50/50 v:v) mixtures. The large molecular weights PS-*b*-P4VP (PS<sub>21k</sub>-*b*-P4VP<sub>21k</sub> and PS<sub>9k</sub>-*b*-P4VP<sub>9.2k</sub>) were annealed in PS selective THF atmospheres, while PS<sub>7.4k</sub>-*b*-P4VP<sub>7.7k</sub> thin films were annealed in mixture of toluene and THF (50/50, v:v) and small molecular weight BCPs (PS<sub>5k</sub>-*b*-P4VP<sub>5k</sub> and PS<sub>3.3k</sub>-*b*-P4VP<sub>3.1k</sub>) were annealed in toluene.



Scheme 3.1 Schematic of time development of the microdomain formation on thin symmetric PS-*b*-P4VP film. The gray and blue region represents PS and P4VP blocks. (A) is as-cast thin film, (B) is thin film after exposed to solvent vapours, (C-E) plausible microstructures after solvent annealing.

### 3.4.1. Self-assembly of PS-*b*-P4VP by annealing in THF environment

High molecular weights PS-*b*-P4VP (PS<sub>21k</sub>-*b*-P4VP<sub>21k</sub> and PS<sub>9k</sub>-*b*-P4VP<sub>9.2k</sub>) were dissolved in a mixture of toluene and THF (80/20, v:v). The 80/20 ratio was carefully chosen since THF has a preferential affinity for PS compared to P4VP, as shown in Table 3.2. Solvent annealing has a unique advantage over thermal annealing. The BCP domain morphology can be controlled through choice of solvent, as explained earlier in Chapter 2. Annealing in toluene (a weakly selective solvent for the PS) causes the block copolymer film to phase separate in hexagonal array of dots, while annealing in THF environment leads to microphase separation resulting in lamellar structures across the whole substrate surface as shown in Fig. 3.1. The morphological changes of the PS<sub>21k</sub>-*b*-P4VP<sub>21k</sub> system under a THF environment (b.p. 66 °C) at various annealing temperatures (from 40 °C to 60 °C) and times (30 min to 7 h) were studied. As evident from the AFM images in Fig. 3.1, the microphase separation occurs at all temperatures studied for 30 min to 7 h. As-cast PS<sub>21k</sub>-*b*-P4VP<sub>21k</sub> thin films prepared in the normal way form micellar structures as explained earlier in Chapter 2. As discussed by O'Driscoll et.al,<sup>51</sup> the choice of solvent is dictated by the solvent parameter.

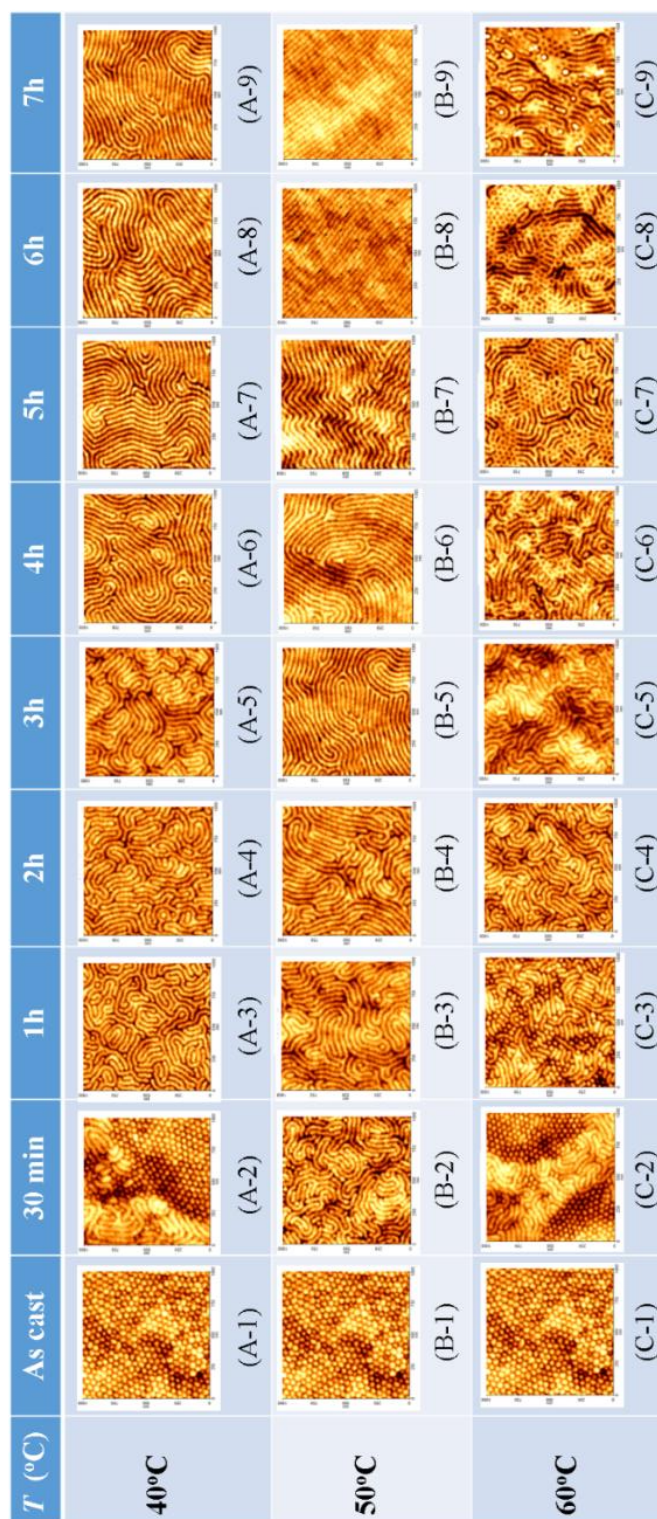


**Figure 3.1.** AFM topographic images of solvent annealed PS<sub>21k</sub>-*b*-P4VP<sub>21k</sub> thin films exhibiting lamellar structures after annealing at 40 °C (A-2 to A-9), 50 °C (B-2 to B-9) and 60 °C (C-2 to C-9) for 30 min to 7 h under THF atmosphere, respectively. The thickness of as-cast and solvent annealed film has a thickness of 33 nm and 35 nm ± 2 nm, respectively.

After exposure to saturated THF vapour at 40 °C for 30 min, the film appear to be phase separated but a mixed morphology containing micelles and fingerprint patterns appears with a lamellar pitch size of 35 nm as observed by AFM. Shorter annealing times result in well-defined microphase separation. On increasing the annealing time to 1 h, all the micellar structures are lost and a regular striped pattern is seen. Prolonged exposure to THF vapour from 2 to 7 h (A-3 to A-9) increases the correlation length of the lamellae. No dewetting or phase transition were observed during the annealing. The film thickness was measured by ellipsometry and found to be around 35 nm for as-cast thin film, while solvent annealed film saw an increase of 2 nm. In all the solvent annealed thin films the equilibrium state phase structures were observed. It is obvious here that there is a clear correlation between defect density/correlation length in lamellar BCP thin films and anneal time due to defect annihilation processes that allow high energy defects (disclinations/dislocations) to be removed while reducing the block-block interfacial area and so lowering the total energy of the system.<sup>52</sup>

As shown in Fig. 3.1, films annealed in THF vapour at 50 °C follows the same trends with small correlation length fingerprint lamellar patterns for 30 min to 4 h (B-2 to B-6) but with increasing annealing time from 5 to 7 h (B-7 to B-9), well-ordered lamellar structures with increased correlation length are formed. The film thickness of the as-cast film and the annealed film were 35 nm and 38 nm, respectively. In further sets of experiments, the samples were annealed at an elevated temperature of 60 °C and data are shown in Fig. 3.1 (C-1 to C-9). The thin films annealed for small duration form fingerprint patterns (C-2 to C-5), but after the increase in annealing time (C-6 to C-9), a mixed morphology is observed. Further increases in annealing time produces no regular structures. With an increase in annealing temperature (60 °C), a higher degree of swelling is observed and an annealed film thickness of 42 nm was observed (as-cast film thickness is  $36 \pm 1$  nm). During annealing in THF vapour, the colour of the cast film changed from grey to yellow during annealing. When the film was removed from

the jar, the film colour quickly returned to grey as the THF vapour in the film evaporated. This indicates the swelling of film and increase in film thickness with THF.

**Table 3.3. Vapour Pressures of the Annealing Solvents at Different Temperatures**

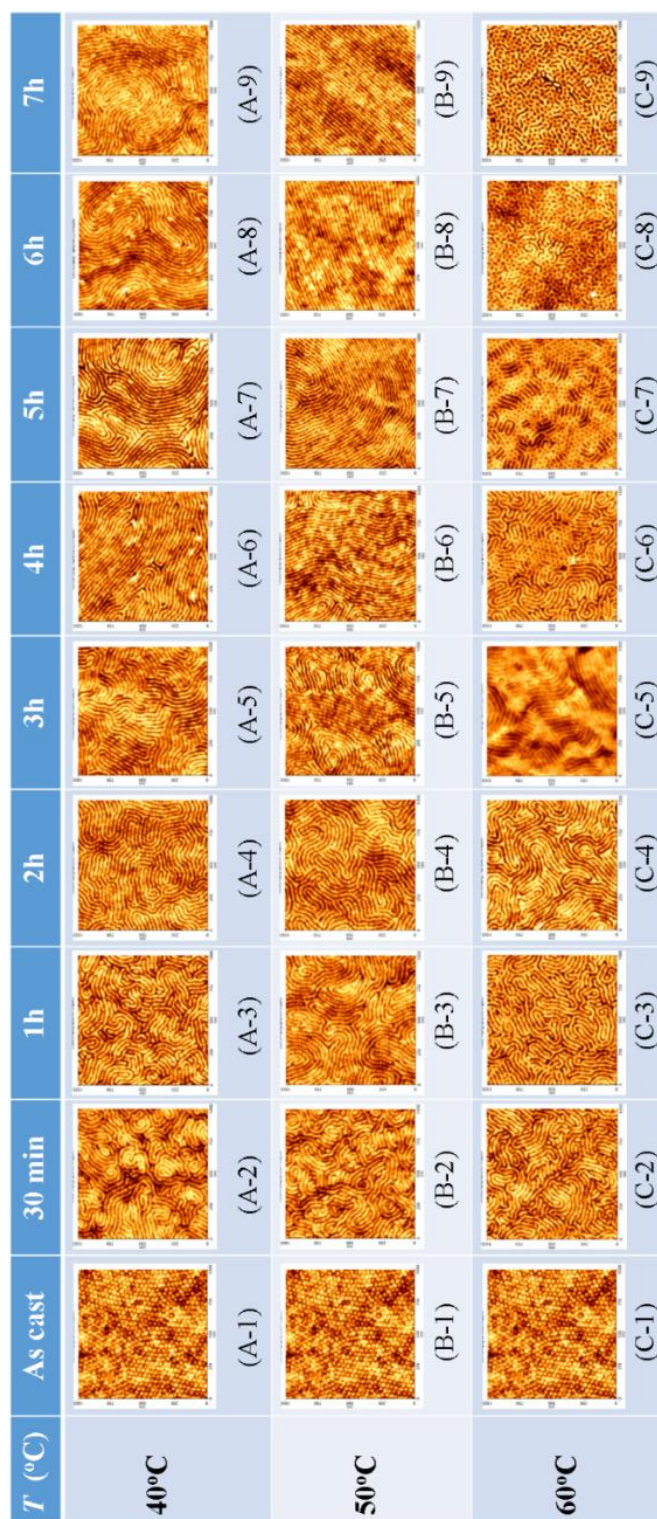
Toluene		THF	
<i>T</i> (°C)	Vapour pressure (mmHg)	<i>T</i> (°C)	Vapour pressure (mmHg)
25	30	25	160
40	59	40	320
50	92	50	420
60	140	60	660

Table 3.3 lists the vapour pressure of the annealing solvents at different temperatures. At 60 °C, the vapour pressure of THF is increased by more than 60% compared to that at 50 °C and it is clear that the film swells to a much greater extent especially on prolonged annealing times. When the annealing time is increase to 4 h or more (C-6 to C-9), the mixed morphology becomes predominant, while increase in annealing time by more than 7 h, no phase separation in thin film is observed. The data suggest the extended swelling results in considerable trapped free volume and also moves the film into the disordered region.

In previous reports, PS-*b*-P4VP thin films were solvent annealed to improve lateral ordering<sup>49,53,54</sup> and change the orientation<sup>55</sup> of the nanodomains. Here, we report that the micellar morphologies can be changed to lamellar nanodomains, in thin films by solvent annealing. As explained earlier, similar solvent annealing conditions were employed for another BCP system, PS<sub>9k</sub>-*b*-P4VP<sub>9.2k</sub>, as shown in Fig. 3.2. The spherical micellar structures (Fig. 3.2, A-1, B-1, C-1) were present for as-cast thin films of thickness 28 nm. The solvent annealing was performed in PS selective (but relatively poor for P4VP) THF vapours. In Chapter 2, for PS<sub>9k</sub>-*b*-P4VP<sub>9.2k</sub>, the solvent annealing conditions were studied by varying solvent selectivity (in toluene rich,

THF rich and various compositions of toluene/THF mixtures). THF was considered as most suitable solvent for annealing to produce well-ordered structures.

At 40 °C, as the annealing time under THF vapours was increased from 30 min to 7 h (Fig. 3.2, A-2 to A-9), microphase separation was observed all over the substrate with no sign of dewetting. The film thickness varied by 1-2 nm, and after 7 h the thickness of the film was 29 nm  $\pm$  1 nm, with the centre-to-centre distance between two adjacent lamellae being 26 nm. On annealing at 50 °C, BCP thin films behave in the same manner (Fig. 3.2, B-2 to B-9) but the correlation length seems to be increased and a well-ordered structure can be seen after 5 h. The domain spacing was unchanged from that recorded at 40 °C (26 nm). The film thickness of PS<sub>9k</sub>-*b*-P4VP<sub>9.2k</sub> after 7 h solvent annealing in THF is measured as 30 nm  $\pm$  1 nm, which is higher than the measured value for 40 °C annealed film. The higher degree of swelling is due to the higher vapour pressure of THF at 50 °C and the increased film thickness is due to residual free volume.



**Figure 3.2.** AFM topographic images of solvent annealed PS<sub>9k</sub>-*b*-P4VP<sub>9.2k</sub> thin films exhibiting lamellar structures after annealing at 40 °C (A-2 to A-9), 50 °C (B-2 to B-9) and 60 °C (C-2 to C-9) for 30 min to 7 h under THF atmosphere, respectively. The thickness of as-cast and solvent annealed film has a thickness of 28 nm and 29 nm ± 2 nm, respectively.

Further increases in annealing temperature leads to higher degree of swelling and at 60 °C the film thickness of 7 h annealed film was further increased to  $32 \pm 1$  nm. A regular trend of spherical micelles transforming into fingerprint structures were observed for as cast and annealed film of 2 h, as shown in Fig. 3.2 (C-1 and C-2 to C-4). Increasing the anneal time from 3 h to 7 h (Fig. 3.2, C-5 to C-9) shows degradation of patterns associated with further increase in swelling of the film. It is important to note that the vapour pressure of the solvent controls the thickness of the swollen film as well as the relative concentration of the polymer and solvent in thin film. After 4 h (C-6) a mixed morphology is observed, while after 5 h (C-7) hexagonally packed (with few stripes) cylindrical P4VP microdomains oriented normal to the surface in the PS matrix are observed. Since THF selectively swells P4VP, the volume fraction of PS is expected to decrease and it is suggested that the increase in annealing time results in composition changes and the morphology shifted from lamellae to cylinders. After 6 h and 7 h of annealing, we suggest the patterns consist of cylindrical microdomains oriented both normal and parallel to the surface as shown in Fig. 3.2 (C-8 and C-9). The change in orientation with film thickness and choice of solvent might be due to the result of changes in commensurability between film thickness and pitch size of the microdomains.

### **3.4.2. Self-assembly of PS-*b*-P4VP by annealing in a mixed solvent environment.**

The solvent annealing technique was also studied for another low molecular weight system, PS<sub>7.4k</sub>-*b*-P4VP<sub>7.7k</sub>. As shown in Fig. 3.3, thin films prepared by spin-coating in the usual way produce 23 nm thin film and resulted in similar morphology trends. As explained in earlier section for the high molecular weight PS-*b*-P4VP system, a well-ordered structure results when annealed in THF, whereas toluene annealed thin films produce micellar structures.

As for the other samples annealing in both toluene and THF vapour swell both PS and P4VP domains in thin film by few nm. But due to high degree of swelling by THF, dewetting was



observed after 2 h. When the thin films are annealed in toluene, no clear phase separation was observed and after 2 h the film was featureless. After 2 h of annealing in THF (A-2 to A-4) and toluene (B-2 to B-4), the film swells by 6 and 2 nm, respectively. When the mixture of toluene/THF (50/50, v:v) was used as annealing solvent relatively well-ordered but vertically orientated line features were observed in Fig. 3.3 (C-2 to C-8) with a domain spacing of 19 nm. The film thickness after 2 h (C-4) was measured at 26 nm due to the swelling by both the solvents. With increased annealing time, well-ordered structures were observed (C-5 to C-8).

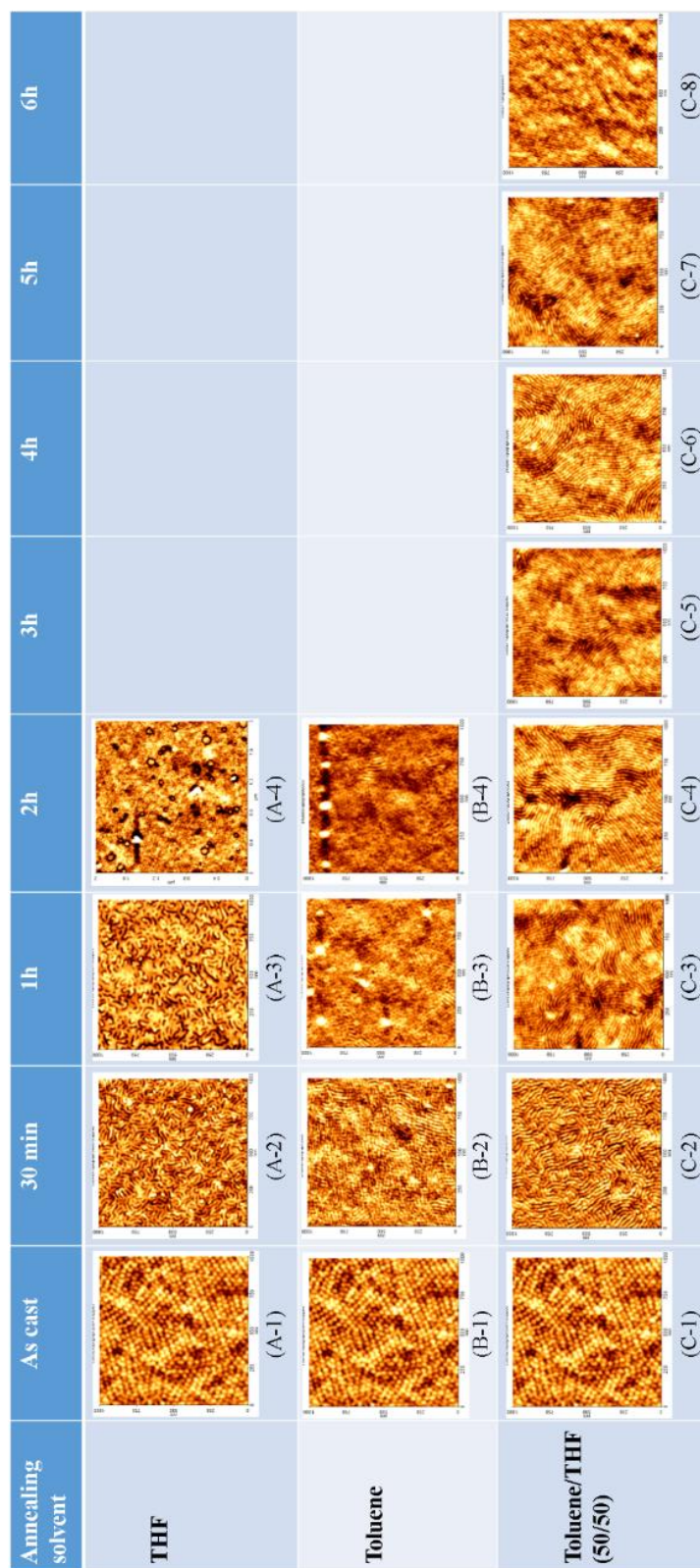


**Figure 3.3.** AFM topographic images of solvent annealed PS<sub>7.4k</sub>-*b*-P4VP<sub>7.7k</sub> thin films after annealing at 50 °C for 30 min to 6 h under THF (A-2 to A-4), toluene (B-2 to B-4) and a mixture of toluene/THF (50/50, v:v) (C-2 to C-8) atmosphere, respectively.

### 3.4.3. Fabrication of sub-7 nm features by solvent annealing.

Thin films of PS<sub>5k</sub>-*b*-P4VP<sub>5k</sub> and PS<sub>3.3k</sub>-*b*-P4VP<sub>3.1k</sub> were used to fabricate sub-7 nm features by solvent annealing in toluene vapours at different temperatures 40 °C, 50 °C and 60 °C for different time intervals, as shown in Fig. 3.4 and Fig. 3.5, respectively. Film thicknesses were measured for the PS<sub>5k</sub>-*b*-P4VP<sub>5k</sub> and PS<sub>3.3k</sub>-*b*-P4VP<sub>3.1k</sub> system after spin-coating and recorded as 18 nm and 14 nm, respectively. It should be noted that although solution concentrations remain constant in this work, reduced film thickness with decreased molecular weight is seen because of decreased viscosity of the casting solution. No features or micellization was observed. This is probably due to increased solubility at low molecular weight. The thin films were solvent annealed in toluene. At 40 °C, disordered structures can be seen as shown in Fig. 3.4 after 1 h (A-1). Interestingly, a similar trend in the behaviour of the BCPs in terms of long range ordering was observed on increasing the annealing time for both smaller and higher molecular weight PS-*b*-P4VP BCP systems. The morphological transition from smaller stripes (i.e. low persistence lengths) to long, ordered lamellae structures with either increased anneal times or by increasing solvent vapour pressure was observed as shown in Fig. 3.4 (A-2 to A-6). Lamellae of 15 nm ± 1 nm were seen to form and the thickness of as-cast and annealed film remained unchanged. It is clear that during annealing at 40 °C, the toluene vapour allows the evolution of the phase separated morphology. By increasing the annealing temperature, higher vapour pressure leads to well-defined film arrangements at 50 °C, with increase of ~ 2 nm film thickness. Well-ordered structures after annealing for longer periods are shown in Fig. 3.4 (B1-B6). Further increasing the temperature to 60 °C, as shown in Fig. 3.4 (C-1 to C-6), increases the film thickness by approximately 3-4 nm and film roughness can be seen with regions of the image showing both mixed morphology and single morphology but at different thicknesses. Lamellae are seen in both the lighter and darker regions of the AFM images. This suggests

“over-swelling” of the films leading to thickness variation. On annealing for 30 min, no well-defined arrangements are observed.

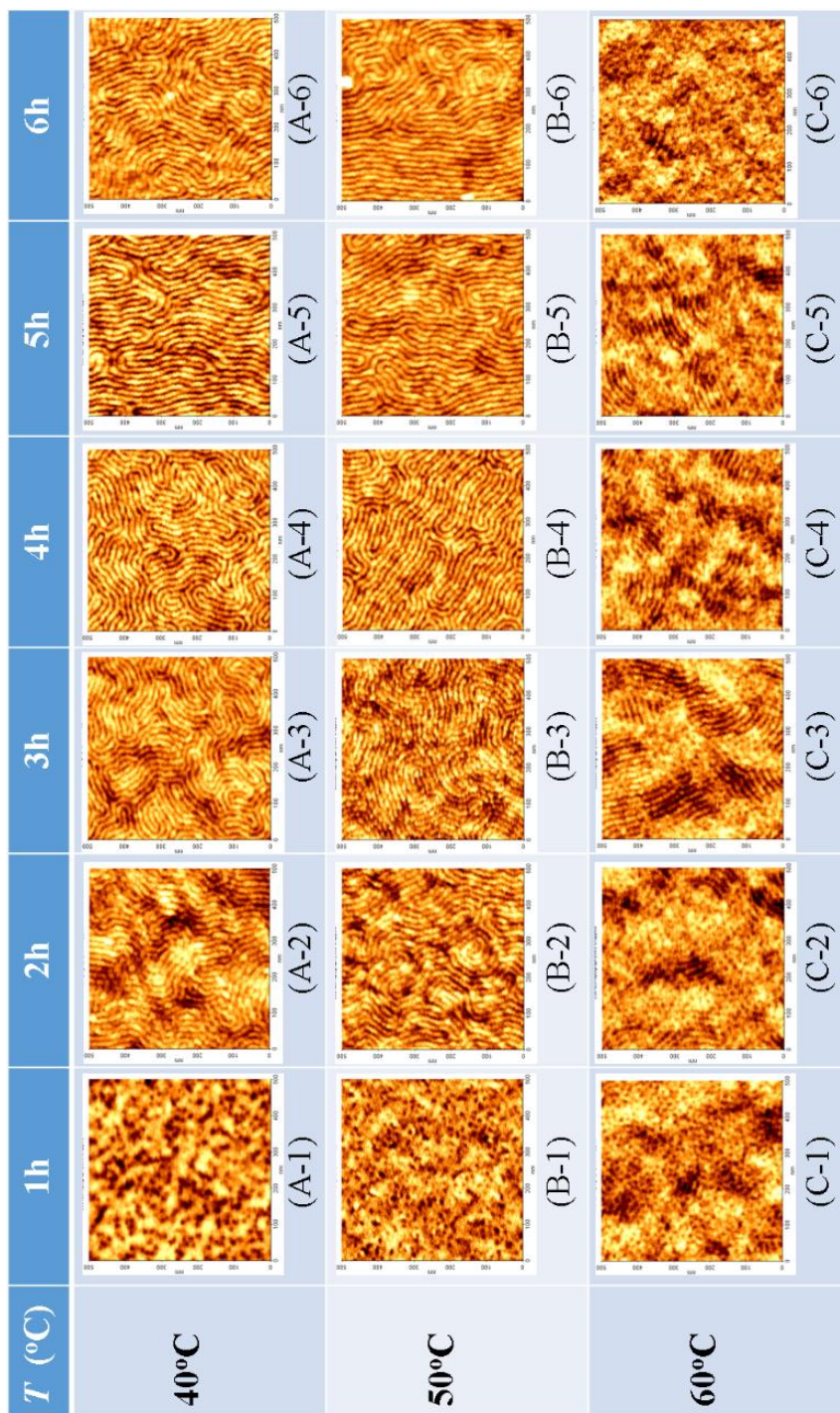


**Figure 3.4.** AFM topographic images of solvent annealed PS<sub>5k</sub>- $b$ -P4VP<sub>5k</sub> thin films exhibiting lamellar structures after annealing at 40  $^{\circ}\text{C}$  (A-1 to A-6), 50  $^{\circ}\text{C}$  (B-1 to B-6) and 60  $^{\circ}\text{C}$  (C-1 to C-6) for 1 h to 6 h under a toluene atmosphere, respectively.

We extended this methodology to a molecular weight PS<sub>3.3k</sub>-*b*-P4VP<sub>3.1k</sub> system. Annealing at 40 °C produces the similar structure as for PS<sub>5k</sub>-*b*-P4VP<sub>5k</sub> as shown in Fig. 3.5. Increasing the anneal temperature leads to well-ordered lamellae with a pitch (domain spacing) size of 10.5 nm ± 0.5 nm. The P4VP feature size was 5.5 nm ± 0.5 nm as shown in Fig. 3.5 (B-2-to B-6). The thin film thickness of the as-cast film and annealed film at 40 °C remained unchanged and was measured as 14 nm ± 1 nm. At anneal temperatures of 50 °C (Fig. 3.5, B-1 to B-7), a 15 nm ± 1 nm thin film was produced after annealing for 7 h. The degree of swelling was as observed for the PS<sub>5k</sub>-*b*-P4VP<sub>5k</sub> system. Annealing at 60 °C produces no structure for 4 h annealing and significant dewetting of the films was observed after the same annealing time (Fig. 3.5, C-1 to C-4).

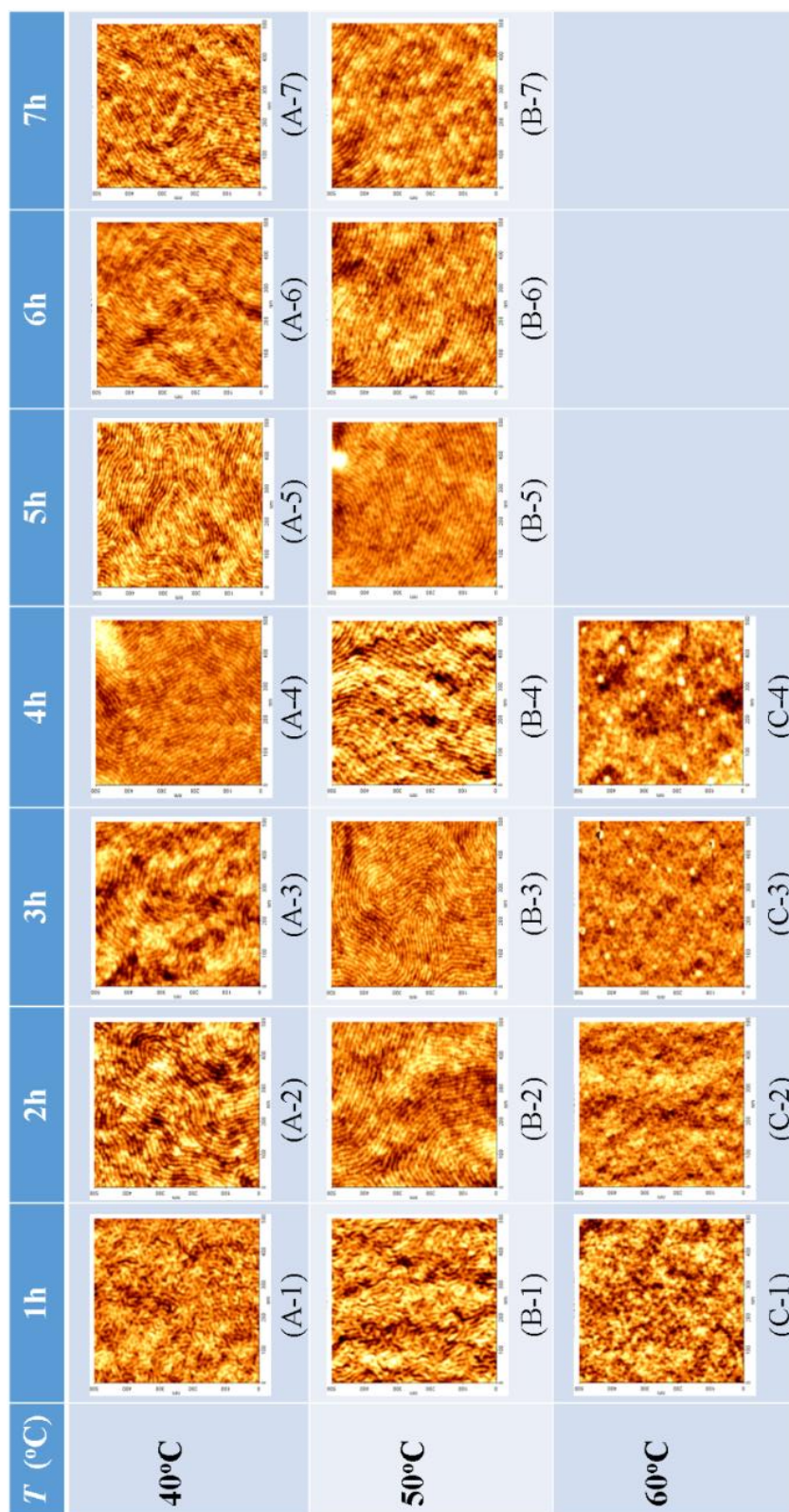


**Figure 3.5.** AFM topographic images of solvent annealed PS<sub>3.3k</sub>-*b*-P4VP<sub>3.1k</sub> thin films exhibiting lamellar structures after annealing at 40 °C (A-1 to A-7), 50 °C (B-1 to B-7) for 1 h to 6 h and 60 °C (C-1 to C-4) for 1 h to 4 h under toluene atmosphere, respectively.

#### 3.4.4. Effect of film thickness on the morphology of BCP thin films

Here we have studied the effect of film thickness on the morphology of solvent annealed thin film at 50 °C under toluene/THF environment for 6 h. Film thickness can have profound effects on e.g. domain orientation and, further, there is a possibility of residual solvent being trapped in thin film which will also be dependent on film thickness. Thin films of different thickness were prepared to form 55 nm to 17 nm thin films, as shown in Fig. 3.6, by spin coating at 1000 to 5000 rpm for 30 s. Note that the film thickness can be controlled by either the spin speed, the volatility of the solvent or the concentration of the block copolymer solution.<sup>57</sup> However, we wanted to use constant coating solutions and so different spin-speed was used. The surface roughness of thin films can be influenced by spin-speed but this was only a minor effect here.

As shown in Fig. 3.6 (A-1), a film with thickness of 55 nm was prepared by spin coating the 0.5 wt % polymer solution at 1000 rpm. After solvent annealing in a mixture of toluene and THF (50/50, v:v) hexagonally ordered dot structures are formed with centre-to-centre distance between two adjacent dots of 23 nm. This is contrary to the expected lamellar structure. It is suggested that, the formation of hexagonally ordered dots are due to a volume of toluene trapped in the films after-coating. With increasing spin speed thinner films are produced and the volume of trapped toluene vapours decreases (since evaporation is more efficient) and this leads to formation of lamellar structures after annealing, as shown in Fig. 3.6 (A-2 to A-7). When the thin films were prepared at spin speed at 3000 rpm (A-5) and 4000 rpm (A-6), a well ordered lamella structure with a pitch size of 22 nm were formed and the film thickness calculated was measured at 25 nm and 21 nm. Note that a high variation in film contrast was observed when the film was prepared at 4000 rpm also suggest this is because of a high degree of swelling in the film and high roughness. At 5000 rpm, as shown in Fig. 3.6 (A-7), a very thin film of 17 nm thickness was formed with good indication of lamellar structure after solvent

annealing; however, the film is also rougher than might be expected due to the high degree of swelling.

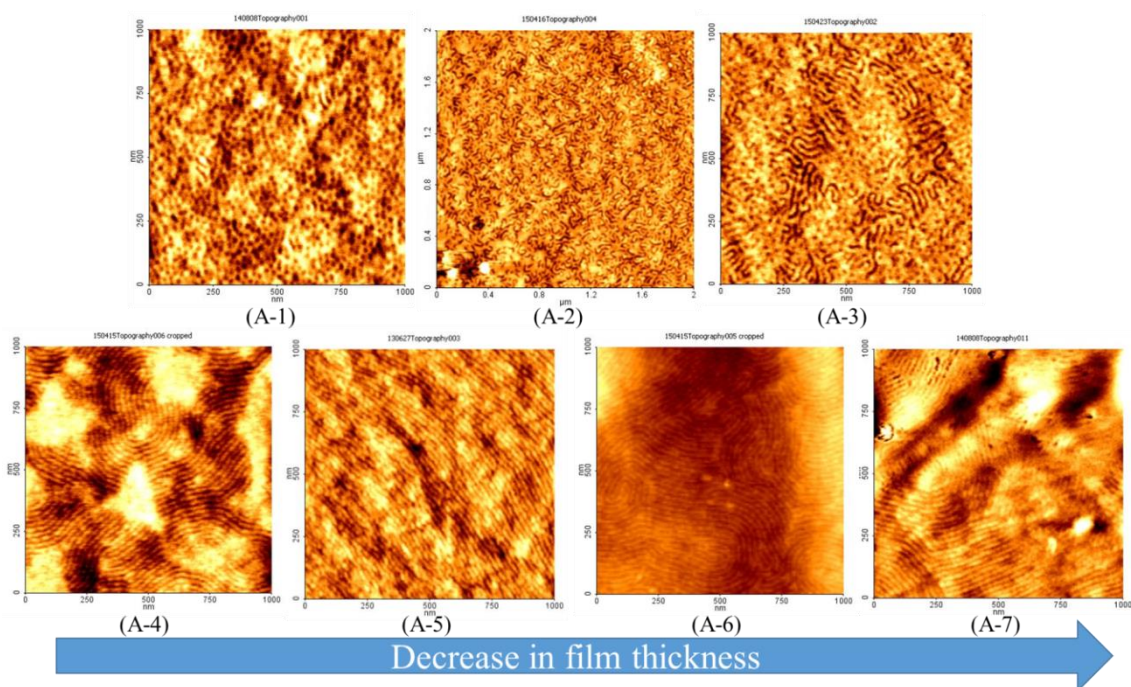


**Figure 3.6.** AFM topographic images of solvent annealed PS<sub>7.4k</sub>-*b*-P4VP<sub>7.7k</sub> thin films after annealing at 50 °C for 6 h under toluene/THF (50/50, v:v), spin coated at: (A-1) 1000 rpm, (A-2) 1500 rpm, (A-3) 1800 rpm, (A-4) 2400 rpm, (A-5) 3000 rpm, (A-6) 4000 rpm and (A-7) 5000 rpm.

An alternative explanation for these data might be given. It is well reported that for a symmetric BCP system, if the film thickness  $t$  is thicker than its equilibrium period  $L_0$  and  $t \neq (n + 1/2)L_0$  ( $n$  is an integer), island or holes of height  $L_0$  form at the free surface. However, the frustrated morphology is formed when the film thickness is below  $L_0$ , by the competition of several forces, including slow kinetics, strong surface interactions and the bulk driving force toward a morphology with the natural period  $L_0$ .<sup>44</sup> One might argue that a similar behaviour was observed here as shown in Fig. 3.6. It could be argued that only the higher speeds have thickness consistent with integer values of the  $L_0$  Value.



### 3.4.5. Graphoepitaxy

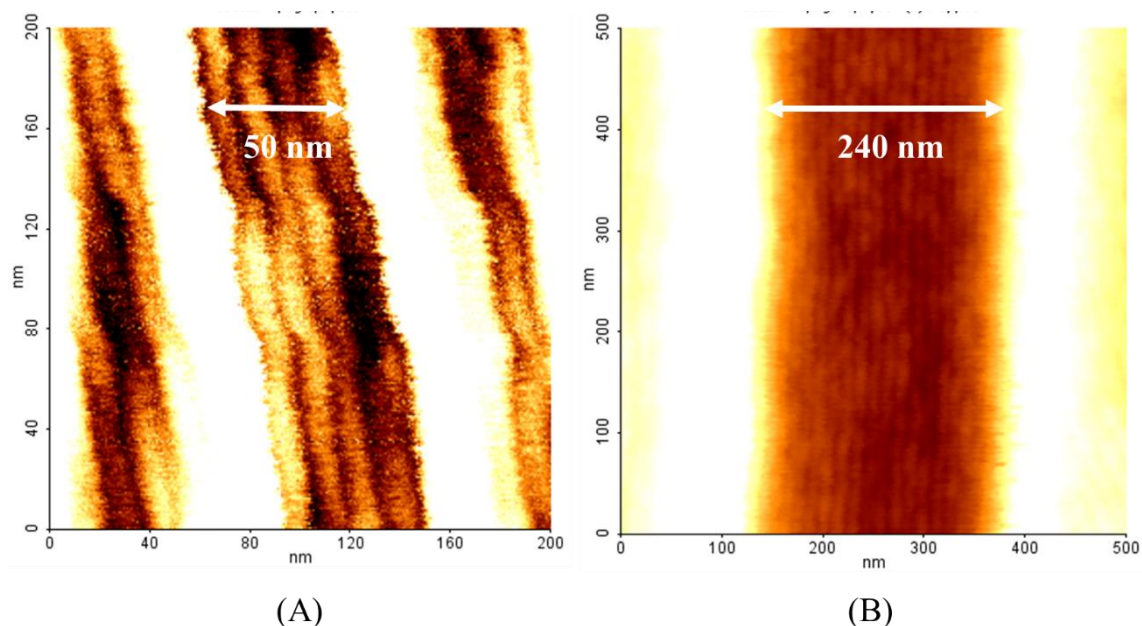


**Figure 3.7.** AFM topographic images of PS<sub>3.3k</sub>-*b*-P4VP<sub>3.1k</sub> thin films formed on patterned Si<sub>3</sub>N<sub>4</sub> substrates. Data shown are with Si<sub>3</sub>N<sub>4</sub> mesa and channel widths of (A) 30 nm and 50 nm, (B) 150 nm and 240 nm.

The true potential of BCP self-assembled patterns can be realized only if long-range periodic and translational alignment can be achieved.<sup>58</sup> Here, we have demonstrated a graphoepitaxial approach for the PS<sub>3.3k</sub>-*b*-P4VP<sub>3.1k</sub> films using topographic features and solvent annealing. A similar annealing method as detailed above was used to generate patterns in the trenched substrates. The substrate were cleaned thoroughly by sonicating and washing with toluene followed by UV/Ozone treatment. The same solution and spin speed that formed 14 nm ± 1 nm thick films on flat substrates were used here. We observe registration of perpendicularly oriented P4VP lamellae upon annealing in toluene vapours at 50 °C, as shown in Fig. 3.7. Two different width trenches of small 50 nm and large 240 nm were studied to demonstrate the alignment of lamellae. We have achieved defect-free domain alignment of perpendicular lamellae with 10.5 nm ± 1 nm pitch across trenches.

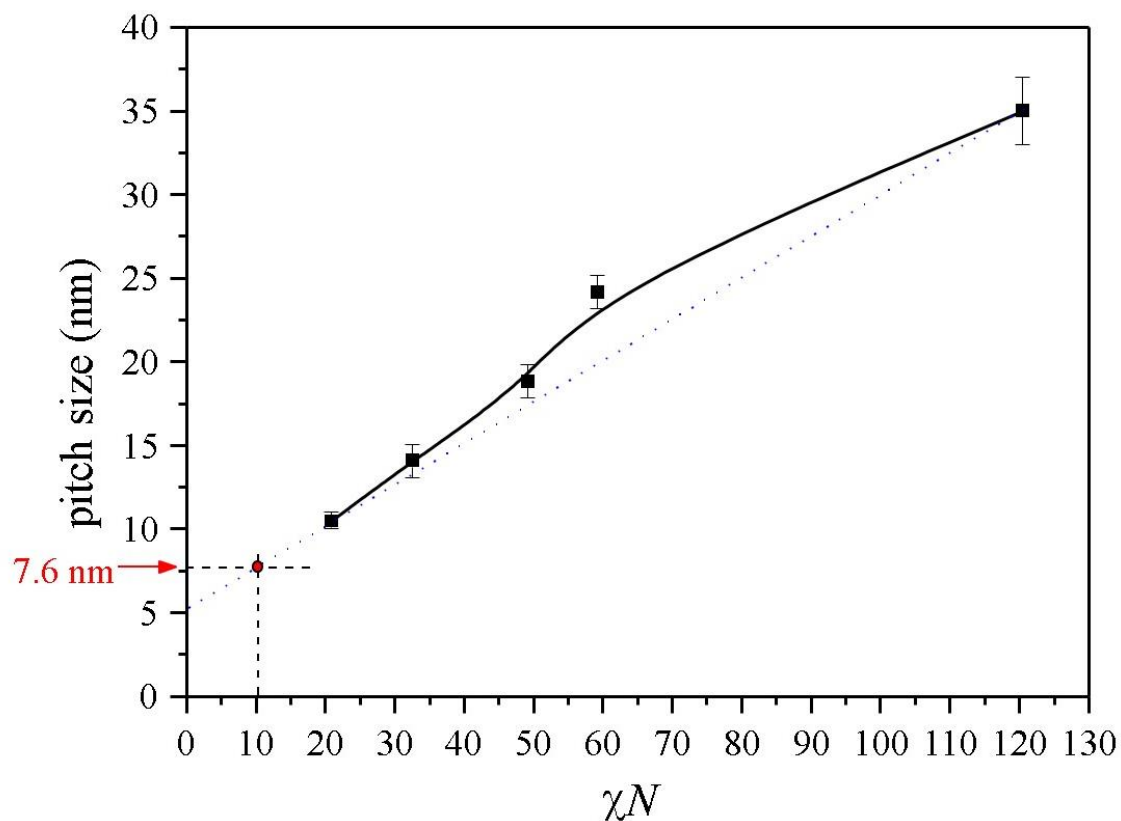


**Figure 3.8.** Pitch size versus the  $\chi N$  values of all PS- $b$ -P4VP used in this study. 7.6 nm is an estimated value calculated by drawing an arbitrary line.

### 3.5. Conclusions

As shown here, ultra-small sub-7 nm features can be generated using this high  $\chi$  PS<sub>3.3k</sub>- $b$ -P4VP<sub>3.1k</sub> BCP system. But a significant question is how small can we go using this approach for this polymer system? This question can be answered by taking into account the Flory-Huggins parameter ( $\chi$ ) and changing the degree of polymerization ( $N$ ) and as shown in Fig. 3.8, where we plot a graph of  $\chi N$  versus the final pitch size of lamellae observed in all the BCPs studied. All the BCPs studied are in either the intermediate segregation regime (ISR,  $12.5 < \chi N < 100$ ) or the strong segregation limit (SSL,  $\chi N > 100$ ). As shown in Fig. 3.8, the *dotted line* can be used to predict the minimum pitch size possible for the lamellar forming PS- $b$ -P4VP BCP system. Since  $\chi N$  should be more than 10.5 to form a lamellar microdomain

structure<sup>7</sup> it is clear that a pitch size of 7.8 nm is possible for this BCP. It should also be pointed out that further scaling can be achieved and recently, Ghoshal et.al<sup>52</sup> have demonstrated a lithium chloride (LiCl) salt addition method to amplify the effective interaction parameter ( $\chi_{\text{eff}}$ ) of the polystyrene-*block*-polyethylene oxide (PS-*b*-PEO) BCP system to fabricate a vertical lamellae arrangement of sub-16 nm pitch size.

We have demonstrated the fabrication of highly ordered arrays with sub-7-nm features on both planar and topographically patterned substrates that allow the directed self-assembly of low-molecular weight PS-*b*-P4VP. The microdomain morphology from the self-assembly of lamellar forming, different molecular weights, high  $\chi$  PS-*b*-P4VP block copolymers was systematically studied following spin-coating and a solvent annealing in toluene and THF. Because of the high interaction parameter ( $\chi$ ) this system gives well-ordered structures at smaller molecular weight BCPs. This BCP system is shown to be very relevant for lithographic applications, since the microdomain orientation could be controlled by choice of solvent, film thickness etc., and microphase separation was obtained by simple solvent annealing technique. As-cast films, when solvent annealed for even short periods had enough mobility to change the morphology from P4VP micelles to the equilibrium morphology of P4VP lamellae. It was also observed that the orientation and resistance length of lamellae is not uniform and increases in annealing time were needed to allow the mobility of chain to increase so as to form well-ordered structures. The phase behaviours of PS-*b*-P4VP are strongly dependent on the use of solvents and variations in the phase diagram of the PS-*b*-P4VP could be observed. This is due to the high difference in solubility parameter between PS and P4VP ( $\delta_{\text{PS}} - \delta_{\text{P4VP}} = 3.6 \text{ MPa}^{1/2}$ ). The thin films solvent annealed at lower temperatures (40 °C) exhibits a mixed pattern of parallel stripes and perpendicular cylinder to the substrate, while increase in temperature (50 °C) produces well-ordered lamellae. The results obtained in this chapter suggest that the PS-*b*-P4VP is an excellent candidate for next-generation lithography.

### 3.6 References

1. Mack, C. A. The Future of Semiconductor Lithography: After Optical, What Next? 2007.
2. Schiff, H., Nanoimprint lithography: An old story in modern times? A review. *Journal of Vacuum Science & Technology B* **2008**, 26 (2), 458-480.
3. Wu, B.; Kumar, A., Extreme ultraviolet lithography: A review. *Journal of Vacuum Science & Technology B* **2007**, 25 (6), 1743-1761.
4. Gangnaik, A.; Georgiev, Y. M.; McCarthy, B.; Petkov, N.; Djara, V.; Holmes, J. D., Characterisation of a novel electron beam lithography resist, SML and its comparison to PMMA and ZEP resists. *Microelectronic Engineering* **2014**, 123, 126-130.
5. Ma, S.; Con, C.; Yavuz, M.; Cui, B., Polystyrene negative resist for high-resolution electron beam lithography. *Nanoscale Research Letters* **2011**, 6 (446).
6. Abetz, V.; Simon, P. W., Phase Behaviour and Morphologies of Block Copolymers. In *Block Copolymers I*, Abetz, V., Ed. Springer Berlin Heidelberg: 2005; Vol. 189, pp 125-212.
7. Bates, F. S.; Fredrickson, G. H., Block Copolymers—Designer Soft Materials. *Physics Today* **1999**, 52 (2), 32.
8. Hamley, I. W., *The Physics of Block Copolymers*. 1998.
9. Hamley, I. W., Nanostructure fabrication using block copolymers. *Nanotechnology* **2003**, 14 (10), R39.
10. Hamley, I. W., Ordering in thin films of block copolymers: Fundamentals to potential applications. *Progress in Polymer Science* **2009**, 34 (11), 1161-1210.

11. Harrison, C.; Park, M.; Chaikin, P. M.; Register, R. A.; Adamson, D. H., Lithography with a mask of block copolymer microstructures. *Journal of Vacuum Science & Technology B* **1998**, *16* (2), 544-552.
12. Hawker, C. J.; Russell, T. P., Block Copolymer Lithography: Merging “Bottom-Up” with “Top-Down” Processes. *MRS Bulletin* **2005**, *30* (12), 952-966.
13. Segalman, R. A., Patterning with block copolymer thin films. *Materials Science and Engineering: R: Reports* **2005**, *48* (6), 191-226.
14. Stoykovich, M. P.; Nealey, P. F., Block copolymers and conventional lithography. *Materials Today* **2006**, *9* (9), 20-29.
15. Flory, P. J., *Principles of Polymer Chemistry*. Cornell University Press: Ithaca, United States, 1953; p 688.
16. Bates, F. S.; Fredrickson, G. H., Block Copolymer Thermodynamics: Theory and Experiment. *Annual Review of Physical Chemistry* **1990**, *41* (1), 525-557.
17. de Gennes, P. G., Wetting: statics and dynamics. *Reviews of Modern Physics* **1985**, *57* (3), 827-863.
18. Anastasiadis, S. H.; Russell, T. P.; Satija, S. K.; Majkrzak, C. F., Neutron reflectivity studies of the surface-induced ordering of diblock copolymer films. *Physical Review Letters* **1989**, *62* (16), 1852-1855.
19. Wan, L.; Ruiz, R.; Gao, H.; Patel, K. C.; Albrecht, T. R.; Yin, J.; Kim, J.; Cao, Y.; Lin, G., The Limits of Lamellae-Forming PS-*b*-PMMA Block Copolymers for Lithography. *ACS Nano* **2015**, *9* (7), 7506-7514.

20. Zhao, Y.; Sivaniah, E.; Hashimoto, T., SAXS Analysis of the Order–Disorder Transition and the Interaction Parameter of Polystyrene-block-poly(methyl methacrylate). *Macromolecules* **2008**, *41* (24), 9948-9951.
21. Zha, W.; Han, C. D.; Lee, D. H.; Han, S. H.; Kim, J. K.; Kang, J. H.; Park, C., Origin of the Difference in Order–Disorder Transition Temperature between Polystyrene-block-poly(2-vinylpyridine) and Polystyrene-block-poly(4-vinylpyridine) Copolymers. *Macromolecules* **2007**, *40* (6), 2109-2119.
22. Nose, T., Coexistence curves of polystyrene/ poly(dimethylsiloxane) blends. *Polymer* **1995**, *36* (11), 2243-2248.
23. Russell, T. P.; Hjelm, R. P.; Seeger, P. A., Temperature dependence of the interaction parameter of polystyrene and poly(methyl methacrylate). *Macromolecules* **1990**, *23* (3), 890-893.
24. Hammond, M. R.; Cochran, E.; Fredrickson, G. H.; Kramer, E. J., Temperature Dependence of Order, Disorder, and Defects in Laterally Confined Diblock Copolymer Cylinder Monolayers. *Macromolecules* **2005**, *38* (15), 6575-6585.
25. Frielinghaus, H.; Hermsdorf, N.; Almdal, K.; Mortensen, K.; Messé, L.; Corvazier, L.; Fairclough, J. P. A.; Ryan, A. J.; Olmsted, P. D.; Hamley, I. W., Micro- vs. macro-phase separation in binary blends of poly(styrene)-poly(isoprene) and poly(isoprene)-poly(ethylene oxide) diblock copolymers. *EPL (Europhysics Letters)* **2001**, *53* (5), 680.
26. Cheng, J. Y.; Mayes, A. M.; Ross, C. A., Nanostructure engineering by templated self-assembly of block copolymers. *Nat Mater* **2004**, *3* (11), 823-828.

27. Jung, Y. S.; Ross, C. A., Orientation-Controlled Self-Assembled Nanolithography Using a Polystyrene–Polydimethylsiloxane Block Copolymer. *Nano Letters* **2007**, *7* (7), 2046-2050.
28. Aissou, K.; Choi, H. K.; Nunns, A.; Manners, I.; Ross, C. A., Ordered Nanoscale Archimedean Tilings of a Templated 3-Miktoarm Star Terpolymer. *Nano Letters* **2013**, *13* (2), 835-839.
29. Rodwogin, M. D.; Spanjers, C. S.; Leighton, C.; Hillmyer, M. A., Polylactide–Poly(dimethylsiloxane)–Polylactide Triblock Copolymers as Multifunctional Materials for Nanolithographic Applications. *ACS Nano* **2010**, *4* (2), 725-732.
30. Luo, Y.; Montarnal, D.; Kim, S.; Shi, W.; Barteau, K. P.; Pester, C. W.; Hustad, P. D.; Christianson, M. D.; Fredrickson, G. H.; Kramer, E. J.; Hawker, C. J., Poly(dimethylsiloxane-*b*-methyl methacrylate): A Promising Candidate for Sub-10 nm Patterning. *Macromolecules* **2015**, *48* (11), 3422-3430.
31. Bates, C. M.; Maher, M. J.; Janes, D. W.; Ellison, C. J.; Willson, C. G., Block Copolymer Lithography. *Macromolecules* **2014**, *47* (1), 2-12.
32. Chang, S.-W.; Chuang, V. P.; Boles, S. T.; Ross, C. A.; Thompson, C. V., Densely Packed Arrays of Ultra-High-Aspect-Ratio Silicon Nanowires Fabricated using Block-Copolymer Lithography and Metal-Assisted Etching. *Advanced Functional Materials* **2009**, *19* (15), 2495-2500.
33. Hirai, T.; Leolukman, M.; Liu, C. C.; Han, E.; Kim, Y. J.; Ishida, Y.; Hayakawa, T.; Kakimoto, M.-a.; Nealey, P. F.; Gopalan, P., One-Step Direct-Patterning Template Utilizing Self-Assembly of POSS-Containing Block Copolymers. *Advanced Materials* **2009**, *21* (43), 4334-4338.

34. Borah, D.; Rasappa, S.; Salaun, M.; Zellsman, M.; Lorret, O.; Liontos, G.; Ntetsikas, K.; Avgeropoulos, A.; Morris, M. A., Soft Graphoepitaxy for Large Area Directed Self-Assembly of Polystyrene-block-Poly(dimethylsiloxane) Block Copolymer on Nanopatterned POSS Substrates Fabricated by Nanoimprint Lithography. *Advanced Functional Materials* **2015**, *25* (22), 3425-3432.
35. Borah, D.; Rasappa, S.; Senthamaraiannan, R.; Holmes, J. D.; Morris, M. A., Graphoepitaxial Directed Self-Assembly of Polystyrene-Block-Polydimethylsiloxane Block Copolymer on Substrates Functionalized with Hexamethyldisilazane to Fabricate Nanoscale Silicon Patterns. *Advanced Materials Interfaces* **2014**, *1* (3), n/a-n/a.
36. Rasappa, S.; Schulte, L.; Borah, D.; Morris, M. A.; Ndoni, S., Sub-15 nm Silicon Lines Fabrication via PS-*b*-PDMS Block Copolymer Lithography. *Journal of Nanomaterials* **2013**, *2013*, 7.
37. Mahony, C. T.; Borah, D.; Morris, M. A., Microphase Separation of a PS-*b*-PFS Block Copolymer via Solvent Annealing: Effect of Solvent, Substrate, and Exposure Time on Morphology. *International Journal of Polymer Science* **2015**, *2015*, 10.
38. Borah, D.; Ghoshal, T.; Shaw, M. T.; Chaudhari, A.; Petkov, N.; Bell, A. P.; Holmes, J. D.; Morris, M. A., The Morphology of Ordered Block Copolymer Patterns as Probed by High Resolution Imaging. *Nanomater Nanotechnol* **2014**, *4* (25).
39. Durand, W. J.; Blachut, G.; Maher, M. J.; Sirard, S.; Tein, S.; Carlson, M. C.; Asano, Y.; Zhou, S. X.; Lane, A. P.; Bates, C. M.; Ellison, C. J.; Willson, C. G., Design of high- $\chi$  block copolymers for lithography. *Journal of Polymer Science Part A: Polymer Chemistry* **2015**, *53* (2), 344-352.



40. Lodge, T. P.; Dalvi, M. C., Mechanisms of Chain Diffusion in Lamellar Block Copolymers. *Physical Review Letters* **1995**, *75* (4), 657-660.
41. Clarke, C. J.; Eisenberg, A.; La Scala, J.; Rafailovich, M. H.; Sokolov, J.; Li, Z.; Qu, S.; Nguyen, D.; Schwarz, S. A.; Strzhemechny, Y.; Sauer, B. B., Measurements of the Flory–Huggins Interaction Parameter for Polystyrene–Poly(4-vinylpyridine) Blends. *Macromolecules* **1997**, *30* (14), 4184-4188.
42. Sauer, B. B.; Dee, G. T., Surface Tension and Melt Cohesive Energy Density of Polymer Melts Including High Melting and High Glass Transition Polymers. *Macromolecules* **2002**, *35* (18), 7024-7030.
43. Cummins, C.; Borah, D.; Rasappa, S.; Chaudhari, A.; Ghoshal, T.; O'Driscoll, B. M. D.; Carolan, P.; Petkov, N.; Holmes, J. D.; Morris, M. A., Self-assembly of polystyrene-block-poly(4-vinylpyridine) block copolymer on molecularly functionalized silicon substrates: fabrication of inorganic nanostructured etchmask for lithographic use. *Journal of Materials Chemistry C* **2013**, *1* (47), 7941-7951.
44. Xuan, Y.; Peng, J.; Cui, L.; Wang, H.; Li, B.; Han, Y., Morphology Development of Ultrathin Symmetric Diblock Copolymer Film via Solvent Vapor Treatment. *Macromolecules* **2004**, *37* (19), 7301-7307.
45. Elbs, H.; Drummer, C.; Abetz, V.; Krausch, G., Thin Film Morphologies of ABC Triblock Copolymers Prepared from Solution. *Macromolecules* **2002**, *35* (14), 5570-5577.
46. Huang, W.-H.; Chen, P.-Y.; Tung, S.-H., Effects of Annealing Solvents on the Morphology of Block Copolymer-Based Supramolecular Thin Films. *Macromolecules* **2012**, *45* (3), 1562-1569.

47. Guo, R.; Huang, H.; Chen, Y.; Gong, Y.; Du, B.; He, T., Effect of the Nature of Annealing Solvent on the Morphology of Diblock Copolymer Blend Thin Films. *Macromolecules* **2008**, *41* (3), 890-900.
48. Bosworth, J. K.; Paik, M. Y.; Ruiz, R.; Schwartz, E. L.; Huang, J. Q.; Ko, A. W.; Smilgies, D.-M.; Black, C. T.; Ober, C. K., Control of Self-Assembly of Lithographically Patternable Block Copolymer Films. *ACS Nano* **2008**, *2* (7), 1396-1402.
49. Park, S.; Wang, J.-Y.; Kim, B.; Chen, W.; Russell, T. P., Solvent-Induced Transition from Micelles in Solution to Cylindrical Microdomains in Diblock Copolymer Thin Films. *Macromolecules* **2007**, *40* (25), 9059-9063.
50. *Physical Properties of Polymers Handbook*. Springer-Verlag New York: 2007.
51. O'Driscoll, S.; Demirel, G.; Farrell, R. A.; Fitzgerald, T. G.; O'Mahony, C.; Holmes, J. D.; Morris, M. A., The morphology and structure of PS-*b*-P4VP block copolymer films by solvent annealing: effect of the solvent parameter. *Polymers for Advanced Technologies* **2011**, *22* (6), 915-923.
52. Ghoshal, T.; Ntaras, C.; Shaw, M. T.; Holmes, J. D.; Avgeropoulos, A.; Morris, M. A., A vertical lamellae arrangement of sub-16 nm pitch (domain spacing) in a microphase separated PS-*b*-PEO thin film by salt addition. *Journal of Materials Chemistry C* **2015**, *3* (27), 7216-7227.
53. Park, S.; Wang, J.-Y.; Kim, B.; Xu, J.; Russell, T. P., A Simple Route to Highly Oriented and Ordered Nanoporous Block Copolymer Templates. *ACS Nano* **2008**, *2* (4), 766-772.
54. Park, S.; Kim, B.; Yavuzcetin, O.; Tuominen, M. T.; Russell, T. P., Ordering of PS-*b*-P4VP on Patterned Silicon Surfaces. *ACS Nano* **2008**, *2* (7), 1363-1370.

55. Gowd, E. B.; Nandan, B.; Vyas, M. K.; Bigall, N. C.; Eychmüller, A.; Schlörb, H.; Stamm, M., Highly ordered palladium nanodots and nanowires from switchable block copolymer thin films. *Nanotechnology* **2009**, *20* (41), 415302.

56. Sinturel, C.; Vayer, M.; Morris, M.; Hillmyer, M. A., Solvent Vapor Annealing of Block Polymer Thin Films. *Macromolecules* **2013**, *46* (14), 5399-5415.

57. Strawhecker, K. E.; Kumar, S. K.; Douglas, J. F.; Karim, A., The Critical Role of Solvent Evaporation on the Roughness of Spin-Cast Polymer Films. *Macromolecules* **2001**, *34* (14), 4669-4672.

58. Darling, S. B., Directing the self-assembly of block copolymers. *Progress in Polymer Science* **2007**, *32* (10), 1152-1204

# 4

## Fabrication of Inorganic Nanostructured Etch Mask by Self-Assembly of Polystyrene-*block*-Poly(4-vinylpyridine)

---

### 4.1. Abstract

The self-assembly of block copolymers (BCPs) has the potential to produce nanoscale structures that can be integrated into current silicon based technologies. In order to be useful for the lithographic applications, one of the blocks of the BCP should be removed to transfer the remaining ‘on-chip etch mask’ pattern into underlying substrate. Here, we use high a *chi* ( $\chi$ ) polystyrene-*block*-poly(4-vinylpyridine) (PS-*b*-P4VP) BCP that can phase separate to form sub-7 nm feature size patterns. However, due to the low etch contrast between the blocks, direct pattern transfer of BCP mask is not practical. To overcome the etch contrast problem, a novel and simple *in-situ* hard mask technology is used to fabricate high aspect ratio silicon nanowires on silicon (Si) substrates. Different molecular weight PS-*b*-P4VP BCPs were used to produce lamellae of various feature size by a solvent annealing technique. The lamellar structures were then used to fabricate iron oxide nanowires which facilitated a pattern transfer process to generate silicon nanowires.

### 4.2. Introduction

Due to limitations for sub-30 nm patterning by conventional 193 nm photolithography<sup>1</sup> (which has been used in the semiconductor industry for 20 years), further scaling is becoming prohibitively expensive. As an alternative, block copolymer (BCP) lithography has emerged as a promising high throughput, low-cost alternative, since it can be used to self-assemble

nanostructures at the scale of 5-100 nm.<sup>2,3</sup> BCPs are extremely versatile platforms with which different morphologies including lamellae, hexagonally close-packed cylinders, spheres, and gyroid networks (depending on the volume fractions of the constituent blocks) that can be self-assembled in the bulk or thin films due to the incompatibility between the blocks.<sup>4, 5, 6</sup> The microphase separation of diblock copolymers is thermodynamically driven by the segregation strength  $\chi N$ , the product of the Flory-Huggins interaction parameter  $\chi$  and the degree of polymerization  $N$ . With BCP lithography, long-range ordering of features and etch selectivity between blocks are very important.

Lamellar forming BCPs in thin film form with domain orientations perpendicular to the substrate surface generally adopt characteristic “fingerprint” morphology. These lamellar patterns are favoured over other morphologies due to the ease of pattern transfer but these systems are practically challenging due to the interfacial energies of the substrate surface and the air interface which can lead to horizontal orientations and preferential segregation.<sup>7, 8</sup> To compete with other lithographic technologies, one of the blocks must be removed so that pattern transfer can be performed with high fidelity. Usually, a dry etching method is preferred over wet etching to remove the polymer block, since it avoids capillary induced pattern collapse of small feature polymer blocks.<sup>9</sup> Progress has been made in synthesizing systems that contain elements like silicon (Si) or iron (Fe) in one of the blocks to achieve high etching selectivity, enabling the formation of high aspect ratio features by pattern transfer.<sup>10-13</sup> In recent years, sequential infiltration synthesis (SIS) by atomic layer deposition (ALD) has shown to enhance etch contrast between the blocks of BCPs by effectively forming a ‘hard mask’ for pattern transfer.<sup>14-16</sup> A similar approach has been reported by solvent inclusion of metal ions into the BCP structure to enhance the etch contrast for Si nanofeature fabrication.<sup>17-24</sup>

BCPs with high  $\chi$  parameter are useful for next-generation lithography since they can microphase separate at low BCP molecular weights and so enable small feature size. The use

of high  $\chi$  polymers can also enable reduced line edge roughness.<sup>25</sup> Different high  $\chi$  systems such as poly(cyclohexylethylene)-*block*-polymethmethacrylate (PCHE-*b*-PMMA),<sup>26</sup> poly(styrene-*block*-4-trimethylsilylstyrene) (PS-*b*-PTMSS),<sup>27</sup> poly (styrene-*block*-methyltrimethylsilylmethacrylate) (PS-*b*-PTMSM),<sup>27</sup> poly(4-trimethylsilylstyrene-*block*-*d,l*-lactide) (PTMSS-PLA),<sup>28</sup> poly(dimethylsilacyclobutane)-*block*-poly(methylmethacrylate) (PDMSB-*b*-PMMA)<sup>29</sup> etc. have been synthesized to generate ultra-small feature sizes and can also be used to enhance the etching contrast between the blocks. One of the most used high  $\chi$  BCP systems, polystyrene-*block*-polydimethylsiloxane (PS-*b*-PDMS,  $\chi = 0.26$ )<sup>30</sup> has a Si backbone that enhances etch contrast and facile pattern transfer when used as an on-chip etch mask.<sup>31, 32</sup> Moreover, to achieve the industry required line edge roughness (LER) it is thought that these large  $\chi$  systems have importance as mentioned earlier.<sup>33</sup> However, as  $\chi$  increases, the interdiffusivity of BCPs decreases resulting in slower kinetics during self-assembly.<sup>34</sup> Hence, the drawback of these high  $\chi$  systems, thermal annealing is often not sufficient to obtain well-ordered structures.<sup>35, 36</sup>

In this work, the self-assembly of different molecular weight, high  $\chi$  lamellar polystyrene-*block*-poly(4-vinylpyridine) (PS-*b*-P4VP,  $\chi = 0.34$ ) was carried out using a solvent annealing technique, as described in detail in earlier chapters. The lamellar pattern formed on the Si substrate can be used to template inorganic nanostructures. The microphase separated nanostructures were used to form iron oxide nanowires across a substrate surface by selective filling of one of the block, in this case P4VP. These iron oxide nanowires can be used as hard masks to transfer to the substrate to form silicon nanowires. By using small molecular weight PS-*b*-P4VP, sub-7 nm features of iron oxide nanowires can be fabricated.

### 4.3. Experimental details

#### 4.3.1 Materials and methods

Different molecular weight, high  $\chi$  lamellar PS-*b*-P4VPs were purchased from Polymer Source, Inc. (Montreal, Canada) as shown in Table 4.1. All the polymers were used as received without any purification and modification. All the PS-*b*-P4VP BCPs were dissolved in toluene and tetrahydrofuran (THF) (volume fractions of 80:20) to form a solution with a concentration of 0.5% w/v. The solutions were left stirring overnight to ensure complete dissolution of polymer. Planar substrates, highly polished single-crystal silicon <100> wafers (p-type) with a native oxide layer of ~2 nm, were used. The substrates were cleaned by sonicating for 10 min in toluene and then 10 min in THF. Following the sonication, the substrates were further rinsed with THF, blown dry under a nitrogen stream and a UV/Ozone treatment was used to make the silicon surface more hydrophilic. The substrates were then placed onto holders and BCP thin films were prepared by spin-coating the polymer solution at 3000 rpm for 30 s. The PS-*b*-P4VP thin films were solvent-annealed in toluene, THF and a mixture of toluene/THF (volume fraction of 1:1) depending on the molecular weight of the BCPs, as explained in Chapter 3. All the samples used in this chapter were annealed at 50 °C for 6 h to achieve a good microphase separation. The lamellae of different pitch sizes were formed depending upon the molecular weight of BCP. Fe<sub>2</sub>(NO<sub>3</sub>)<sub>3</sub>·9H<sub>2</sub>O (iron(III) nitrate nonahydrate), THF (inhibitor-free, CHROMASOLV Plus, for HPLC, ≥99.9%), toluene (HROMASOLV Plus, for HPLC, 99.9%), ethanol (dehydrated) were purchased from Sigma-Aldrich and used without purification unless otherwise stated.

**Table 4.1 Molecular characteristics of block copolymers used**

Polymer	Total $M_n$ ( $\times 10^3$ g/mol)	$M_w/M_n$	P4VP fraction	BCP morphology (*)
PS <sub>20k</sub> - <i>b</i> -P4VP <sub>17k</sub>	37.0	1.08	0.46	L
PS <sub>9k</sub> - <i>b</i> -P4VP <sub>9.2k</sub>	18.2	1.09	0.51	L
PS <sub>7.4k</sub> - <i>b</i> -P4VP <sub>7.7k</sub>	15.1	1.08	0.51	L
PS <sub>5k</sub> - <i>b</i> -P4VP <sub>5k</sub>	10	1.1	0.5	L
PS <sub>3.3k</sub> - <i>b</i> -P4VP <sub>3.1k</sub>	6.4	1.2	0.48	L

\*L = Lamellae forming

P4VP dry etch removal was performed with an Oxford plasmatech 100 system in RIE mode using O<sub>2</sub> and CF<sub>4</sub> gases at 100 W for 30 s, the chamber pressure was 15 mTorr and the flow rate of CF<sub>4</sub> was 30 sccm. An STS, Advanced Oxide Etch (AOE) ICP etcher was used to pattern transfer the iron oxide nanowires into the Si substrate using SF<sub>6</sub> and C<sub>4</sub>F<sub>8</sub> mixture in ICP mode at a pressure of 15 mTorr at 10 °C. The C<sub>4</sub>F<sub>8</sub> and SF<sub>6</sub> flow rate was 90 sccm and 30 sccm, respectively.

### 4.3.2 Iron oxide nanowire pattern fabrication

Fe<sub>2</sub>(NO<sub>3</sub>)<sub>3</sub>·9H<sub>2</sub>O (iron(III) nitrate nonahydrate) solutions of 0.3 to 0.5 wt% were prepared in anhydrous ethanol stirred for 20 min. The solution was spin-coated for 30 s at 3000 rpm onto the BCP patterned substrate. Samples were UV/Ozone treated for 3 h in a UV/Ozone system (PSD Pro Series Digital UV Ozone System, Novascan Technologies, Inc., USA).

### 4.3.3 Characterization

Atomic Force Microscopy (AFM) (Park systems, XE-100) in tapping mode under ambient conditions using silicon microcantilever probe tips with a force constant of 42 Nm<sup>-1</sup> was used to record the topographic and phase images of BCP thin films. Scanning electron microscopy (SEM, FEI Helios Nanolab 600i and Raith eLINE Plus) was used to study the surface



morphology of iron oxide nanowires. A Zeiss Orion Plus (Peabody, MA) Helium Ion Microscope (HIM) employing on SE2 detector was used for imaging the block copolymer thin films. Cross-section SEM images were recorded by cleaving the substrate and edges were positioned perpendicular to the incident beam of electrons. X-ray Photoelectron Spectroscopy (XPS) was performed on a Vacuum Science Workshop CLASS100 high performance hemispherical analyser using Al K $\alpha$  X-ray at 200 W power. Spectra were obtained at a take-off angle of 90°.

## 4.4 Results and Discussion

### 4.4.1 Self-assembly of BCP by solvent annealing

All PS-*b*-P4VP block copolymers in this work can be self-assembled into lamellar structures in the presence of solvent vapours. Large molecular weight (PS<sub>20k</sub>-*b*-P4VP<sub>17k</sub> and PS<sub>9k</sub>-*b*-P4VP<sub>9.2k</sub>) BCPs were solvent annealed in THF vapour and formed microphase separated P4VP lamellar microdomains oriented perpendicular to the substrate, as shown in Fig. 4.1 (A) and (B). Lamellae of PS<sub>7.4k</sub>-*b*-P4VP<sub>7.7k</sub> BCP were formed after solvent annealing in a mixture of toluene and THF (50:50, v:v) while small molecular weight (PS<sub>5k</sub>-*b*-P4VP<sub>5k</sub> and PS<sub>3.3k</sub>-*b*-P4VP<sub>3.1k</sub>) BCPs were solvent annealed in toluene as shown in Fig. 4.1 (C-E).

The annealing solvents were carefully chosen and the detailed solvent annealing studies were fully discussed in chapters 2 and 3. The solubility parameters for the solvents ( $\delta_{\text{toluene}} = 18.2 \text{ MPa}^{1/2}$ ,  $\delta_{\text{THF}} = 19.4 \text{ MPa}^{1/2}$ ) and for polymers ( $\delta_{\text{PS}} = 18.6 \text{ MPa}^{1/2}$ ,  $\delta_{\text{P4VP}} = 22.2 \text{ MPa}^{1/2}$ ) are reported elsewhere.<sup>37, 38</sup> These data show that, THF is neutral solvent for the PS block and P4VP block. For large molecular weight PS-*b*-P4VP, THF is a good solvent since it has a preferential affinity to PS block and, hence, it provides sufficient mobility to the block copolymer chains and allowed to self-assemble the blocks into the ordered structures. As-cast film thickness of PS<sub>20k</sub>-*b*-P4VP<sub>17k</sub> and PS<sub>9k</sub>-*b*-P4VP<sub>9.2k</sub> were 35 nm and 28 nm, respectively.

The thickness of BCP thin film formed after solvent annealing showed an increase of 2-3 nm compared to the as-cast film suggesting some trapped free volume. The centre-to-centre distances between two adjacent lamellae are 37 nm and 26 nm for PS<sub>20k</sub>-*b*-P4VP<sub>17k</sub> and PS<sub>9k</sub>-*b*-P4VP<sub>9.2k</sub> systems, respectively.

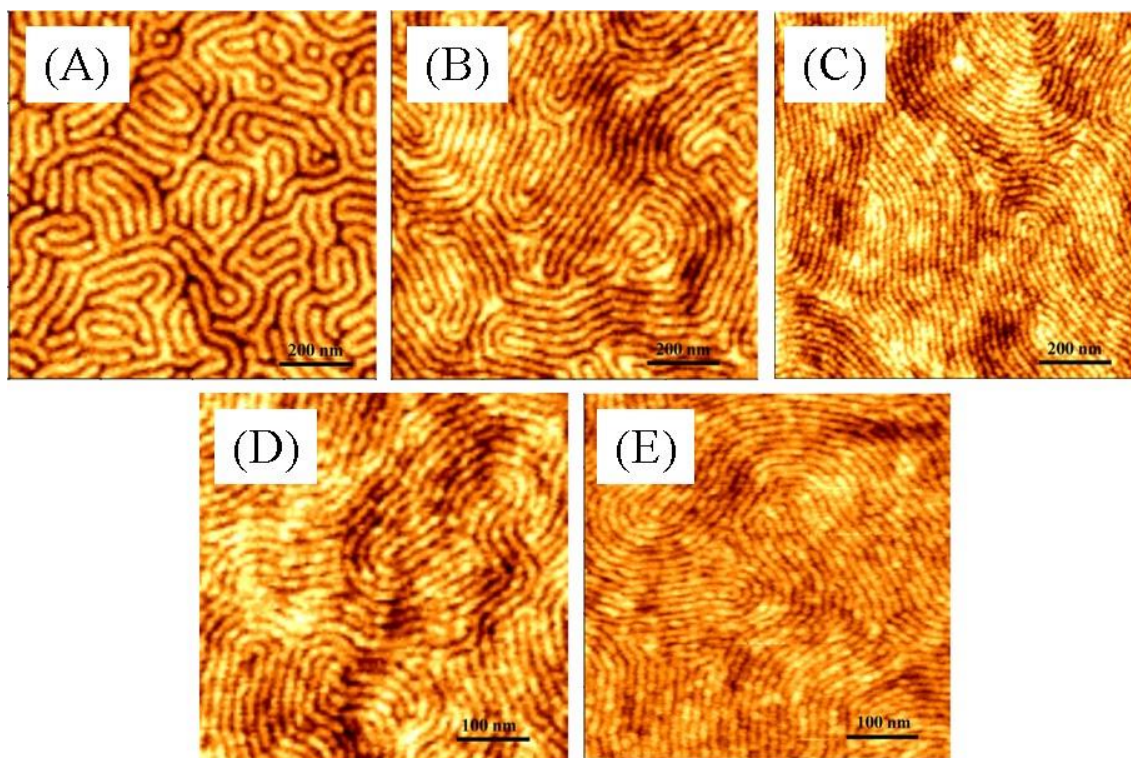


**Figure 4.1.** AFM topographic images of different molecular weight PS-*b*-P4VP BCPs after solvent annealing. The lamellae perpendicular to the substrates were observed in all the BCP systems: (A) PS<sub>20k</sub>-*b*-P4VP<sub>17k</sub>, (B) PS<sub>9k</sub>-*b*-P4VP<sub>9.2k</sub>, (C) PS<sub>7.4k</sub>-*b*-P4VP<sub>7.7k</sub>, (D) PS<sub>5k</sub>-*b*-P4VP<sub>5k</sub>, and (E) PS<sub>3.3k</sub>-*b*-P4VP<sub>3.1k</sub>.

With the decrease in molecular weight of BCPs and thickness of thin film the preference for the annealing solvent changes. In the case of PS<sub>7.4k</sub>-*b*-P4VP<sub>7.7k</sub>, the thickness of as-cast film is 23 nm, after solvent annealing in the mixture of toluene/THF (50:50, v:v) at 50 °C for 6 h, the thickness was increased by 1 nm. The vapour pressure of toluene (92 mmHg) is much lower than of THF (420 mmHg) at 50 °C. It can, therefore, be concluded that the increase in thickness

on solvent annealing is due to the presence of THF which causes increased film swelling. The lamellar domain spacing is 19 nm, as shown in Fig. 4.1 (C).

As shown in Fig. 4.1 (D-E), the smaller molecular weight PS-*b*-P4VP (PS<sub>5k</sub>-*b*-P4VP<sub>5k</sub> and PS<sub>3.3k</sub>-*b*-P4VP<sub>3.1k</sub>) BCPs were annealed in toluene vapours at 50 °C for 6 h. If THF was used, the high vapour pressure of THF led to dewetting the films in a few minutes. The difference in film thickness of as-cast and annealed film for these samples was negligible. The film thickness of as-cast PS<sub>5k</sub>-*b*-P4VP<sub>5k</sub> and PS<sub>3.3k</sub>-*b*-P4VP<sub>3.1k</sub> is measured at 18 and 14 nm and the domain spacings were 15 nm and 10.5 nm, respectively.

#### 4.4.2 BCP imaging by Helium Ion Microscopy

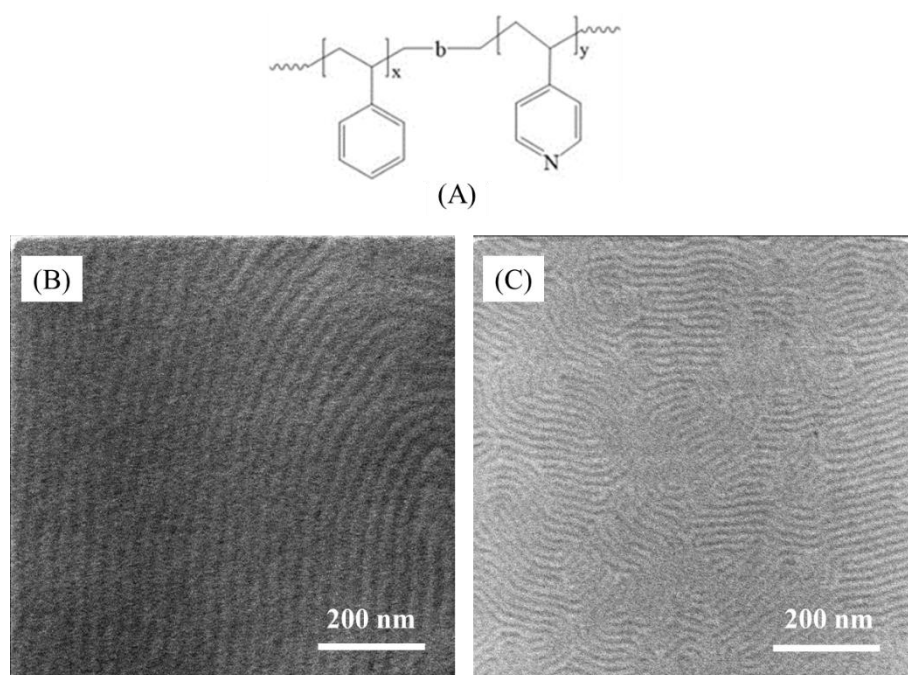


**Figure 4.2.** (A) Chemical structure of PS-*b*-P4VP. (B) and (C) are HIM images of unetched PS<sub>9k</sub>-*b*-P4VP<sub>9.2k</sub> and PS<sub>5k</sub>-*b*-P4VP<sub>5k</sub>.

Due to the very similar chemical composition of both PS and P4VP (Fig. 4.2-A), this BCP exhibits very low etch contrast. For the same reason, SEM imaging provided only featureless data due to the limited contrast issues between blocks. Scanning Helium Ion Microscopy (HIM)

may prove to be an important imaging technique to image these types of BCPs because of its ability to discriminate similar molecules.<sup>39</sup> As shown in Fig. 4.2 (B-C), the HIM is used to study the nanopatterns formed by PS<sub>9k</sub>-*b*-P4VP<sub>9.2k</sub> and PS<sub>5k</sub>-*b*-P4VP<sub>5k</sub> BCP thin films. The lamellar pattern with 25 nm and 15 nm pitch are observed for both the BCP systems. These data demonstrate that HIM can discriminate between the blocks without any further processing.

#### 4.4.3 Etching of PS-*b*-P4VP

The phase separated block copolymer pattern formed during the annealing process is not immediately useful as a lithographic mask. In order to fulfil the templating and pattern transfer potential, the BCP films require either wet or dry etching.<sup>7, 40-43</sup> Park et al. first demonstrated the use of BCP films as etch masks to transfer the patterns to an underlying semiconductor substrate.<sup>44</sup> As shown in Fig. 4.3, the PS<sub>9k</sub>-*b*-P4VP<sub>9.2k</sub> lamellae formed after solvent annealing were dry etched by using O<sub>2</sub> and CF<sub>4</sub> gases at 100 W for 30 s. In this image the contrast is very low suggesting only small amount of the polymers are present.

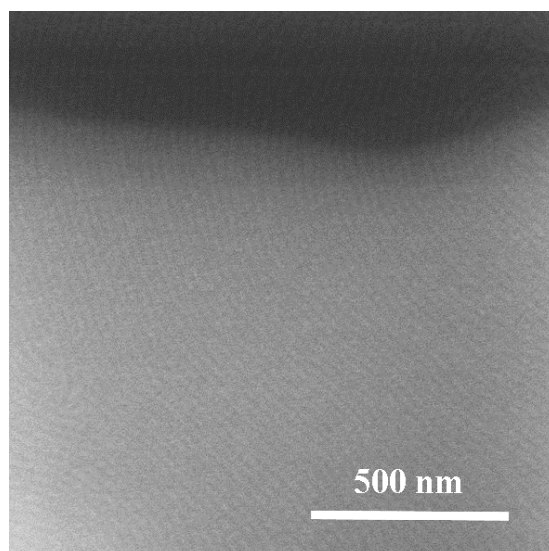


**Figure 4.3.** SEM image of PS<sub>9k</sub>-*b*-P4VP<sub>9.2k</sub> film post 30 s RIE with flow rate of 30 sccm CF<sub>4</sub> / 5 sccm O<sub>2</sub> at 15 mTorr.

It should be noted that in order to optimize etching procedure, the etch selectivity of the blocks were studied by comparing the etch rates of homopolymer films in a similar approach to methods outlined elsewhere.<sup>7</sup> The difference in the etching rates of both the blocks is very small. For this BCP system, the selective removal of one of the block was not successful which further hinders the pattern transfer into the silicon substrates.

#### **4.4.4. Iron oxide nanowires fabrication by a solvent inclusion technique**

The BCP systems containing an inorganic block have been reviewed recently showing potential for lithographic applications.<sup>45</sup> Since both PS and P4VP blocks are organic and have very low etch contrast, it is necessary to increase the etching contrast between the blocks. One way this can be achieved is that one of the lamellae can be functionalized by using electronically, optically, or magnetically active species to make them applicable in semiconductor industry or in photonic devices. Iron oxide nanowires are formed by simple inclusion of iron ions by spin coating iron nitrate solution from ethanol into the P4VP block. Ethanol selectively swells the P4VP block, since the PS block is insoluble in ethanol, decreasing the density of P4VP microdomains. The P4VP block has a Brönsted base character (proton acceptor) owing to the pyridine groups ( $pK_b \sim 5$ ),<sup>46</sup> as well as having the potential to act as a metal ligand to coordinate with metal complexes.<sup>47</sup> Acidification leads formation of the swollen, protonated P4VP structures allowing contact with the anionic metal complexes through electrostatic attraction. Following exposure to the UV/ozone, the block copolymer is removed to form the oxide nanowires.

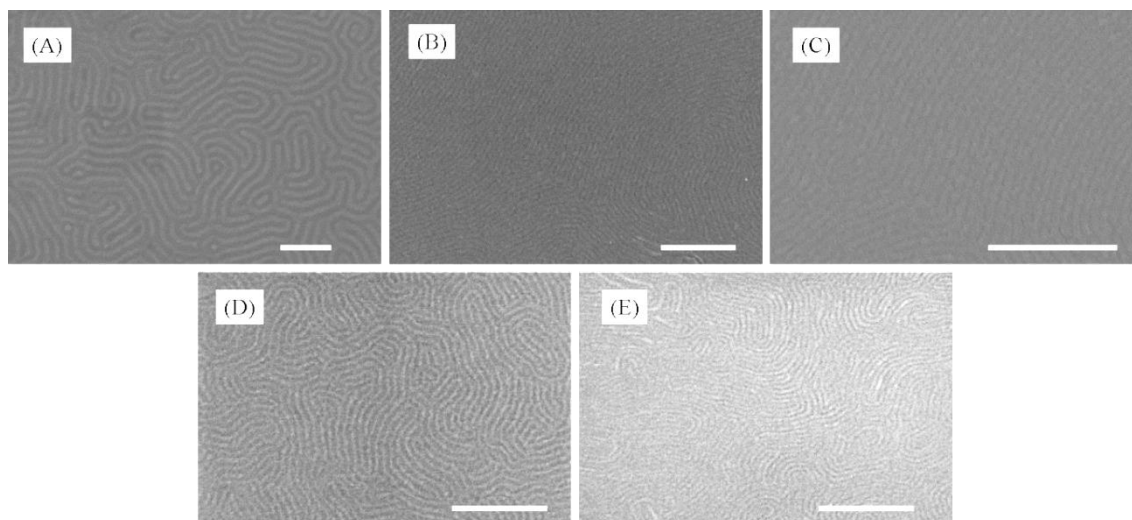


**Figure 4.4.** Top-down SEM images of iron oxide nanowires formed by using (A) PS<sub>20k</sub>-*b*-P4VP<sub>17k</sub>, (B) PS<sub>9k</sub>-*b*-P4VP<sub>9.2k</sub>, (C) PS<sub>7.4k</sub>-*b*-P4VP<sub>7.7k</sub>, (D) PS<sub>5k</sub>-*b*-P4VP<sub>5k</sub> and (E) PS<sub>3.3k</sub>-*b*-P4VP<sub>3.1k</sub>. All scale bars represent 200 nm.

The general methodology is as explained by Ghoshal et al.<sup>20</sup> Here, microphase separated PS-*b*-PEO nanostructures are formed after solvent annealing are immersed in ethanol to produce the nanoporous structures. These nanoporous templates can be used to create ordered nanodots or nanowires arrays by the Ghoshal metal inclusion method.<sup>29-36, 47, 48</sup> Here we use a similar method to increase the high etch contrast by introducing robust inorganic moiety as shown in Fig. 4.4. It should be noted that the concentration of iron precursor solution used is critical. For larger molecular weight BCPs (PS<sub>20k</sub>-*b*-P4VP<sub>17k</sub> and PS<sub>9k</sub>-*b*-P4VP<sub>9.2k</sub>), 0.5 wt% solution of iron nitrate from ethanol was used. Larger concentrations result in overloading and it reduces the fidelity of the pattern transfer process. For other PS-*b*-P4VP systems (PS<sub>7.4k</sub>-*b*-P4VP<sub>7.7k</sub>, PS<sub>5k</sub>-*b*-P4VP<sub>5k</sub> and PS<sub>3.3k</sub>-*b*-P4VP<sub>3.1k</sub>), a 0.3 wt% precursor solution was used for the same reasons - i.e. avoiding overflow.

In order to quantify the surface composition, XPS analysis was performed on the iron oxide nanowires samples, as shown in Fig. 4.5. A typical XPS survey spectrum of the sample confirms the presence of Si, C, O and Fe (Fig. 4.5-A). The Si, O and Fe features originate from

the Si substrate, the native oxide layer and iron oxide nanowires, respectively. The high intensity of C1s features is expected from adventitious contamination during sample preparation.

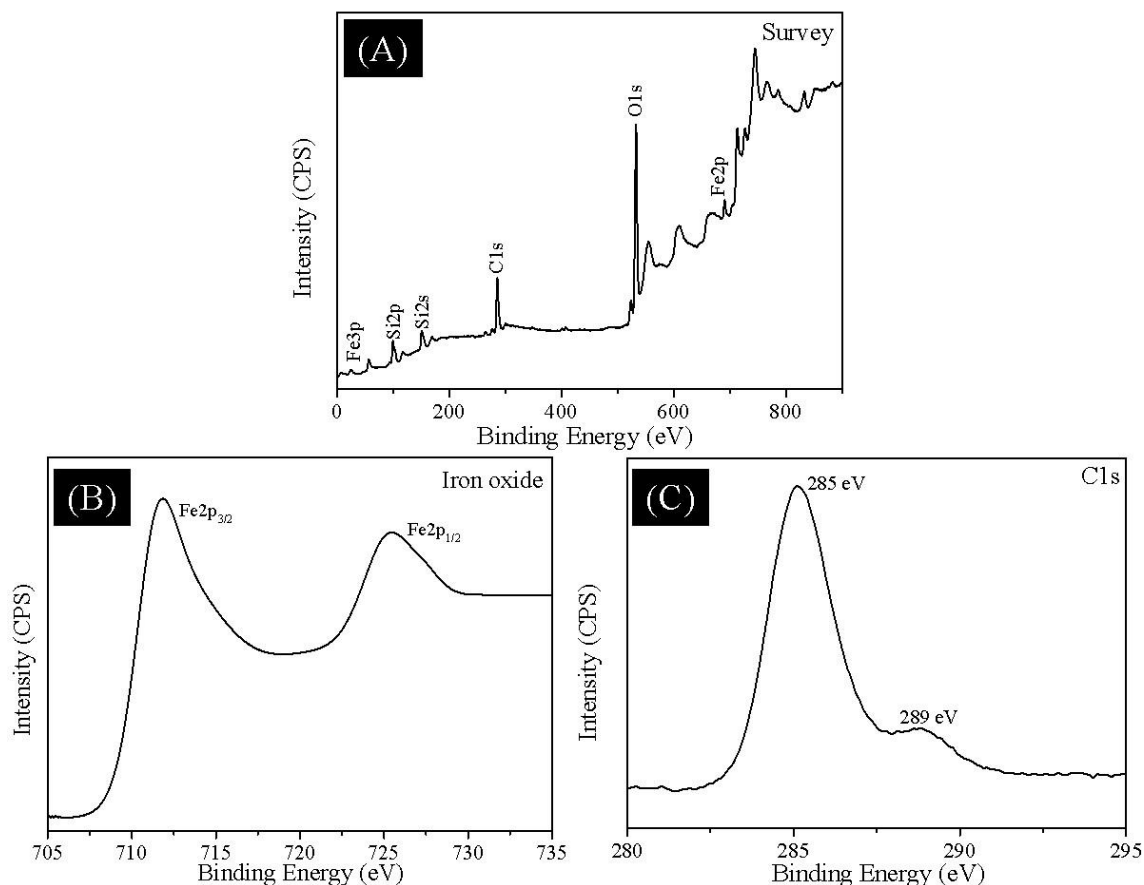


**Figure 4.5.** (A) XPS survey spectra recorded from the iron oxide nanowires on Si substrate after UV/Ozone treatment. (B) and (C) are the high resolution Fe2p and C1s spectra of iron oxide nanowires on the Si substrate.

Additional higher resolution spectrum of Fe2p and C1s signals were recorded for further investigation. As shown in Fig. 4.5-(B), the Fe2p core level spectrum consists of two sharp peaks at 711.8 eV and 725.4 eV associated with Fe2p<sub>3/2</sub> and Fe2p<sub>1/2</sub>, respectively. The binding energies of these are consistent with the existence of Fe<sup>+3</sup> ions only, implying the presence of the iron oxide as the Fe<sub>2</sub>O<sub>3</sub> structure.<sup>49, 50</sup> The C1s spectrum, as shown in Fig. 4.5-(C), exhibits a major peaks at 285 eV and a minor peak at 289 eV. The peak at 285 eV is assigned to the

adventitious carbon, whereas the peak at 289 eV suggest the existence of a functional group (C=O),<sup>51</sup> due to the oxidation of carbon during UV/ozone treatment.

We can conclude from these data that the metal ion inclusion into the BCP template is favoured by a combination of capillary forces and the affinity of P4VP with the ionic ethanol solution. Metal counter ions can interact with the pyridine group, which becomes pyridinium group after protonation, of the P4VP block. The protonated P4VP offers the possibility to make metal structures by reduction of coordinated metal counter ions.<sup>52, 53</sup> After the UV/Ozone treatment, almost complete removal of organic polymers was possible since only residual oxidized carbon was visible and the overall process allows iron oxide nanowire formation to take place. The feature size of iron oxide nanowires can be varied by the molecular weight of the BCP but here, as shown in Fig. 4.4, the feature size was very effectively controlled by using different molecular weight PS-*b*-P4VP system. The use of small molecular weight PS<sub>3.3k</sub>-*b*-P4VP<sub>3.1k</sub> produces iron oxide nanowires with a feature size of 6 nm (Fig. 4.4-(E)).

#### 4.4.5. Pattern transfer of iron oxide nanowires into Si-substrate

In order to create Si nanowire structures on the substrate surface, the iron oxide nanowires were used as a hard mask in the ICP etch process. Figure 4.6-(A) shows an SEM image of iron oxide nanowire formed by using the PS<sub>20k</sub>-*b*-P4VP<sub>17k</sub> BCP on a Si substrate. The iron oxide nanowires formed are continuous with feature size of 18 nm and the centre-to-centre nanowire spacing is 35 nm which was unchanged from that of the solvent annealed film. The Si etch was carried out by using C<sub>4</sub>F<sub>8</sub>-SF<sub>6</sub>.



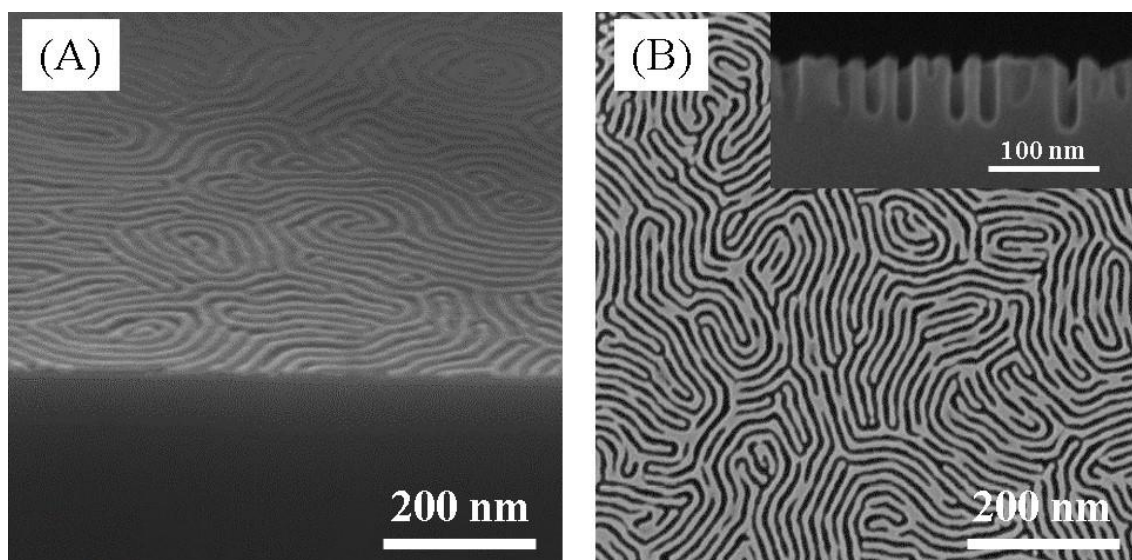


**Figure 4.6.** (A) SEM image of iron oxide nanowires formed using PS<sub>20k</sub>-*b*-P4VP<sub>17k</sub> and (B) is SEM image of pattern transferred Si nanostructures, inset shows cross sectional SEM image.

The top-down SEM image as shown in Fig. 4.6-B, is of Si nanowires formed after pattern transfer of the iron oxide nanowires using the ICP Si etch. The line-edge roughness (LER) of the Si nanowires can be observed due to the extended plasma etching of iron oxide nanowires. The inset of Fig. 4.6-B shows cross-section SEM of Si structures where the Si was etched for 90 s.

Pattern transfer of the iron oxide mask to create a high aspect ratio silicon structure is challenging. To obtain high fidelity nanoscale pattern transfer without e.g. an undercut, various parameters were studied. In this study, a one-step ICP pattern transfer recipe was preferred by using C<sub>4</sub>F<sub>8</sub> and SF<sub>6</sub> at a flow rate of 90 sccm and 30 sccm, respectively. No oxide etch recipe was employed to remove the native oxide layer. During ICP etching, the anisotropic distribution preferentially bombards and removes the passivant formed at the bottom of the silicon trench, which during etching of silicon produces high aspect ratio features with vertical sidewalls.

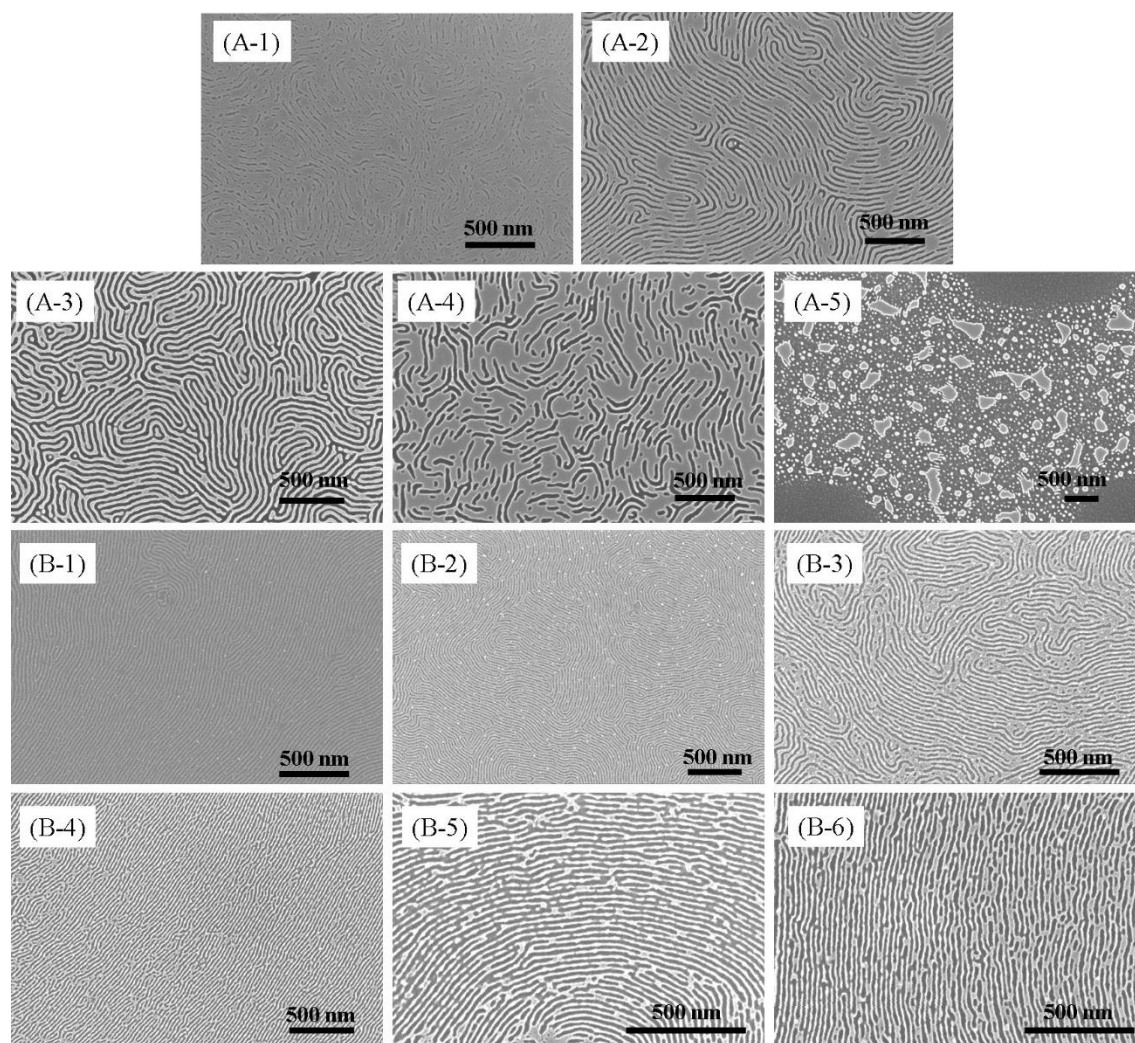


**Figure 4.7.** Top-down SEM images of progressive Si etch after various etch periods (conditions  $C_4F_8$  and  $SF_6$  at the flow rate of 90 sccm and 30 sccm, respectively at 10 Torr and  $10^\circ C$ ). (A-1 to A-5) are Si nanowires fabricated by using  $PS_{20k}-b-P4VP_{17k}$  at different etching times 10 s (A-1), 40 s (A-2), 90 s (A-3), 120 s (A-4) and 150 s (A-5). (B-1 to B-6) are Si nanowires fabricated by using  $PS_{9k}-b-P4VP_{9.2k}$  at different etching times 5 s (B-1), 10 s (B-2), 15 s (B-3), 20 s (B-4), 30 s (B-5) and 60 s (B-6).

A systematic study of the pattern transfer of iron oxide nanowires formed by using  $PS_{20k}-b-P4VP_{17k}$  (A-1 to A-5) and  $PS_{9k}-b-P4VP_{9.2k}$  (B-1 to B-6) were studied as shown in Fig. 4.7. The iron oxide nanowires formed by using  $PS_{20k}-b-P4VP_{17k}$  BCP system with centre-to-centre distance of 35 nm were pattern transferred in  $C_4F_8$  and  $SF_6$  gases for various times between 10-

150 s. After 10 s (A-1) of ICP etching a small increase in the patterns was seen. As the etch time changed to 40 s (A-2) and 90 s (A-3), the image contrast is increased but no change in feature size was observed. With further increases in time the hard etch mask appears to be removed and produces degraded structures, as shown in Fig. 4.7 (A-4 and A-5).

The same method is capable of being scaled for patterning smaller features by reducing the molecular weight of the block copolymer. The PS<sub>9k</sub>-*b*-P4VP<sub>9.2k</sub> BCP system produces iron oxide nanowires of pitch size of ~25 nm. The iron oxide nanowires were used as mask to pattern transfer into silicon. The Si nanowires were formed as shown in Fig. 4.7 (B-1 to B-6). By lowering the molecular weight of the block copolymer, the increase in areal density of the silicon nanowire patterns were observed. It is important to note that the smaller feature size iron oxide nanowires require less ICP etching time. The 5 s Si etch (B-1) produces a good contrast for small molecular weight system. However, by increasing the etching time the contrast is increased indicating deep etches. The samples were etched for 5-60 s to produce the Si nanowires. To compare the results of the Si nanowires formed by using both the block copolymer system, it was observed that the smaller features requires less etching time and the degradation of the structure observed in less than 60 s of etching (B-6).

#### 4.5 Conclusions

In conclusion, we have demonstrated a simple route to fabricate a low cost and industrial compatible methodology to fabricate metal oxide nanowires which has significant potential in the semiconductor industry. The formation of the block copolymer pattern formation by solvent annealing was a very simple process and requires low temperature and low times. A metal oxide precursor solution was spin-coated on the lamellae of PS-*b*-P4VP followed by UV/Ozone treatment and results in both polymer removal and metal oxide nanowire formation on the silicon substrate. The metal oxide nanowires formed are mirrors of the parent block copolymer

structure. The iron oxide nanowire structure formed was confirmed by XPS studies. Metal oxide nanowires can be prepared for small molecular weight BCP systems and used to fabricate ultra-small sub-7 nm feature size. The metal oxide nanowires were then pattern transferred into silicon substrate to produce silicon nanowires.

## 4.6 References

1. Harriott, L. R., Limits of lithography. *Proceedings of the IEEE* **2001**, 89 (3), 366-374.
2. Stoykovich, M. P.; Nealey, P. F., Block copolymers and conventional lithography. *Materials Today* **2006**, 9 (9), 20-29.
3. Bates, F. S.; Fredrickson, G. H., Block Copolymer Thermodynamics: Theory and Experiment. *Annual Review of Physical Chemistry* **1990**, 41 (1), 525-557.
4. Hamley, I. W., Nanotechnology with Soft Materials. *Angewandte Chemie International Edition* **2003**, 42 (15), 1692-1712.
5. Park, C.; Yoon, J.; Thomas, E. L., Enabling nanotechnology with self-assembled block copolymer patterns. *Polymer* **2003**, 44 (22), 6725-6760.
6. Bates, C. M.; Maher, M. J.; Janes, D. W.; Ellison, C. J.; Willson, C. G., Block Copolymer Lithography. *Macromolecules* **2014**, 47 (1), 2-12.
7. Farrell, R. A.; Petkov, N.; Shaw, M. T.; Djara, V.; Holmes, J. D.; Morris, M. A., Monitoring PMMA Elimination by Reactive Ion Etching from a Lamellar PS-*b*-PMMA Thin Film by ex Situ TEM Methods. *Macromolecules* **2010**, 43 (20), 8651-8655.
8. Potemkin, I. I., Lamellar Orientation in Thin, Supported Diblock Copolymer Films: Strong Segregation Theory. *Macromolecules* **2004**, 37 (9), 3505-3509.
9. Liu, C.-C.; Nealey, P. F.; Ting, Y.-H.; Wendt, A. E., Pattern transfer using poly(styrene-*block*-methyl methacrylate) copolymer films and reactive ion etching. *Journal of Vacuum Science & Technology B* **2007**, 25 (6), 1963-1968.
10. Manners, I., Side-Chain Metal-Containing Polymers. In *Synthetic Metal-Containing Polymers*, Wiley-VCH Verlag GmbH & Co. KGaA: 2004; pp 39-70.

11. Cheng, J. Y.; Mayes, A. M.; Ross, C. A., Nanostructure engineering by templated self-assembly of block copolymers. *Nat Mater* **2004**, *3* (11), 823-828.
12. Lammertink, R. G. H.; Hempenius, M. A.; van den Enk, J. E.; Chan, V. Z. H.; Thomas, E. L.; Vancso, G. J., Nanostructured Thin Films of Organic–Organometallic Block Copolymers: One-Step Lithography with Poly(ferrocenylsilanes) by Reactive Ion Etching. *Advanced Materials* **2000**, *12* (2), 98-103.
13. Jung, Y. S.; Ross, C. A., Orientation-Controlled Self-Assembled Nanolithography Using a Polystyrene–Polydimethylsiloxane Block Copolymer. *Nano Letters* **2007**, *7* (7), 2046-2050.
14. Tseng, Y.-C.; Peng, Q.; Ocola, L. E.; Czaplewski, D. A.; Elam, J. W.; Darling, S. B., Enhanced polymeric lithography resists via sequential infiltration synthesis. *Journal of Materials Chemistry* **2011**, *21* (32), 11722-11725.
15. Biswas, M.; Libera, J. A.; Darling, S. B.; Elam, J. W., Kinetics for the Sequential Infiltration Synthesis of Alumina in Poly(methyl methacrylate): An Infrared Spectroscopic Study. *The Journal of Physical Chemistry C* **2015**, *119* (26), 14585-14592.
16. Biswas, M.; Libera, J. A.; Darling, S. B.; Elam, J. W., New Insight into the Mechanism of Sequential Infiltration Synthesis from Infrared Spectroscopy. *Chemistry of Materials* **2014**, *26* (21), 6135-6141.
17. Cummins, C.; Gangnaik, A.; Kelly, R. A.; Borah, D.; O'Connell, J.; Petkov, N.; Georgiev, Y. M.; Holmes, J. D.; Morris, M. A., Aligned silicon nanofins via the directed self-assembly of PS-*b*-P4VP block copolymer and metal oxide enhanced pattern transfer. *Nanoscale* **2015**, *7* (15), 6712-6721.
18. Cummins, C.; Kelly, R. A.; Gangnaik, A.; Georgiev, Y. M.; Petkov, N.; Holmes, J. D.; Morris, M. A., Solvent Vapor Annealing of Block Copolymers in Confined Topographies:

Commensurability Considerations for Nanolithography. *Macromolecular Rapid Communications* **2015**, *36* (8), 762-767.

19. Cummins, C.; Gangnaik, A.; Kelly, R. A.; Hydes, A. J.; O'Connell, J.; Petkov, N.; Georgiev, Y. M.; Borah, D.; Holmes, J. D.; Morris, M. A., Parallel Arrays of Sub-10 nm Aligned Germanium Nanofins from an In Situ Metal Oxide Hardmask using Directed Self-Assembly of Block Copolymers. *Chemistry of Materials* **2015**.

20. Ghoshal, T.; Sentharamaikkannan, R.; Shaw, M. T.; Holmes, J. D.; Morris, M. A., "In situ" hard mask materials: a new methodology for creation of vertical silicon nanopillar and nanowire arrays. *Nanoscale* **2012**, *4* (24), 7743-7750.

21. Ghoshal, T.; Maity, T.; Godsell, J. F.; Roy, S.; Morris, M. A., Large Scale Monodisperse Hexagonal Arrays of Superparamagnetic Iron Oxides Nanodots: A Facile Block Copolymer Inclusion Method. *Advanced Materials* **2012**, *24* (18), 2390-2397.

22. Cummins, C.; Borah, D.; Rasappa, S.; Chaudhari, A.; Ghoshal, T.; O'Driscoll, B. M. D.; Carolan, P.; Petkov, N.; Holmes, J. D.; Morris, M. A., Self-assembly of polystyrene-*block*-poly(4-vinylpyridine) block copolymer on molecularly functionalized silicon substrates: fabrication of inorganic nanostructured etchmask for lithographic use. *Journal of Materials Chemistry C* **2013**, *1* (47), 7941-7951.

23. Ghoshal, T.; Maity, T.; Sentharamaikkannan, R.; Shaw, M. T.; Carolan, P.; Holmes, J. D.; Roy, S.; Morris, M. A., Size and space controlled hexagonal arrays of superparamagnetic iron oxide nanodots: magnetic studies and application. *Scientific Reports* **2013**, *3*, 2772.

24. Ghoshal, T.; Sentharamaikkannan, R.; Shaw, M. T.; Holmes, J. D.; Morris, M. A., Fabrication of Ordered, Large Scale, Horizontally-Aligned Si Nanowire Arrays Based on an In Situ Hard Mask Block Copolymer Approach. *Advanced Materials* **2014**, *26* (8), 1207-1216.

25. Semenov, A. N., Theory of block copolymer interfaces in the strong segregation limit. *Macromolecules* **1993**, *26* (24), 6617-6621.
26. Kennemur, J. G.; Yao, L.; Bates, F. S.; Hillmyer, M. A., Sub-5 nm Domains in Ordered Poly(cyclohexylethylene)-block-poly(methyl methacrylate) Block Polymers for Lithography. *Macromolecules* **2014**, *47* (4), 1411-1418.
27. Maher, M. J.; Bates, C. M.; Blachut, G.; Sirard, S.; Self, J. L.; Carlson, M. C.; Dean, L. M.; Cushen, J. D.; Durand, W. J.; Hayes, C. O.; Ellison, C. J.; Willson, C. G., Interfacial Design for Block Copolymer Thin Films. *Chemistry of Materials* **2014**, *26* (3), 1471-1479.
28. Kim, S.; Bates, C. M.; Thio, A.; Cushen, J. D.; Ellison, C. J.; Willson, C. G.; Bates, F. S., Consequences of Surface Neutralization in Diblock Copolymer Thin Films. *ACS Nano* **2013**, *7* (11), 9905-9919.
29. Aissou, K.; Mumtaz, M.; Fleury, G.; Portale, G.; Navarro, C.; Cloutet, E.; Brochon, C.; Ross, C. A.; Hadziioannou, G., Sub-10 nm Features Obtained from Directed Self-Assembly of Semicrystalline Polycarbosilane-Based Block Copolymer Thin Films. *Advanced Materials* **2015**, *27* (2), 261-265.
30. Nose, T., Coexistence curves of polystyrene/ poly(dimethylsiloxane) blends. *Polymer* **1995**, *36* (11), 2243-2248.
31. Borah, D.; Rasappa, S.; Senthamaraiannan, R.; Holmes, J. D.; Morris, M. A., Graphoepitaxial Directed Self-Assembly of Polystyrene-Block-Polydimethylsiloxane Block Copolymer on Substrates Functionalized with Hexamethyldisilazane to Fabricate Nanoscale Silicon Patterns. *Advanced Materials Interfaces* **2014**, *1* (3), n/a-n/a.
32. Borah, D.; Ozmen, M.; Rasappa, S.; Shaw, M. T.; Holmes, J. D.; Morris, M. A., Molecularly Functionalized Silicon Substrates for Orientation Control of the Microphase



Separation of PS-*b*-PMMA and PS-*b*-PDMS Block Copolymer Systems. *Langmuir* **2013**, *29* (9), 2809-2820.

33. Patrone, P. N.; Gallatin, G. M., Modeling Line Edge Roughness in Templated, Lamellar Block Copolymer Systems. *Macromolecules* **2012**, *45* (23), 9507-9516.

34. Lodge, T. P.; Dalvi, M. C., Mechanisms of Chain Diffusion in Lamellar Block Copolymers. *Physical Review Letters* **1995**, *75* (4), 657-660.

35. Park, W. I.; Kim, K.; Jang, H.-I.; Jeong, J. W.; Kim, J. M.; Choi, J.; Park, J. H.; Jung, Y. S., Directed Self-Assembly with Sub-100 Degrees Celsius Processing Temperature, Sub-10 Nanometer Resolution, and Sub-1 Minute Assembly Time. *Small* **2012**, *8* (24), 3762-3768.

36. Gotrik, K. W.; Hannon, A. F.; Son, J. G.; Keller, B.; Alexander-Katz, A.; Ross, C. A., Morphology Control in Block Copolymer Films Using Mixed Solvent Vapors. *ACS Nano* **2012**, *6* (9), 8052-8059.

37. *Polymer Handbook*. 4 ed.; p 2336.

38. Barton, A. F. M., *CRC Handbook of Solubility Parameters and Other Cohesion Parameters*. 2 ed.; CRC Press

39. Bell, A. P.; Senthamaraiannan, R.; Ghoshal, T.; Chaudhari, A.; Shaw, M. T.; Lesson, M.; Morris, M. A., The development and advantages of helium ion microscopy for the study of block copolymer nanopatterns. *Proc. SPIE 9424, Metrology, Inspection, and Process Control for Microlithography XXIX* **2015**, 13.

40. Zhang, M.; Yang, L.; Yurt, S.; Misner, M. J.; Chen, J. T.; Coughlin, E. B.; Venkataraman, D.; Russell, T. P., Highly Ordered Nanoporous Thin Films from Cleavable Polystyrene-*block*-poly(ethylene oxide). *Advanced Materials* **2007**, *19* (12), 1571-1576.

41. Zschech, D.; Kim, D. H.; Milenin, A. P.; Scholz, R.; Hillebrand, R.; Hawker, C. J.; Russell, T. P.; Steinhart, M.; Gösele, U., Ordered Arrays of  $\langle 100 \rangle$  -Oriented Silicon Nanorods by CMOS-Compatible Block Copolymer Lithography. *Nano Letters* **2007**, *7* (6), 1516-1520.
42. Hirai, T.; Leolukman, M.; Liu, C. C.; Han, E.; Kim, Y. J.; Ishida, Y.; Hayakawa, T.; Kakimoto, M.-a.; Nealey, P. F.; Gopalan, P., One-Step Direct-Patterning Template Utilizing Self-Assembly of POSS-Containing Block Copolymers. *Advanced Materials* **2009**, *21* (43), 4334-4338.
43. Ting, Y.-H.; Park, S.-M.; Liu, C.-C.; Liu, X.; Himpfel, F. J.; Nealey, P. F.; Wendt, A. E., Plasma etch removal of poly(methyl methacrylate) in block copolymer lithography. *Journal of Vacuum Science & Technology B* **2008**, *26* (5), 1684-1689.
44. Park, M.; Harrison, C.; Chaikin, P. M.; Register, R. A.; Adamson, D. H., Block Copolymer Lithography: Periodic Arrays of  $\sim 10^{11}$  Holes in 1 Square Centimeter. *Science* **1997**, *276* (5317), 1401-1404.
45. Nunns, A.; Gwyther, J.; Manners, I., Inorganic block copolymer lithography. *Polymer* **2013**, *54* (4), 1269-1284.
46. Satoh, M.; Yoda, E.; Hayashi, T.; Komiyama, J., Potentiometric titration of poly(vinylpyridines) and hydrophobic interaction in the counterion binding. *Macromolecules* **1989**, *22* (4), 1808-1812.
47. Aizawa, M.; Buriak, J. M., Nanoscale Patterning of Two Metals on Silicon Surfaces Using an ABC Triblock Copolymer Template. *Journal of the American Chemical Society* **2006**, *128* (17), 5877-5886.

48. Ghoshal, T.; Shaw, M. T.; Bolger, C. T.; Holmes, J. D.; Morris, M. A., A general method for controlled nanopatterning of oxide dots: a microphase separated block copolymer platform. *Journal of Materials Chemistry* **2012**, *22* (24), 12083-12089.
49. Fujii, T.; de Groot, F. M. F.; Sawatzky, G. A.; Voogt, F. C.; Hibma, T.; Okada, K., In-situ XPS analysis of various iron oxide films grown by NO<sub>2</sub>- assisted molecular-beam epitaxy. *Physical Review B* **1999**, *59* (4), 3195-3202.
50. Yamashita, T.; Hayes, P., Analysis of XPS spectra of Fe<sup>2+</sup> and Fe<sup>3+</sup> ions in oxide materials. *Applied Surface Science* **2008**, *254* (8), 2441-2449.
51. Yin, Y.; Hu, Y.; Wu, P.; Zhang, H.; Cai, C., A graphene-amorphous FePO<sub>4</sub> hollow nanosphere hybrid as a cathode material for lithium ion batteries. *Chemical Communications* **2012**, *48* (15), 2137-2139.
52. Spatz, J. P.; Mössmer, S.; Hartmann, C.; Möller, M.; Herzog, T.; Krieger, M.; Boyen, H.-G.; Ziemann, P.; Kabius, B., Ordered Deposition of Inorganic Clusters from Micellar Block Copolymer Films. *Langmuir* **2000**, *16* (2), 407-415.
53. Spatz, J. P.; Herzog, T.; Mößmer, S.; Ziemann, P.; Möller, M., Micellar Inorganic–Polymer Hybrid Systems—A Tool for Nanolithography. *Advanced Materials* **1999**, *11* (2), 149-153.

# 5

## Fabrication of a Layered MoS<sub>2</sub> Structure *via* the Self-Assembly of Block Copolymers.

---

### 5.1. Abstract

The semiconductor and optical industries have shown increasing interest in two dimensional molybdenum disulphide (MoS<sub>2</sub>) as a potential device material due to its low band gap and high electron mobility. However, current methods for its synthesis are not ‘fab’ friendly and require harsh environments and processes. Here, we report a novel method to prepare MoS<sub>2</sub> layered structures via self-assembly of a block copolymer system. The microphase separation of a polystyrene-*block*-poly (4-vinylpyridine) (PS-*b*-P4VP) block copolymer was carried out under tetrahydrofuran (THF) atmosphere at 50 °C to generate line-space patterns. Non-stoichiometric molybdenum oxide thin films were then successfully prepared by a UV/Ozone treatment following spin coating of molybdenum (V) chloride on to the phase separated structure. The molybdenum oxide structures obtained were characterized by X-ray photoelectron spectroscopy (XPS) and the surface morphology examined by atomic force microscopy (AFM) and scanning electron microscopy (SEM). A layered MoS<sub>2</sub> structure was then prepared by thermal evaporation of sulphur over the as-prepared MoO<sub>3</sub> thin films. The formation of the layered MoS<sub>2</sub> was confirmed by XPS, Raman spectroscopy and high resolution transmission electron microscopy (TEM).

### 5.2 Introduction

The transition-metal dichalcogenide semiconductor, molybdenum disulphide (MoS<sub>2</sub>), has recently emerged as a promising two-dimensional (2D) layered material and has attracted great

interest because of its distinctive electronic, optical, and catalytic properties, as well as its importance for dry lubrication.<sup>1-17</sup> An indirect-gap semiconductor, the bulk MoS<sub>2</sub> crystal, is built-up of van der Waals bonded S-Mo-S units and has a band gap of 1.29 eV and 1.90 eV for the bulk material and single layers, respectively.<sup>18</sup> MoS<sub>2</sub> field-effect transistors (FETs) have shown significant potential for fabrication of 2D electronic devices.<sup>19-27</sup> However, all the MoS<sub>2</sub> field-effect transistors (FETs) reported to date are fabricated using electron beam- or photolithography on top of MoS<sub>2</sub> flakes dispersed on substrates<sup>28-38</sup> and/or polymer-assisted transfer of MoS<sub>2</sub> sheets followed by dissolving the effective adhesive used.<sup>35</sup> Both these processes involve multiple wet processing steps and the 2D structure formed are in direct contact with various wet chemicals which may contaminate or even degrade the MoS<sub>2</sub> surface. Different morphologies of MoS<sub>2</sub> can be synthesized by different methods such as solvothermal, hydrothermal, high pressure-arc discharge and various chemical transport reactions. Generally, the 2D materials are prepared by a two-step process: the synthesis of the layered bulk material which is followed by an exfoliation process.<sup>39-41</sup> Liu et al. performed a modified vacuum assisted impregnation route to synthesize highly ordered mesoporous MoS<sub>2</sub>.<sup>42</sup> Ding et al. have obtained hierarchical MoS<sub>2</sub> microspheres via a facile PS microsphere-assisted hydrothermal method.<sup>43</sup> Surfactant assisted synthesis was also reported to improve the electrochemical performances. Liang et al. have reported the synthesis of MoS<sub>2</sub> nanosheets by an efficient and scalable PVP-assisted hydrothermal reaction.<sup>44</sup> There are a few well-known vapour phased synthesis methods involving the chemical reaction of sulfur and molybdenum compounds such the thermal decomposition of ammonium thiomolybdate precursors in presence of hazardous gases like hydrogen sulphide (H<sub>2</sub>S) and carbon disulphide(CS<sub>2</sub>).<sup>45-47</sup>

The microphase separation of block copolymer (BCP) thin films can provide an alternative to conventional top-down lithographic methods. The BCP nanopatterns can be integrated into fabrication by removing one block of polymer and then using the remaining block of polymer

as an etch mask for pattern transfer into the substrate.<sup>48-50</sup> Different materials including various metal oxides, dielectric materials and metals have been combined with the BCP and used to create a hard mask to overcome the poor etch selectivity and shape control.<sup>51-55</sup>

In this study, we systematically demonstrate the fabrication of nanowires of layered MoS<sub>2</sub> by an alternative to conventional photolithographic processing, i.e. self-assembly of block copolymers followed by selective insertion of a Mo salt into the P4VP block and oxidation to form the metal trioxide. The MoS<sub>2</sub> nanowires were prepared with simple sulfurization of the molybdenum oxide (MoO<sub>3</sub>). This method not only obviates the excessive use of wet chemistry steps, but also generates nanodimensioned wire-like patterns of 2D MoS<sub>2</sub> nanowires.

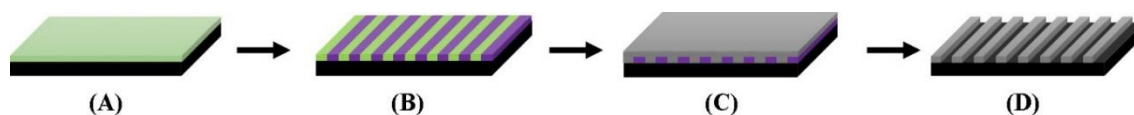
### 5.3 Experimental:

#### 5.3.1 Materials

For this study, highly polished single-crystal silicon <100> wafers (p-type) with a native oxide layer of 2 nm were used. Two different molecular weight polystyrene-*block*-poly(4-vinylpyridine) (PS-*b*-P4VP) were purchased from Polymer Source, Inc., Canada, with a molecular weight of 37 kg mol<sup>-1</sup> ( $M_{nPS} = 20$  kg mol<sup>-1</sup>,  $M_{nP4VP} = 17$  kg mol<sup>-1</sup>,  $f_{PS} = 0.54$ ), with a polydispersity ( $M_w/M_n$ ) of 1.08 and  $M_n = 18.2$  kg mol<sup>-1</sup> ( $M_{nPS} = 9$  kg mol<sup>-1</sup>,  $M_{nP4VP} = 9.2$  kg mol<sup>-1</sup>,  $f_{PS} = 0.49$ ), with a polydispersity ( $M_w/M_n$ ) of 1.09 (where,  $M_n$  and  $M_w$  are number average and weight average molecular weights). The block copolymer was used without further purification. Molybdenum (V) chloride (MoCl<sub>5</sub>), toluene (99.8%, anhydrous), tetrahydrofuran (THF) (99.8%, anhydrous), ethanol (dehydrated) were purchased from Sigma-Aldrich and used without further purification.

### 5.3.2 MoS<sub>2</sub> nanowire formation

Scheme 5.1 shows the overall methodology of producing molybdenum oxide nanowires. In order to use this methodology a well-defined microphase separated BCP nanopattern has to be formed. Briefly, the BCP was spin coated onto a silicon wafer (A) and then phase separation was achieved by solvent vapor annealing (SVA) (B). The molybdenum precursor solution was then spin coated onto the phase separated BCP film (C). Finally, UV/Ozone treatment was carried out for a 3h period which led to the formation of regular structure of MoO<sub>x</sub>.



**Scheme 5.1.** Schematic of the formation of the MoO<sub>x</sub> nanowires. (A) PS-*b*-P4VP BCP spin coated on silicon wafer, (B) phase separated BCP thin film after solvent annealing, (C) loading of molybdenum precursor on/in the P4VP domains by spin coating and (D) fabrication of MoO<sub>x</sub> nanowires by UV/Ozone treatment.

In detail, the polymer was first dissolved in a mixture of toluene and THF (80:20) to yield 0.5 wt% solution stirred for several hours to ensure complete dissolution prior to coating. BCP thin films were prepared by spin coating the polymer solution onto the substrates at 3000 rpm for 30 s. The thin films prepared were exposed to a saturated THF environment at 50 °C for six hours. This solvent annealing procedure was carried out in 100 mL glass jar containing 10 mL of THF solvent in small vial. After six hours, samples were removed and trapped solvent allowed to evaporate under ambient conditions. Following this, a molybdenum (V) chloride solution of 0.5 wt% was prepared in ethanol and spin coated onto the phase separated film at 3000 rpm for 30 s. UV/Ozone treatment was used to oxidize the precursor and remove the polymer. A UV/Ozone system (PSD Pro Series Digital UV Ozone system; Novascan Technologies, Inc., USA) was used to treat the sample in this way. This equipment has a UV

source consisting of two low pressure mercury vapour grid lamps. Both lamps have an output current of 0.8-0.95 A and power of 65-100 W and have strong emissions at both wavelengths of UV radiation (184.9 nm and 253.7 nm). This system produces highly reactive ozone gas from oxygen that is present within the chamber. Samples were exposed for 3 h to ensure complete oxidization of the inorganic precursor and removal of the polymer. The thermal stability of the nanowires was verified by placing the substrate in the furnace at 700 °C for 1 h.

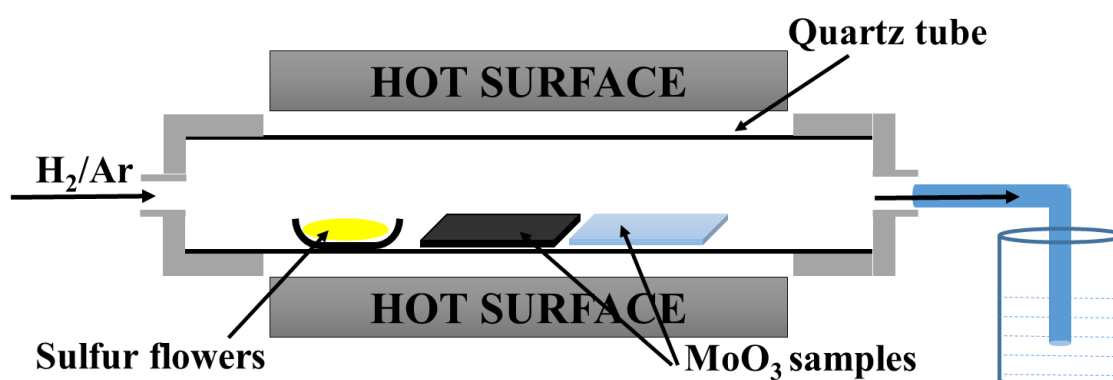


**Figure 5.1.** Experimental setup of the quartz tube in the centre of the furnace containing sulphur flowers and MoO<sub>3</sub> samples (see text for details).

Lee and co-workers have reported a method for synthesizing large-area MoS<sub>2</sub> monolayer flakes using the gas-phase reaction of MoO<sub>3</sub> and sulfur powders.<sup>56</sup> This was adapted here and MoO<sub>3</sub> wires prepared above were sulfurized using sulfur flowers at different temperatures and time (300 °C, 400 °C and 700 °C for 30 min, 20 min and 15 min respectively). The thermal evaporation of sulfur was affected in a horizontal quartz tube furnace as shown in Fig. 5.1. The samples were heated at heating rate of 15 °C min<sup>-1</sup> under a H<sub>2</sub>/Ar gas flow of 200 sccm. After sulfurization, the temperature ramped down at 15 °C min<sup>-1</sup> until room temperature was reached.

### 5.3.3 Characterization

BCP film thicknesses were measured by an optical ellipsometer (Woolam M2000). Surface morphologies were imaged by atomic force microscopy (SPM, Park systems, XE-100) in



tapping mode using silicon microcantilever probe tips with a force constant of 60000 Nm<sup>-1</sup> and a scanning force of 0.11 nN. Both topographic and phase images were recorded simultaneously. Scanning electron microscopy (SEM, FEI Helios NanoLab 600 Dual Beam FIB and Raith eLINE Plus) was also used to study the surface morphology. X-Ray photoelectron spectroscopy (XPS) experiments were conducted on a Vacuum Science Workshop CLASS100 high performance hemispherical analyser with Al K $\alpha$  (h $\nu$ =1486.6 eV) X-ray source operating at 72 W. Raman scattering spectroscopy was collected with a Renishaw inVia Raman spectrometer using a 514 nm 30mW Argon Ion laser and spectra were collected using a RenCam CCD camera. The beam was focused onto the samples using either a 20x or a 50x objective lens. Spectra were collected at a variety of exposure times and laser intensities. TEM cross-sections (lamellae) were prepared using a Helios Nanolab DB FIB. FIB samples were analysed by JEOL 2100 high resolution transmission electron microscope operating at an accelerating voltage of 200 kV.

## **5.4 Results and Discussion**

### **5.4.1 Self-assembly of PS-*b*-P4VP block copolymer**

As-cast PS<sub>20k</sub>-*b*-P4VP<sub>17k</sub> thin films are kinetically trapped in a micellar arrangement as can be clearly seen in Fig. 5.2(A). Thin films solvent annealed in a THF environment for 6 h at 50 °C generate vertically aligned lamellar nanostructures of pitch size (domain spacing) 37 nm, as shown in Fig. 5.2(B). The morphology and orientation of the films is dependent on careful choice of annealing solvent and conditions as discussed elsewhere.<sup>57, 58</sup> The thickness of the film was measured by ellipsometry and found out to be ~32 nm, close to the domain spacing.

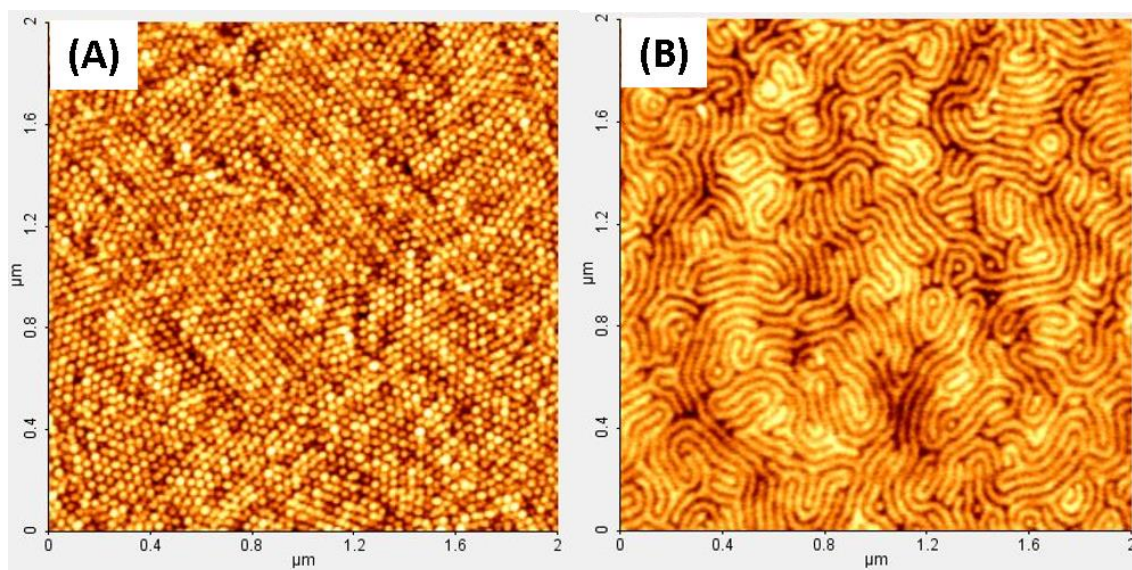


**Figure 5.2.** AFM topographic images of (A) as-cast and (B) phase separated PS-*b*-P4VP thin films after solvent annealing in THF for 6 h at 50 °C

#### 5.4.2 Molybdenum oxide nanowires fabrication by an inclusion technique

The BCP films can be used as templates to create ordered oxide nanowire arrays by the salt inclusion technique described above.<sup>59,60</sup> When ethanol was added to MoCl<sub>5</sub>, an emerald green solution was obtained, due to the formation of the dimer [MoCl<sub>3</sub>(OR)<sub>2</sub>]<sub>2</sub>.<sup>61</sup> To prevent overflow and non-selective salt deposition at the film surface of the BCP, a low concentration of precursor solution was required and a 0.5 wt.% MoCl<sub>5</sub> solution was found to be optimum for spin coating. Typical samples following UV/Ozone treatment for 3 h are shown in Fig. 5.3(A) (topographic AFM) and Fig. 5.3(B) SEM of the Mo oxide structures formed. The MoO<sub>x</sub> structure formed by inclusion was similar to that of the original BCP with a pitch size of 37 nm. The SEM magnified view of the surface Fig. 5.3(C) displays features with sharp edges and relatively smooth surfaces consistent with crystalline materials.

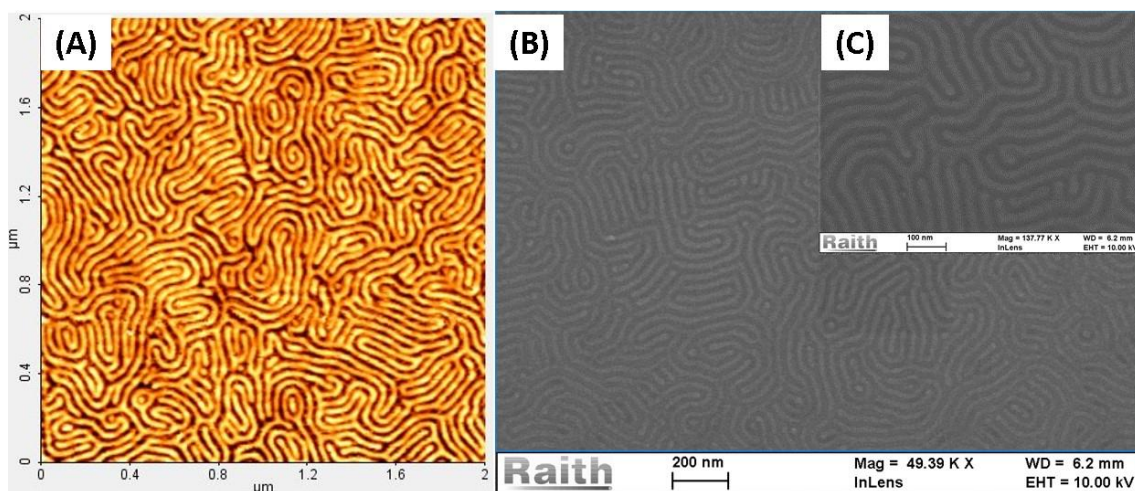


**Figure 5.3.** AFM topography image (A), top-down SEM image (B) and (C) is SEM image of same sample at higher magnification of molybdenum oxide nanowires obtained after UV/Ozone treatment of self-assembled PS<sub>20k</sub>-*b*-P4VP<sub>17k</sub> for 3 h.

#### 5.4.3 Determination of the MoO<sub>x</sub> stoichiometry by XPS

X-ray photoelectron spectroscopy (XPS) analysis of the Mo oxide nanowires prepared above was performed in order to determine the chemical composition of the samples. Since these are thin (see below) it is suggested this is an indication of the bulk composition of the wires. The XPS wide spectrum shows main features due to molybdenum and oxygen atoms and minor peaks of carbon and silicon (Fig. 5.4(A)). This survey scan shows no evidence of surface charging effects and no features due to impurities such as Cl could be seen. The carbon seen (C1s at 285.1 eV) is consistent with adventitious contamination. The appearance of Si 2s and Si 2p signals are attributed to the Si substrate used. The Mo 3d features (Fig. 5.4(B)) are typical of Mo in the 6+ oxidation state<sup>62-68</sup> with Mo 3d<sub>5/2</sub> and Mo 3d<sub>3/2</sub> at binding energies (BE) of 232.3 eV and 235.5 eV. As shown in Fig. 5.4(C), the two components associated with Mo 3p<sub>3/2</sub> and Mo 3p<sub>1/2</sub> spin orbit doublet at 398.2 eV and 415.6 eV BE respectively are also in agreement with the literature values.<sup>69</sup> Complete hydrolysis/oxidation of the Mo precursor solution was also confirmed as no chlorine can be detected on XPS. The O 1s peaks of the XPS spectra of the same films are shown in Fig. 5.4(D). Two resolved (using standard curve-fitting

procedures) O1s peaks at ~531 eV and 532.5 eV were observed and these can be interpreted as lattice oxygen (O<sup>2-</sup>) and surface hydroxyl/adsorbed water species respectively. Note that the O 1s signal at ~531 eV is quite broad possibly because of a contribution of a range of different lattice oxygen sites in the MoO<sub>3</sub> structure and also signal deriving from the passive oxide coated silicon substrate.

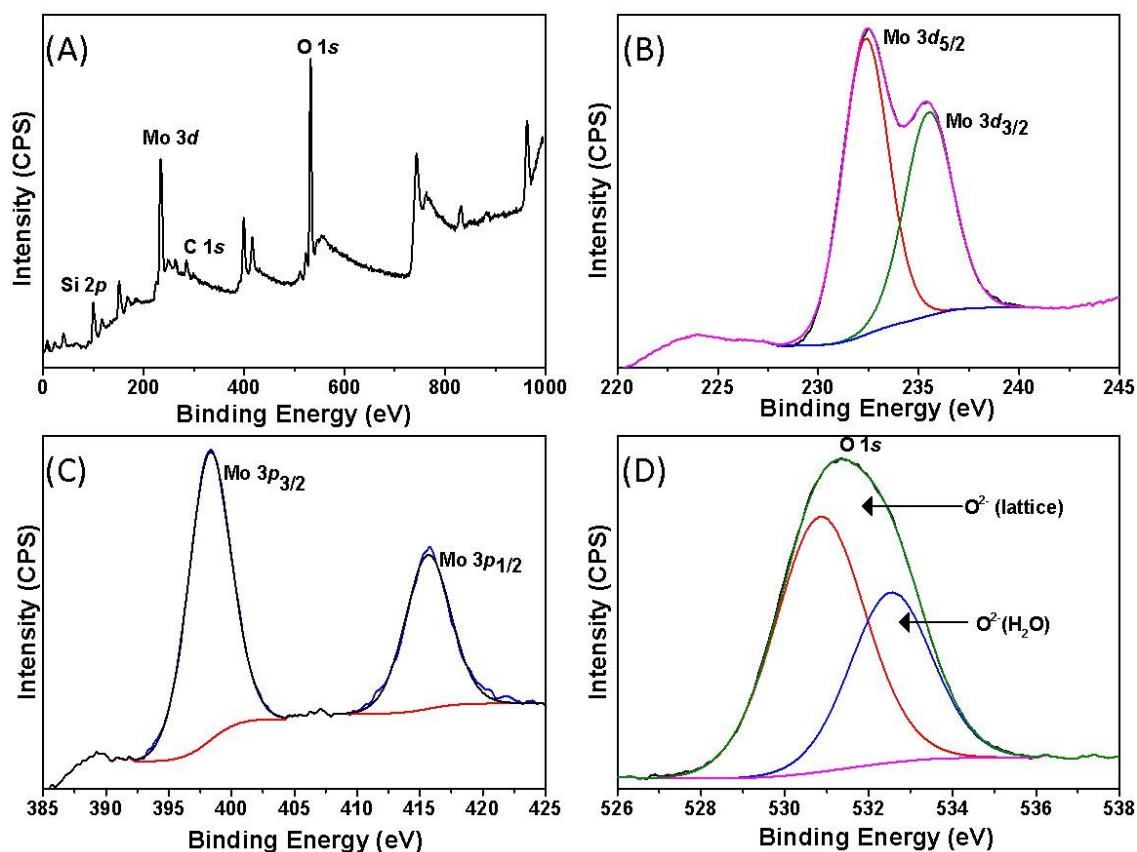


**Figure 5.4.** XPS spectra of (A) wide scan spectra (survey), (B) Mo 3d, (C) Mo 3p and (D) O 1s core level spectra of molybdenum oxide nanowires after UV/Ozone treatment.

#### 5.4.4 Sulfurization of MoO<sub>3</sub> nanowires

The previously fabricated MoO<sub>3</sub> nanowires on silicon substrates were subject to sulfur treatments for different temperature/times. These were temperatures and times of 300, 400 and 700 °C for 30, 20 and 15 min, conditions are fully described above. These conditions were varied to ensure that the MoO<sub>3</sub> nanowires could be fully converted to the sulfide derivatives. Fig. 5.5 shows typical SEM data from selected samples but in each case the contrast changes

(compared to the oxide only samples) are consistent with composition changes. At the lowest temperature of 300 °C the nanowires formed are not damaged or delaminated from the substrate and, hence, the structures remain intact (Fig. 5.5(A)). It is thought that in these conditions the MoO<sub>3</sub> is readily reduced to MoO<sub>2</sub> which is then readily converted to the sulfide. The higher magnification image (Fig. 5.5(B)) confirms the gross morphology of the nanopattern is not disturbed. Higher temperature processes appear to cause the degradation of the pattern with clear evidence of over-sulfurization as shown in Fig. 5.5(C) and (D). At 400 °C (Fig. 5.5(C)) the SEM image appears to be similar to the image of the MoS<sub>2</sub> formed at 300 °C but the structure is not uniform and in several areas the wires coalesce. After reaction at 700 °C (Fig. 5.5(D)), obvious degradation has occurred. Much of the nanowire pattern is lost and evidence of the nucleation of particulate is observed. This suggests that a nucleation and growth mechanism for MoS<sub>2</sub> through surface diffusion exists at higher temperature.

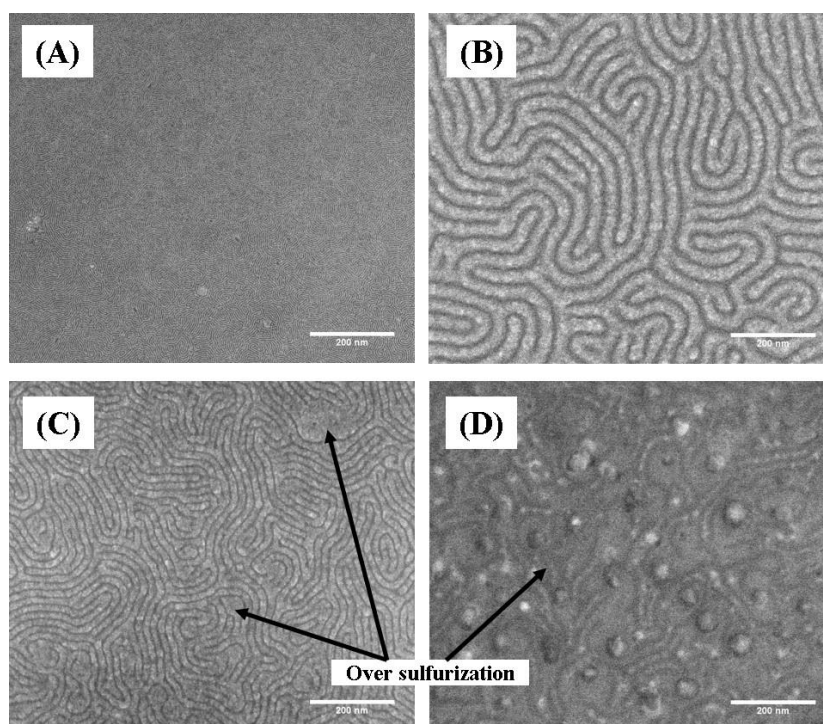


**Figure 5.5.** Scanning electron micrographs of MoS<sub>2</sub> nanowires formed after sulfurization of MoO<sub>3</sub> nanowires by thermal evaporation of sulfur powders at: (A-B) 300 °C for 30 min, (C) 400 °C for 20 min and (D) 700 °C for 15 min.

For all three samples, as shown in Fig. 5.6, XPS analysis was carried out to study the chemical composition and the surface electronic states of MoS<sub>2</sub>. The XPS survey spectrum (Fig. 5.6A) indicates the presence of Mo, S, C and O elements. In Fig. 5.6(B) and 5.6(C), high-resolution XPS spectra of Mo 3*d* and S 2*p* are shown, respectively. The Mo 3*d* spectra displays peaks around 229.7 and 232.7 eV (Mo3*d*<sub>5/2</sub> and Mo3*d*<sub>3/2</sub> respectively) and these are similar to features typical of Mo<sup>4+</sup> states in MoS<sub>2</sub>.<sup>70</sup> The smaller peak visible (Fig. 5.6(B)) at 226.4 eV is identified as the S2*s* feature. The S2*p* photoelectron spectrum is shown in Fig. 5.6(C) and shows a broad single peak at 162.5 eV due to overlapping S2*p*<sup>3/2</sup> and 2*p*<sup>1/2</sup> peaks of S<sup>2-</sup> in MoS<sub>2</sub>.<sup>71, 72</sup> Raman spectroscopy was carried out to analyse the structure and it further confirmed the MoS<sub>2</sub> structure with the appearance of two distinct peaks at 381 cm<sup>-1</sup> and 405 cm<sup>-1</sup>. These are consistent with the E<sup>1</sup><sub>2g</sub> vibrational Mo-S bond along the base plane and the A<sub>1g</sub> vibration of sulphur along the vertical axis, respectively.<sup>73</sup> At 300 °C, a small shoulder peak was observed at about 460 cm<sup>-1</sup> due to the presence of MoO<sub>2</sub>.<sup>74</sup> This suggests incomplete sulfurization at the lower temperatures used. With increasing temperature the Raman features remained narrow and are consistent with the presence of highly ordered layered structures. The peak difference between A<sub>1g</sub> and E<sub>2g</sub> modes (24 cm<sup>-1</sup>) can be used to identify the number of layers of MoS<sub>2</sub> and this indicates 4-5 layers.<sup>73, 75</sup>

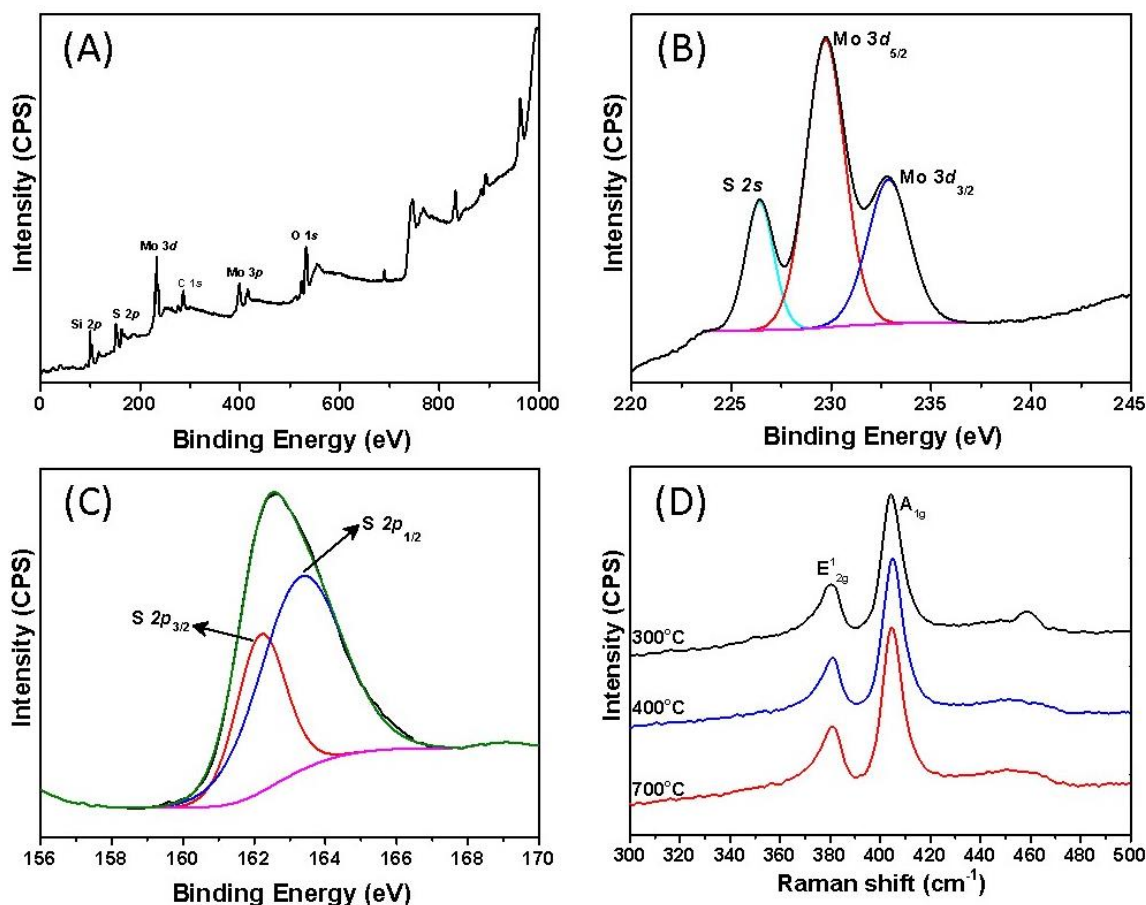


**Figure 5.6.** MoS<sub>2</sub> nanopatterns analyzed by XPS and Raman spectroscopy. (A) XPS survey spectrum of the MoS<sub>2</sub> prepared at 300 °C. High resolution XPS spectra of (B) Mo 3d and S 2s; and (C) S 2p. (D) Raman spectrum of MoS<sub>2</sub> nanowires formed after sulfurization at 300 °C, 400 °C and 700 °C showing the E<sup>1</sup><sub>2g</sub> and A<sub>1g</sub> vibrational modes

The value of the MoS<sub>2</sub> thickness calculated by the Raman method can be compared to that calculated by AFM. Fig. 5.7 shows the multilayer MoO<sub>3</sub> and MoS<sub>2</sub> nanowires and their height profiles by AFM. An analysis of the data in Fig. 5.7 shows that the distance between the MoO<sub>3</sub> and MoS<sub>2</sub> nanowires (pitch) is 38 nm consistent with the original BCP structure. However the measured thicknesses for the oxide is 3.8 nm and 3.5 nm for the sulfide MoS<sub>2</sub>. The monolayer thickness of S-Mo-S structures in bulk MoS<sub>2</sub> have a thickness of 0.6 nm.<sup>76, 77</sup> This suggest a shade of around 6 MoS<sub>2</sub> layers in reasonable agreement with the Raman measured value.

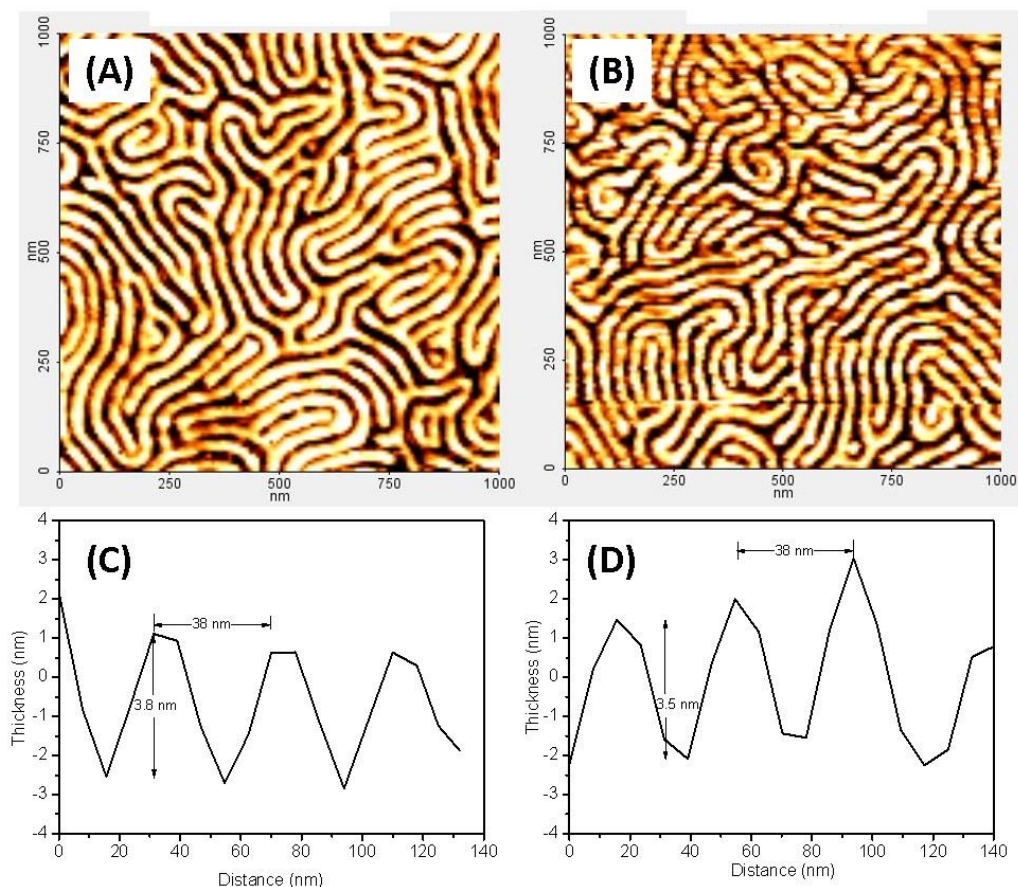


**Figure 5.7.** (A) and (B) are the topographic AFM images of MoO<sub>3</sub> and MoS<sub>2</sub> nanowires, (C) and (D) are the height profiles of (A) and (B) respectively.

The final morphology of the multilayer MoS<sub>2</sub> formed by sulfurization at 300 °C for 30 min was studied by TEM FIB cross section and a typical image is shown in Fig. 5.8. It can be seen immediately that the top-down nanowire pattern extends through to the substrate (Fig. 5.8(A)). The nanowire structures seem to be somewhat different than might be expected from ideal rectangular cross-sections. The nanowires show a rounded shape and indications of spreading at the base or even the formation of a surface layer of MoS<sub>2</sub>. However, the latter seems less likely as in several areas distinct gaps are seen between the wire bases. The observation of broadening be expected as the high temperature sulfurization did indicate diffusion occurs. Further, the melting point of MoO<sub>3</sub> is relatively low at less than 800 °C.<sup>78</sup> In Fig. 5.8(B), indicative high resolution TEM cross-section data confirm that the MoS<sub>2</sub> nanowires have a



well-defined layer structure although the structure is clearly polycrystalline in nature and not preferentially orientated with reference to the surface plane. There are clearly a few layers of MoS<sub>2</sub> on top of the SiO<sub>2</sub>/Si substrates is shown and the average height of these is 6 to 8 nm or 10-12 layers. This is somewhat higher than the value seen by AFM but this may be related to tip issues in small dimensioned topography as well as the averaging nature of Raman which will provide an average thickness across the nanowire width. As shown in Figure 5.8(C), the high angle annular dark-field scanning transmission electron microscopy (HAADF-STEM) image indicates the presence of MoS<sub>2</sub> nanowires on Si-substrate. To confirm the presence of MoS<sub>2</sub> nanowire after the sulfurization, energy dispersive X-ray (EDX) mapping was performed to reveal presence of S (yellow) and Mo (green).

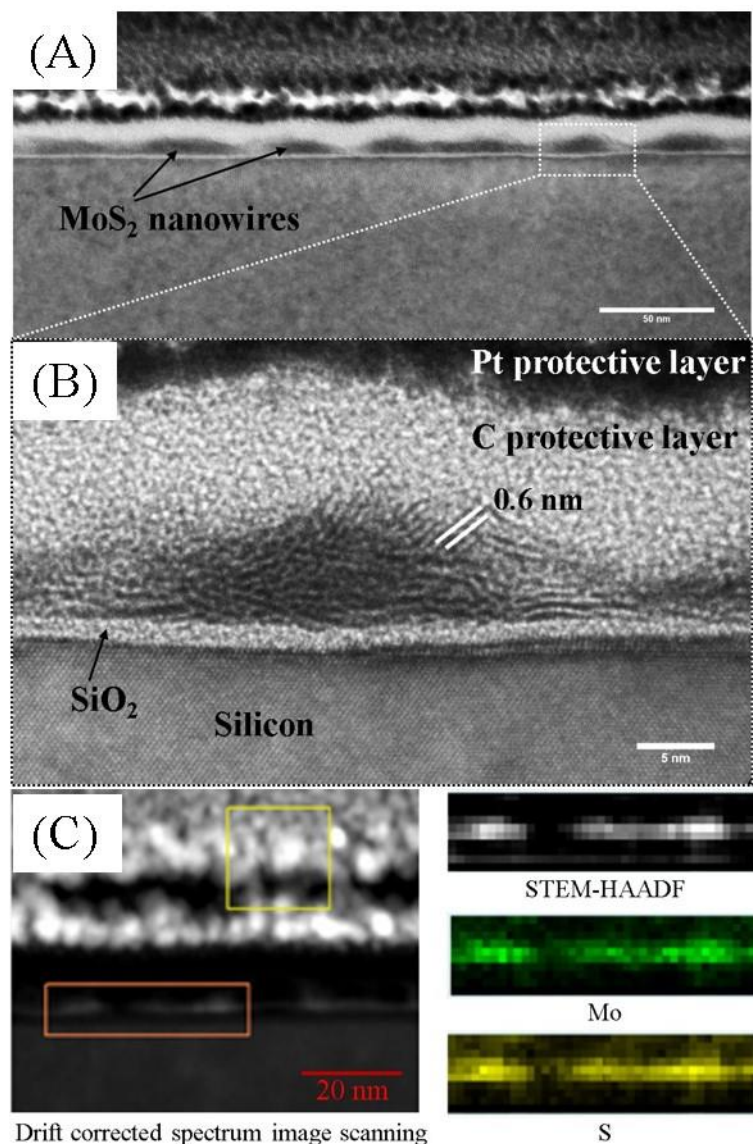


**Figure 5.8.** (A) TEM images of MoS<sub>2</sub> nanowires. (B) Enlarged HR-TEM image of the marked area in (A). (C) EDX mapping of MoS<sub>2</sub> nanowire revealing presence of S and Mo.

This form of BCP nanofabrication is extremely versatile and can be used to create nanopatterns of different dimensions by tuning the molecular weight of the polymer. In order to verify that the methodology could be extended to lower molecular weight systems and, hence, smaller feature size, a further set of the experiments were performed using the lower molecular weight PS<sub>9k</sub>-*b*-P4VP<sub>9.2k</sub> with total molecular weight of 18.2 kg mol<sup>-1</sup>. Fig. 5.9(A) illustrates the lamellar structure formed after solvent annealing the PS<sub>9k</sub>-*b*-P4VP<sub>9.2k</sub> at 50 °C for 6 h in a THF atmosphere. The long range well-defined and ordered lamellar morphology of the BCP over

several micrometres can be readily seen in the image and a domain (pitch) size of 23 nm was measured. Fig. 5.9 (B and C) provides a view of the derived MoO<sub>3</sub> and MoS<sub>2</sub> (300 °C sulfurization) nanopatterns formed after a similar experimental procedure to that described above. As for the higher molecular weight BCP, the oxide and sulfide nanowires have similar morphology to the templating microphase separated BCP structure and indicate the robust nature of the fabrication process used. Interestingly, nucleation of sulfide nanoparticles is seen at this lower temperature in contrast to the higher molecular weight structure where sulfurization did not produce aggregates until higher temperatures. This is consistent with a mass-transport limited growth or sintering process since these limitations are reduced for the smaller, more densely packed nanofeatures produced by lower molecular weight BCPs.

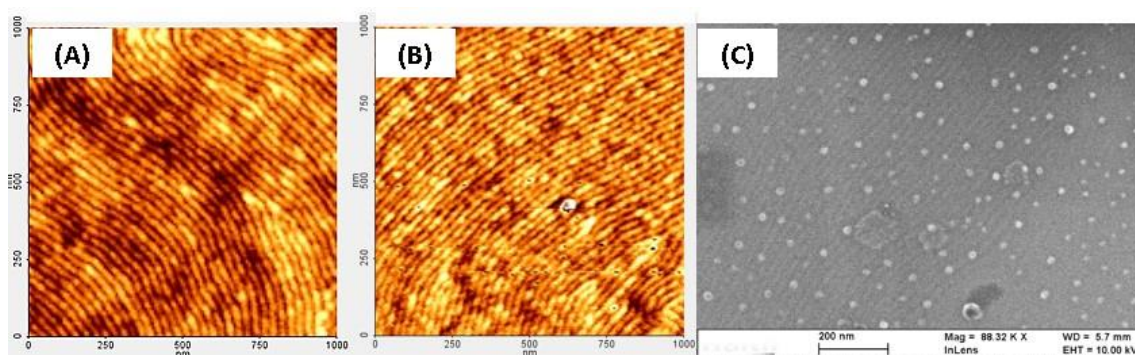


**Figure 5.9.** (A) is the AFM topography images of PS<sub>9k</sub>-b-P4VP<sub>9.2k</sub> after solvent annealing in THF for 6 h at 50 °C, (B) is the topographic AFM image of the MoO<sub>3</sub> nanowires obtained after UV/Ozone treatment of sample shown in (A), and (C) is SEM image of the MoS<sub>2</sub> nanowires obtained after sulfurization at 300 °C.

### 5.5. Conclusions:

The self-assembly of block copolymers has already received attention as an alternative method to the current UV-lithographic process for producing Si nanowires but the use of the methodology outlined here could be adapted to allow the direct formation of a range of nanowire materials. There are real challenges in developing methods for the fabrication of

nanometre dimensioned patterns of 2D materials such as low-band gap MoS<sub>2</sub> where etching and selective chemistries can either alter the stoichiometry or easily prepared materials such as flakes are difficult to integrate into large scale production. In this article we propose a two-step process to synthesize large-area and polycrystalline MoS<sub>2</sub> nanowire thin layers. The self-assembly of PS-*b*-P4VP block copolymers have been shown to be a convenient and readily processable method for the preparation of MoS<sub>2</sub> nanowires of thicknesses equivalent to a few layers of MoS<sub>2</sub>. The structures obtained here are free of chlorine after oxidation by UV/Ozone treatment as confirmed by XPS despite the use of a chloride salt precursor. Large-area MoS<sub>2</sub> films were the directly synthesized on SiO<sub>2</sub>/Si substrates by sulfurization of the patterned MoO<sub>3</sub> thin film formed by an insertion and oxidation process. The obtained structures were characterized and confirmed as MoS<sub>2</sub> layered systems by a range of techniques such as AFM, XPS, Raman, SEM and TEM.

The sulfurization strategy used here was performed at relatively low temperatures, however, elevated temperatures resulted in agglomeration and growth of 3D particles. Even at the lowest temperatures, the mass transport and diffusion led to broadening of the wire bases as evidenced by high resolution, cross-section TEM. This may be associated with the low melting point of MoO<sub>3</sub>. Thus, in order to produce nanowires as electronic circuitry, careful optimization of the sulfurization route will be required. However, the techniques outlined here may provide a breakthrough in the fabrication of patterned structures of complex materials.

## 5.6. References

1. Optical and Electrical Properties, in *Physics and chemistry of materials with layered structures*, Lee, P. A., Ed. Springer Netherlands: **1976**; Vol. 4, pp VIII, 464.
2. Bromley, R. A.; Murray, R. B.; Yoffe, A. D., The band structures of some transition metal dichalcogenides. III. Group VIA: trigonal prism materials. *Journal of Physics C: Solid State Physics* **1972**, 5 (7), 759.
3. Kasowski, R. V., Band Structure of MoS<sub>2</sub> and NbS<sub>2</sub>. *Physical Review Letters* **1973**, 30 (23), 1175-1178.
4. Mattheiss, L. F., Energy Bands for 2H-NbSe<sub>2</sub> and 2H-MoS<sub>2</sub>. *Physical Review Letters* **1973**, 30 (17), 784-787.
5. Mattheiss, L. F., Band Structures of Transition-Metal-Dichalcogenide Layer Compounds. *Physical Review B* **1973**, 8 (8), 3719-3740.
6. Coehoorn, R.; Haas, C.; de Groot, R. A., Electronic structure of MoSe<sub>2</sub>, MoS<sub>2</sub>, and WSe<sub>2</sub>. II. The nature of the optical band gaps. *Physical Review B* **1987**, 35 (12), 6203-6206.
7. Coehoorn, R.; Haas, C.; Dijkstra, J.; Flipse, C. J. F.; de Groot, R. A.; Wold, A., Electronic structure of MoSe<sub>2</sub>, MoS<sub>2</sub>, and WSe<sub>2</sub>. I. Band-structure calculations and photoelectron spectroscopy. *Physical Review B* **1987**, 35 (12), 6195-6202.
8. Beal, A. R.; Hughes, H. P., Kramers-Kronig analysis of the reflectivity spectra of 2H-MoS<sub>2</sub>, 2H-MoSe<sub>2</sub> and 2H-MoTe<sub>2</sub>. *Journal of Physics C: Solid State Physics* **1979**, 12 (5), 881.
9. Beal, A. R.; Knights, J. C.; Liang, W. Y., Transmission spectra of some transition metal dichalcogenides. II. Group VIA: trigonal prismatic coordination. *Journal of Physics C: Solid State Physics* **1972**, 5 (24), 3540.

10. Böker, T.; Severin, R.; Müller, A.; Janowitz, C.; Manzke, R.; Voß, D.; Krüger, P.; Mazur, A.; Pollmann, J., Band structure of MoS<sub>2</sub>, MoSe<sub>2</sub>, and  $\alpha$ -MoTe<sub>2</sub>: Angle-resolved photoelectron spectroscopy and ab initio calculations. *Physical Review B* **2001**, 64 (23), 235305.
11. Evans, B. L.; Young, P. A., Optical Absorption and Dispersion in Molybdenum Disulphide. *Proceedings of the Royal Society of London A: Mathematical, Physical and Engineering Sciences* **1965**, 284 (1398), 402-422.
12. Evans, B. L.; Young, P. A., Exciton spectra in thin crystals: the diamagnetic effect. *Proceedings of the Physical Society* **1967**, 91 (2), 475.
13. Kam, K. K.; Parkinson, B. A., Detailed photocurrent spectroscopy of the semiconducting group VIB transition metal dichalcogenides. *The Journal of Physical Chemistry* **1982**, 86 (4), 463-467.
14. Li, T.; Galli, G., Electronic Properties of MoS<sub>2</sub> Nanoparticles. *The Journal of Physical Chemistry C* **2007**, 111 (44), 16192-16196.
15. McMenamin, J. C.; Spicer, W. E., Photoemission studies of layered transition-metal dichalcogenides: MoS<sub>2</sub>. *Physical Review B* **1977**, 16 (12), 5474-5487.
16. Wilson, J. A.; Yoffe, A. D., The transition metal dichalcogenides discussion and interpretation of the observed optical, electrical and structural properties. *Advances in Physics* **1969**, 18 (73), 193-335.
17. Zong, X.; Yan, H.; Wu, G.; Ma, G.; Wen, F.; Wang, L.; Li, C., Enhancement of Photocatalytic H<sub>2</sub> Evolution on CdS by Loading MoS<sub>2</sub> as Cocatalyst under Visible Light Irradiation. *Journal of the American Chemical Society* **2008**, 130 (23), 7176-7177.
18. Mak, K. F.; Lee, C.; Hone, J.; Shan, J.; Heinz, T. F., Atomically Thin MoS<sub>2</sub>: A New Direct-Gap Semiconductor. *Physical Review Letters* **2010**, 105 (13), 136805.

19. Baugher, B. W. H.; Churchill, H. O. H.; Yang, Y.; Jarillo-Herrero, P., Intrinsic Electronic Transport Properties of High-Quality Monolayer and Bilayer MoS<sub>2</sub>. *Nano Letters* **2013**, 13 (9), 4212-4216.
20. Fang, H.; Tosun, M.; Seol, G.; Chang, T. C.; Takei, K.; Guo, J.; Javey, A., Degenerate n-Doping of Few-Layer Transition Metal Dichalcogenides by Potassium. *Nano Letters* **2013**, 13 (5), 1991-1995.
21. Fu, D.; Zhou, J.; Tongay, S.; Liu, K.; Fan, W.; King Liu, T.-J.; Wu, J., Mechanically modulated tunneling resistance in monolayer MoS<sub>2</sub>. *Applied Physics Letters* **2013**, 103 (18), 183105.
22. Liu, H.; Si, M.; Deng, Y.; Neal, A. T.; Du, Y.; Najmaei, S.; Ajayan, P. M.; Lou, J.; Ye, P. D., Switching Mechanism in Single-Layer Molybdenum Disulfide Transistors: An Insight into Current Flow across Schottky Barriers. *ACS Nano* **2014**, 8 (1), 1031-1038.
23. Radisavljevic, B.; Kis, A., Mobility engineering and a metal–insulator transition in monolayer MoS<sub>2</sub>. *Nat Mater* **2013**, 12 (9), 815-820.
24. Radisavljevic, B.; Whitwick, M. B.; Kis, A., Integrated Circuits and Logic Operations Based on Single-Layer MoS<sub>2</sub>. *ACS Nano* **2011**, 5 (12), 9934-9938.
25. Radisavljevic B; Radenovic A; Brivio J; Giacometti V; Kis A, Single-layer MoS<sub>2</sub> transistors. *Nat Nano* **2011**, 6 (3), 147-150.
26. Wang, H.; Yu, L.; Lee, Y.; Fang, W.; Hsu, A.; Herring, P.; Chin, M.; Dubey, M.; Li, L.; Kong, J.; Palacios, T. In Large-scale 2D electronics based on single-layer MoS<sub>2</sub> grown by chemical vapor deposition, *Electron Devices Meeting (IEDM), 2012 IEEE International*, 10-13 Dec. 2012; **2012**; pp 4.6.1-4.6.4.

27. Wang, H.; Yu, L.; Lee, Y.-H.; Shi, Y.; Hsu, A.; Chin, M. L.; Li, L.-J.; Dubey, M.; Kong, J.; Palacios, T., Integrated Circuits Based on Bilayer MoS<sub>2</sub> Transistors. *Nano Letters* **2012**, 12 (9), 4674-4680.
28. Bao, W.; Cai, X.; Kim, D.; Sridhara, K.; Fuhrer, M. S., High mobility ambipolar MoS<sub>2</sub> field-effect transistors: Substrate and dielectric effects. *Applied Physics Letters* **2013**, 102 (4), 042104.
29. Chang, H.-Y.; Yang, S.; Lee, J.; Tao, L.; Hwang, W.-S.; Jena, D.; Lu, N.; Akinwande, D., High-Performance, Highly Bendable MoS<sub>2</sub> Transistors with High-K Dielectrics for Flexible Low-Power Systems. *ACS Nano* **2013**, 7 (6), 5446-5452.
30. Das, S.; Appenzeller, J., Screening and interlayer coupling in multilayer MoS<sub>2</sub>. *physica status solidi (RRL) – Rapid Research Letters* **2013**, 7 (4), 268-273.
31. Das, S.; Chen, H.-Y.; Penumatcha, A. V.; Appenzeller, J., High Performance Multilayer MoS<sub>2</sub> Transistors with Scandium Contacts. *Nano Letters* **2013**, 13 (1), 100-105.
32. Jongho, L.; Hsiao-Yu, C.; Tae-Jun, H.; Huifeng, L.; Ruoff, R. S.; Dodabalapur, A.; Akinwande, D. In High-performance flexible nanoelectronics: 2D atomic channel materials for low-power digital and high-frequency analog devices, *Electron Devices Meeting (IEDM), 2013 IEEE International*, 9-11 Dec. 2013; **2013**; pp 19.2.1-19.2.4.
33. Kim, S.; Konar, A.; Hwang, W.-S.; Lee, J. H.; Lee, J.; Yang, J.; Jung, C.; Kim, H.; Yoo, J.-B.; Choi, J.-Y.; Jin, Y. W.; Lee, S. Y.; Jena, D.; Choi, W.; Kim, K., High-mobility and low-power thin-film transistors based on multilayer MoS<sub>2</sub> crystals. *Nat Commun* **2012**, 3, 1011.
34. Late, D. J.; Huang, Y.-K.; Liu, B.; Acharya, J.; Shirodkar, S. N.; Luo, J.; Yan, A.; Charles, D.; Waghmare, U. V.; Dravid, V. P.; Rao, C. N. R., Sensing Behavior of Atomically Thin-Layered MoS<sub>2</sub> Transistors. *ACS Nano* **2013**, 7 (6), 4879-4891.



35. Lee, G.-H.; Yu, Y.-J.; Cui, X.; Petrone, N.; Lee, C.-H.; Choi, M. S.; Lee, D.-Y.; Lee, C.; Yoo, W. J.; Watanabe, K.; Taniguchi, T.; Nuckolls, C.; Kim, P.; Hone, J., Flexible and Transparent MoS<sub>2</sub> Field-Effect Transistors on Hexagonal Boron Nitride-Graphene Heterostructures. *ACS Nano* **2013**, 7 (9), 7931-7936.
36. Liu, H.; Neal, A. T.; Ye, P. D., Channel Length Scaling of MoS<sub>2</sub> MOSFETs. *ACS Nano* **2012**, 6 (10), 8563-8569.
37. Liu, H.; Ye, P. D., MoS<sub>2</sub> Dual-Gate MOSFET With Atomic-Layer-Deposited Al<sub>2</sub>O<sub>3</sub> as Top-Gate Dielectric. *Electron Device Letters, IEEE* **2012**, 33 (4), 546-548.
38. Nam, H.; Wi, S.; Rokni, H.; Chen, M.; Priessnitz, G.; Lu, W.; Liang, X., MoS<sub>2</sub> Transistors Fabricated via Plasma-Assisted Nanoprinting of Few-Layer MoS<sub>2</sub> Flakes into Large-Area Arrays. *ACS Nano* **2013**, 7 (7), 5870-5881.
39. Chhowalla, M.; Amaratunga, G. A. J., Thin films of fullerene-like MoS<sub>2</sub> nanoparticles with ultra-low friction and wear. *Nature* **2000**, 407 (6801), 164-167.
40. Duphil, D.; Bastide, S.; Levy-Clement, C., Chemical synthesis of molybdenum disulfide nanoparticles in an organic solution. *Journal of Materials Chemistry* **2002**, 12 (8), 2430-2432.
41. Virsek, M.; Krause, M.; Kolitsch, A.; Remškar, M., Raman characterization of MoS<sub>2</sub> microtube. *physica status solidi (b)* **2009**, 246 (11-12), 2782-2785.
42. Liu, H.; Su, D.; Zhou, R.; Sun, B.; Wang, G.; Qiao, S. Z., Highly Ordered Mesoporous MoS<sub>2</sub> with Expanded Spacing of the (002) Crystal Plane for Ultrafast Lithium Ion Storage. *Advanced Energy Materials* **2012**, 2 (8), 970-975.
43. Ding, S.; Zhang, D.; Chen, J. S.; Lou, X. W., Facile synthesis of hierarchical MoS<sub>2</sub> microspheres composed of few-layered nanosheets and their lithium storage properties. *Nanoscale* **2012**, 4 (1), 95-98.

44. Liang, S.; Zhou, J.; Liu, J.; Pan, A.; Tang, Y.; Chen, T.; Fang, G., PVP-assisted synthesis of MoS<sub>2</sub> nanosheets with improved lithium storage properties. *CrystEngComm* **2013**, 15 (25), 4998-5002.
45. Chen, X.; Wang, X.; Wang, Z.; Yu, W.; Qian, Y., Direct sulfidization synthesis of high-quality binary sulfides (WS<sub>2</sub>, MoS<sub>2</sub>, and V<sub>5</sub>S<sub>8</sub>) from the respective oxides. *Materials Chemistry and Physics* **2004**, 87 (2–3), 327-331.
46. Farag, H.; El-Hendawy, A.-N. A.; Sakanishi, K.; Kishida, M.; Mochida, I., Catalytic activity of synthesized nanosized molybdenum disulfide for the hydrodesulfurization of dibenzothiophene: Effect of H<sub>2</sub>S partial pressure. *Applied Catalysis B: Environmental* **2009**, 91 (1–2), 189-197.
47. Lieberzeit, P. A.; Afzal, A.; Rehman, A.; Dickert, F. L., Nanoparticles for detecting pollutants and degradation processes with mass-sensitive sensors. *Sensors and Actuators B: Chemical* **2007**, 127 (1), 132-136.
48. Farrell, R.; Fitzgerald, T.; Borah, D.; Holmes, J.; Morris, M., Chemical Interactions and Their Role in the Microphase Separation of Block Copolymer Thin Films. *International Journal of Molecular Sciences* **2009**, 10 (9), 3671.
49. Farrell, R. A.; Petkov, N.; Shaw, M. T.; Djara, V.; Holmes, J. D.; Morris, M. A., Monitoring PMMA Elimination by Reactive Ion Etching from a Lamellar PS-*b*-PMMA Thin Film by ex Situ TEM Methods. *Macromolecules* **2010**, 43 (20), 8651-8655.
50. Park, M.; Harrison, C.; Chaikin, P. M.; Register, R. A.; Adamson, D. H., Block Copolymer Lithography: Periodic Arrays of ~10<sup>11</sup> Holes in 1 Square Centimeter. *Science* **1997**, 276 (5317), 1401-1404.

51. Fang, Q.; Li, X.; Tuan, A. P.; Perumal, J.; Kim, D.-P., Direct pattern transfer using an inorganic polymer-derived silicate etch mask. *Journal of Materials Chemistry* **2011**, 21 (12), 4657-4662.
52. Ghoshal, T.; Senthamaraikannan, R.; Shaw, M. T.; Holmes, J. D.; Morris, M. A., "In situ" hard mask materials: a new methodology for creation of vertical silicon nanopillar and nanowire arrays. *Nanoscale* **2012**, 4 (24), 7743-7750.
53. Krishnamoorthy, S.; Manipaddy, K. K.; Yap, F. L., Wafer-Level Self-Organized Copolymer Templates for Nanolithography with Sub-50 nm Feature and Spatial Resolutions. *Advanced Functional Materials* **2011**, 21 (6), 1102-1112.
54. Lim, K.-m.; Gupta, S.; Ropp, C.; Waks, E., Development of metal etch mask by single layer lift-off for silicon nitride photonic crystals. *Microelectron. Eng.* **2011**, 88 (6), 994-998.
55. Rangelow, I. W., Dry etching-based silicon micro-machining for MEMS. *Vacuum* **2001**, 62 (2-3), 279-291.
56. Lee, Y.-H.; Zhang, X.-Q.; Zhang, W.; Chang, M.-T.; Lin, C.-T.; Chang, K.-D.; Yu, Y.-C.; Wang, J. T.-W.; Chang, C.-S.; Li, L.-J.; Lin, T.-W., Synthesis of Large-Area MoS<sub>2</sub> Atomic Layers with Chemical Vapor Deposition. *Advanced Materials* **2012**, 24 (17), 2320-2325.
57. Chaudhari, A.; Ghoshal, T.; Shaw, M. T.; Cummins, C.; Borah, D.; Holmes, J. D.; Morris, M. A. *Formation of sub-7 nm feature size PS-b-P4VP block copolymer structures by solvent vapour process*, **2014**; pp 905110-905110-10.
58. Chaudhari, A.; Ghoshal, T.; Shaw, M.T.; Cummins, C; Borah, D; Holmes, J.D.; Morris, M.A., The effect of solvent annealing conditions on the film morphologies of lamellar forming polystyrene-b-poly(4-vinylpyridine). *Applied Materials & Interfaces* **2015**. Submitted

59. Cummins, C.; Borah, D.; Rasappa, S.; Chaudhari, A.; Ghoshal, T.; O'Driscoll, B. M. D.; Carolan, P.; Petkov, N.; Holmes, J. D.; Morris, M. A., Self-assembly of polystyrene-block-poly(4-vinylpyridine) block copolymer on molecularly functionalized silicon substrates: fabrication of inorganic nanostructured etchmask for lithographic use. *Journal of Materials Chemistry C* **2013**, 1 (47), 7941-7951.
60. Ghoshal, T.; Senthamaraiannan, R.; Shaw, M. T.; Holmes, J. D.; Morris, M. A., Fabrication of Ordered, Large Scale, Horizontally-Aligned Si Nanowire Arrays Based on an In Situ Hard Mask Block Copolymer Approach. *Advanced Materials* **2014**, 26 (8), 1207-1216.
61. Bradley, D. C.; Multani, R. K.; Wardlaw, W., 936. Some chloride alkoxides of quadrivalent vanadium and quinquevalent molybdenum. *Journal of the Chemical Society (Resumed)* **1958**, (0), 4647-4651.
62. Fleisch, T. H.; Mains, G. J., An XPS study of the UV reduction and photochromism of MoO<sub>3</sub> and WO<sub>3</sub>. *The Journal of Chemical Physics* **1982**, 76 (2), 780-786.
63. Greiner, M. T.; Chai, L.; Helander, M. G.; Tang, W.-M.; Lu, Z.-H., Transition Metal Oxide Work Functions: The Influence of Cation Oxidation State and Oxygen Vacancies. *Advanced Functional Materials* **2012**, 22 (21), 4557-4568.
64. Greiner, M. T.; Helander, M. G.; Tang, W.-M.; Wang, Z.-B.; Qiu, J.; Lu, Z.-H., Universal energy-level alignment of molecules on metal oxides. *Nat Mater* **2012**, 11 (1), 76-81.
65. Gruenert, W.; Stakheev, A. Y.; Feldhaus, R.; Anders, K.; Shpiro, E. S.; Minachev, K. M., Analysis of molybdenum(3d) XPS spectra of supported molybdenum catalysts: an alternative approach. *The Journal of Physical Chemistry* **1991**, 95 (3), 1323-1328.

66. Katrib, A.; Benadda, A.; Sobczak, J. W.; Maire, G., XPS and catalytic properties of the bifunctional supported MoO<sub>2</sub>(Hx)ac on TiO<sub>2</sub> for the hydroisomerization reactions of hexanes and 1-hexene. *Applied Catalysis A: General* **2003**, 242 (1), 31-40.
67. Soultati, A.; Douvas, A. M.; Georgiadou, D. G.; Palilis, L. C.; Bein, T.; Feckl, J. M.; Gardelis, S.; Fakis, M.; Kennou, S.; Falaras, P.; Stergiopoulos, T.; Stathopoulos, N. A.; Davazoglou, D.; Argitis, P.; Vasilopoulou, M., Solution-Processed Hydrogen Molybdenum Bronzes as Highly Conductive Anode Interlayers in Efficient Organic Photovoltaics. *Advanced Energy Materials* **2014**, 4 (3), n/a-n/a.
68. Vasilopoulou, M.; Douvas, A. M.; Georgiadou, D. G.; Palilis, L. C.; Kennou, S.; Sygellou, L.; Soultati, A.; Kostis, I.; Papadimitropoulos, G.; Davazoglou, D.; Argitis, P., The Influence of Hydrogenation and Oxygen Vacancies on Molybdenum Oxides Work Function and Gap States for Application in Organic Optoelectronics. *Journal of the American Chemical Society* **2012**, 134 (39), 16178-16187.
69. Moulder, J. F.; Chastain, J., Handbook of x-ray photoelectron spectroscopy: a reference book of standard spectra for identification and interpretation of XPS data. Perkin-Elmer Corporation: Eden Prairie, Minnesota, **1992**.
70. da Silveira Firmiano, E. G.; Rabelo, A. C.; Dalmaschio, C. J.; Pinheiro, A. N.; Pereira, E. C.; Schreiner, W. H.; Leite, E. R., Supercapacitor Electrodes Obtained by Directly Bonding 2D MoS<sub>2</sub> on Reduced Graphene Oxide. *Advanced Energy Materials* **2014**, 4 (6), n/a-n/a.
71. Baker, M. A.; Gilmore, R.; Lenardi, C.; Gissler, W., XPS investigation of preferential sputtering of S from MoS<sub>2</sub> and determination of MoS<sub>x</sub> stoichiometry from Mo and S peak positions. *Applied Surface Science* **1999**, 150 (1-4), 255-262.

72. Daqiang Gao, M. S., Jinyun Li, Jing Zhang, Zhipeng Zhang, Zhaolong Yang, Desheng Xue, Ferromagnetism in freestanding MoS<sub>2</sub> nanosheets. *Nanoscale Research Letters* **2013**, 8 (129).
73. Li, H.; Zhang, Q.; Yap, C. C. R.; Tay, B. K.; Edwin, T. H. T.; Olivier, A.; Baillargeat, D., From Bulk to Monolayer MoS<sub>2</sub>: Evolution of Raman Scattering. *Advanced Functional Materials* **2012**, 22 (7), 1385-1390.
74. Geske, M.; Korup, O.; Horn, R., Resolving kinetics and dynamics of a catalytic reaction inside a fixed bed reactor by combined kinetic and spectroscopic profiling. *Catalysis Science & Technology* **2013**, 3 (1), 169-175.
75. Lee, C.; Yan, H.; Brus, L. E.; Heinz, T. F.; Hone, J.; Ryu, S., Anomalous Lattice Vibrations of Single- and Few-Layer MoS<sub>2</sub>. *ACS Nano* **2010**, 4 (5), 2695-2700.
76. Tributsch, H.; Bennett, J. C., Electrochemistry and photochemistry of MoS<sub>2</sub> layer crystals. I. *Journal of Electroanalytical Chemistry and Interfacial Electrochemistry* **1977**, 81 (1), 97-111.
77. Wieting, T. J.; Verble, J. L., Infrared and Raman Studies of Long-Wavelength Optical Phonons in Hexagonal MoS<sub>2</sub>. *Physical Review B* **1971**, 3 (12), 4286-4292.
78. Cosgrove, L. A.; Snyder, P. E., High Temperature Thermodynamic Properties of Molybdenum Trioxide<sup>1</sup>. *Journal of the American Chemical Society* **1953**, 75 (5), 1227-1228

# 6

## Conclusions and Future Work

---

This chapter presents a summary of the research presented in this dissertation and points out some future recommendations based on the work.

### 6.1. Summary of the Dissertation

Current photolithographic techniques have enabled tremendous advancements in the semiconductor industry thus enabling high throughput and economical mass production of integrated semiconductor devices with ultra-high density of transistors and commensurate computing power. The directed self-assembly of block copolymers (BCPs) could enable the long-term extension of Moore's law via the formation of patterns at 20 nm pitch length scales and below. The main objective of this dissertation was to fabricate ultra-small feature size lamellar structures by using high  $\chi$  ( $\chi$ ) BCPs. The most widely used BCP currently, poly(styrene)-*block*-poly(methylmethacrylate) (PS-*b*-PMMA), lacks the thermodynamic driving force necessary for phase separation at smallest length scales. Here we have concentrated our research on high  $\chi$  ( $\chi \sim 0.34$ ) BCP system, polystyrene-*block*-poly(4-vinylpyridine) (PS-*b*-P4VP). This thesis investigated solvent annealing technique and applications of BCP self-assembly, which is driven by the microphase-separation of two mutually incompatible blocks. The patterns formed using BCP can be easily transferred into different functional materials. In this thesis, various factors were studied to self-assemble the BCPs in well-ordered and long range ordered structures.

In Chapter 2, the effect of type of solvent and time on the microdomain orientation during solvent-annealing of BCP ultrathin films on silicon substrate was studied using two different higher molecular weight PS-*b*-P4VP diblock copolymer. For high- $\chi$  BCP systems, solvent

annealing is preferred over thermal annealing, which can provide better chain flexibility to form well-ordered BCP microdomains. As demonstrated in Fig. 6.1, when the solvent-annealing was performed in toluene vapour atmosphere, hexagonally packed micellar structures were observed. However, by introducing tetrahydrofuran (THF) vapours with toluene vapours into the annealing chamber, mixed orientation of lamellae and perpendicular cylinders to the substrate were observed by AFM. When the thin films were annealed in THF rich environment, long stripes were formed.

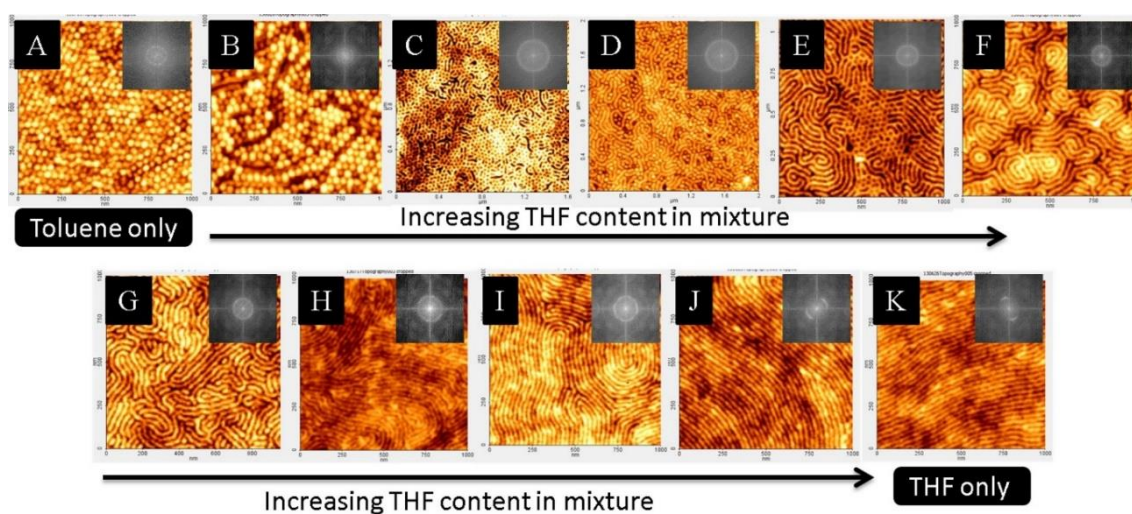


**Figure 6.1.** Topographic AFM images ( $1 \times 1 \mu\text{m}$ ) of  $\text{PS}_{9\text{k}}\text{-}b\text{-P4VP}_{9.2\text{k}}$  cast from toluene/THF (80/20) and solvent annealed at  $50^\circ\text{C}$  for 4h in different saturated solvent vapour environments of: (A) pure toluene, (B) toluene/THF =90/10, (C) toluene/THF =80/20, (D) toluene/THF =70/30, (E) toluene/THF =60/40, (F) toluene/THF =50/50, (G) toluene/THF =40/60, (H) toluene/THF =30/70, (I) toluene/THF =20/80, (J) toluene/THF =10/90 and (K) pure THF. All solvent compositions are given as (v/v). FFT patterns inset show the difference in the degree of order.

A systematic study of time effect on the morphology was undertaken. When the samples were annealed for short times, mixed morphologies of micelles and small stripes could be seen. By increasing the annealing time, high correlation length of lamellae was observed. Furthermore, it was investigated if various morphologies of BCPs, such as spheres, cylinders, and perforated lamellae, can be formed using solvent annealing technique. It was shown that the orientation and morphology of microdomains as well as the kinetics in  $\text{PS-}b\text{-P4VP}$  ultrathin films on solvent-annealing is significantly affected by the type of solvent.



In Chapter 3, lower molecular weight PS-*b*-P4VP BCPs were studied so as to achieve patterns of pitch size 10.3 nm (half-pitch ~6 nm) and different molecular weight PS-*b*-P4VP BCPs were also chosen to fabricate sub-7 nm features, as shown in Fig. 6.2.

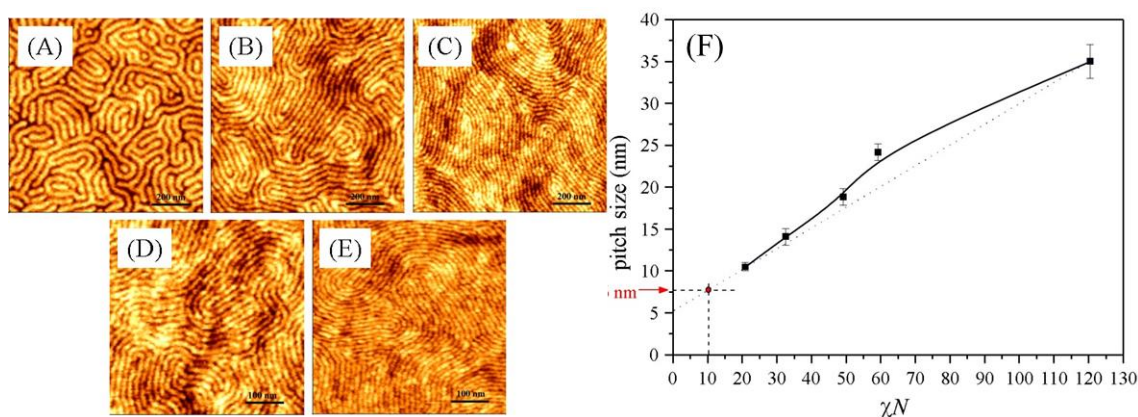


**Figure 6.2.** AFM topographic images of different molecular weight PS-*b*-P4VP BCPs after solvent annealing. The lamellae perpendicular to the substrates were observed in all the BCP system: (A) PS<sub>20k</sub>-*b*-P4VP<sub>17k</sub>, (B) PS<sub>9k</sub>-*b*-P4VP<sub>9.2k</sub>, (C) PS<sub>7.4k</sub>-*b*-P4VP<sub>7.7k</sub>, (D) PS<sub>5k</sub>-*b*-P4VP<sub>5k</sub>, and (E) PS<sub>3.3k</sub>-*b*-P4VP<sub>3.1k</sub>. (F) Pitch size versus the  $\chi N$  values of all PS-*b*-P4VP used in this study. 7.6 nm is an estimated value calculated by drawing an arbitrary line.

Various experimental aspects, such as temperature, time, and solvent(s) were studied. Interestingly, whilst the higher molecular weight BCP system form lamellae in THF vapours, the lower molecular weight BCPs phase separate in toluene vapours to produce well-ordered and well-aligned lamellae microdomains. It was also demonstrated that film thickness plays an important role in the self-assembly of BCPs. Thin films of different thickness were prepared by varying spin speed during casting. It is accepted that in symmetric BCP systems, if the film thickness is thicker than its equilibrium period, island or holes form at the free surface. The film thickness was controlled by using optimised spin speed so as to produce good ordered lamellae structure. Directed Self Assembly (DSA) was demonstrated using graphoepitaxy. Various wide trench substrates were used to demonstrate the long range ordering to achieve sub-7 nm features. By decreasing the molecular weight of polymers smaller features can be achieved. As shown in Fig. 6.2-F, a theoretically pitch size of 7.6 nm can be achieved when total molecular weight of the PS-*b*-P4VP system is approximately 4000 g/mol ( $\chi N=10.5$ ).

In Chapter 4, a novel *in-situ* iron oxide inclusion technique was used to generate an iron oxide hard mask which can facilitate the pattern transfer process. In this high- $\chi$  PS-*b*-P4VP BCP system, the etch contrast between both the blocks are very low due to the similarity between the structures of PS and P4VP (the benzene ring in PS and pyridine ring in P4VP is the only difference). To enhance the etch contrast between the blocks, one of the blocks is modified by incorporating inorganic species (here iron oxide) into the polymeric structure. Iron oxide nanowires are formed by simple inclusion of iron ions by spin coating iron nitrate solution from ethanol into the P4VP block. Ethanol selectively swells the P4VP block, since the PS block is insoluble in ethanol, decreasing the density of P4VP microdomains. Also, P4VP act as a metal ligand to coordinate with metal complexes. As shown in Fig. 6.3, different size iron oxide nanowires are generated by using different molecular weights of PS-*b*-P4VP.

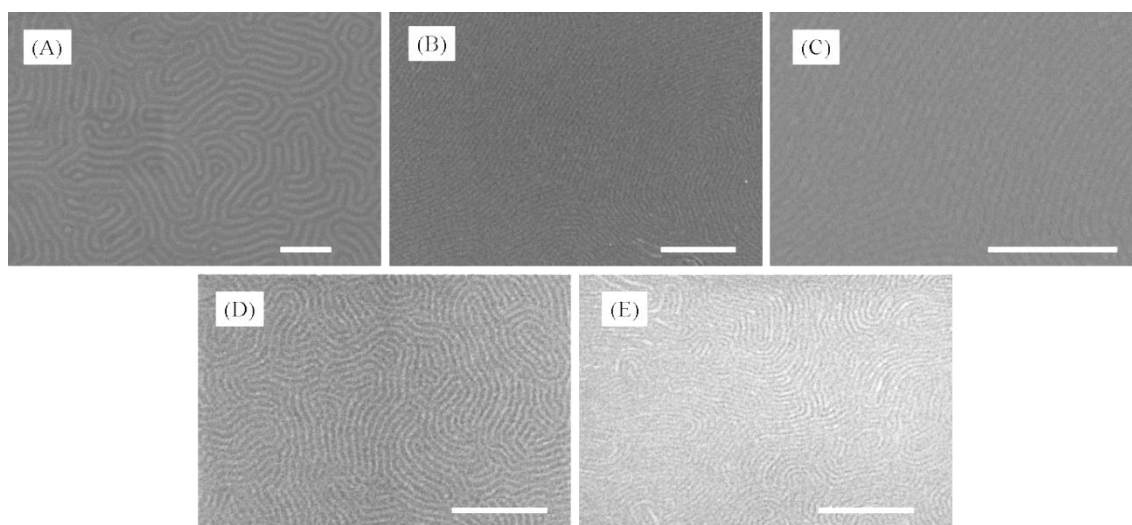


**Figure 6.3.** Top-down SEM images of iron oxide nanowires formed by using (A) PS<sub>20k</sub>-*b*-P4VP<sub>17k</sub>, (B) PS<sub>9k</sub>-*b*-P4VP<sub>9.2k</sub>, (C) PS<sub>7.4k</sub>-*b*-P4VP<sub>7.7k</sub>, (D) PS<sub>5k</sub>-*b*-P4VP<sub>5k</sub> and (E) PS<sub>3.3k</sub>-*b*-P4VP<sub>3.1k</sub>. All scale bars represent 200 nm.

As shown in Fig. 6.3 (E), the smallest feature size of  $\sim 6$  nm was achieved using PS<sub>3.3k</sub>-*b*-P4VP<sub>3.1k</sub>. The concentrations of iron oxide precursor solutions were decreased from 0.5 wt% to 0.3 wt% when the smaller molecular weights BCPs were used. Further these iron oxide

nanostructures were then pattern transferred into silicon substrate to generate silicon nanowires.

In Chapter 5, further applications of BCPs were studied. Two dimensional (2D) molybdenum disulfide ( $\text{MoS}_2$ ) nanowires were fabricated on a silicon substrate by using an *in-situ* technique and post-processing sulfurization. As illustrated in Chapter 4, the *in-situ* technique was applied to generate different metal oxides, mainly molybdenum trioxide ( $\text{MoO}_3$ ). Molybdenum pentachloride ( $\text{MoCl}_5$ ) was dissolved in anhydrous ethanol to yield 0.5 wt% solution, which then spin-coated on the lamellae patterns of  $\text{PS}_{20\text{k}}\text{-}b\text{-P4VP}_{17\text{k}}$ , followed by UV/Ozone to generate  $\text{MoO}_3$  nanowires. These  $\text{MoO}_3$  nanowires formed were then sulfurized at different temperatures to generate  $\text{MoS}_2$  nanowires. The 2D- $\text{MoS}_2$  nanostructures were confirmed by XPS, Raman spectroscopy and by AFM, SEM and TEM.

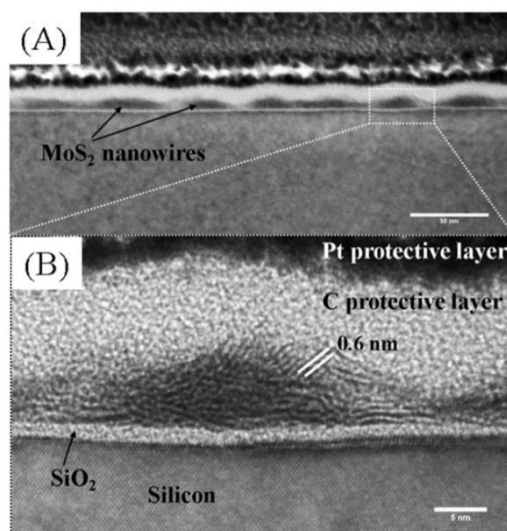


**Figure 6.4.** (A) TEM images of  $\text{MoS}_2$  nanowires. (B) Enlarged HR-TEM image of the marked area in (A).

## 6.2. Recommendations for future work

In order to achieve sub-5 nm features, it is important to consider other block copolymers or new synthesized BCP systems with high Flory-Huggins interaction parameter  $\chi$  with high etch contrast. In order to reduce feature size, small molecular weight BCPs must be used. By

increasing the  $\chi$  value and decreasing the degree of polymerization  $N$ , the  $\chi N$  value can be maintained to more than 10.5 to allow the phase separation. It must be noted that the large unfavourable interaction between the blocks ultimately reduces the interfacial thickness between them, which allows the block-to-block interfaces to exhibit less line-edge roughness. A question remains as to how low can the feature size be reduced to? By polymer engineering 6 nm pitch is possible but producing good films becomes a challenge because films are becoming e.g. strongly hydrophobic and hydrophilic and very strong interface interactions are possible. Indeed, many people believe it is extremely difficult to use high- $\chi$  systems to produce vertically orientated lamellae because of strong interfacial reactions between blocks at the substrate and air interface. One of the things we have not considered in this system is why parallel orientations are not observed. Comprehensive experimental and theoretical work is needed to address the propensity of these systems to form vertical orientations. These have been observed for PS-b-PDMS, PS-b-PLA, PS-b-PEO even for non-chemically functionalised neutral substrates.

For future applications in semiconductor industry, one of the block of BCP system must be etched, either by dry or wet etching steps. Therefore, an etching recipe must be developed to etch the block with the highest possible fidelity. For smaller dimension features, the film thickness is also smaller. To etch such ultrathin films using a chemical etch is very challenging. Due to slower diffusion of gas ions that are confined to nanoscopic space, dry-etching very small features can also be very difficult. As mentioned in Chapter 4 of this thesis, different metal oxide nanostructures can be fabricated by *in-situ* inclusion technique, which then can be used as hard mask for pattern transfer. Whilst iron is not a metal generally used in FABs alternative metal insertion could be used to yield HfO<sub>2</sub>, Al<sub>2</sub>O<sub>3</sub> or W hard masks and the integration of the methodology needs considerable effort. In the semiconductor industry, many attractive technologies have been integrated but very significant effort is required.

It is also necessary to address the problem of defects in these patterns. According to ITRS 2013, the defect density in ordered BCP patterns must not exceed 0.01 defects  $\text{cm}^{-2}$  at the resist level for all device types and this is extremely difficult to obtain. Defects in structure can be originated from various steps during self-assembly. It can occur any time during synthesis, annealing or processing steps. During synthesis of polymer, a special care should be taken while using catalysts, solvents and environment where the synthesis is carried out. The solvents used must be 99.99% pure and the annealing conditions should be carefully monitored. Various methods like real-time scanning microscopic or spectroscopic studies can also be performed to understand defect annihilation. Perhaps the biggest problem will be maintaining ultra-clean environments as single dust particles can cause high defect densities. Maintaining a pristine surface in UHV is problematical but in terms of 'open' laboratory conditions will require very careful control.

For pattern formation, different annealing techniques have been employed. Thermal and solvent annealing techniques are widely used for the self-assembly of BCPs. For high  $\chi$  BCP systems, thermal annealing method is generally not sufficient to bring about high order but by incorporating solvent vapours during annealing steps it is possible to lower the glass transition temperature and phase separation can occur at rapid speed. Recently, microwave annealing has used as an alternative annealing technique to self-assemble high  $\chi$  BCPs. During microwave annealing, solvent may or may not be used, but the microwave radiation excites the silicon substrate and the energy produced during irradiation is enough to make polymer chains flexible and the phase separated structures of good orientation can be formed in few seconds. However, these techniques have not been industrialized. Due to environmental restrictions on the use of various solvents, fab friendly solvents must be used. But as seen here, the choice of solvents during casting and annealing are critical and are selected on the basis of their

properties such as solubility parameters/vapour pressure. It is questionable if enough solvents or equipment are available to allow commercial production.

Thus, despite the enormous amount of research that has been carried out in the past couple of decades, there remains a number of key issues to be addressed before bringing the BCPs into the semiconductor manufacturing process. However, research and development targeting the use of BCP materials and patterning technologies in future integrated circuit (IC) technology nodes continues with pace and their use as on-chip etch masks is becoming more of a real option.